ENGINEERED 2D NANOPLATES FOR PICKERING EMULSIFICATION AND FUNCTIONAL MATERIALS

A Dissertation

by

XUEZHEN WANG

Submitted to the Office of Graduate and Professional Studies of
Texas A&M University
in partial fulfillment of the requirements for the degree of

DOCTOR OF PHILOSOPHY

Chair of Committee,	Zhengdong Cheng
Committee Members,	Mustafa Akbulut
	Jorge L. Alvarado
	M. Sam Mannan
Head of Department,	M. Nazmul Karim

December 2016

Major Subject: Chemical Engineering

ABSTRACT

Layered zirconium phosphate (ZrP), particularly α-ZrP, is crystalline two-dimensional material with a hexagonal shape. Plenty of free hydroxide groups are available on the surface, which provides ZrP a great potential for surface modifications. The surface has been engineered to be either hydrophobic or thermosensitive. Upon surface functionalization, the applications of ZrP disks have been greatly enhanced in Pickering emulsification as well as functional materials.

First of all, after the surface modification with hydrophobic dodecyl chains, ZrP disks were exfoliated into amphiphilic Janus and Gemini ZrP-C18 nanoplates. Both Janus and Gemini nanoplates served well as Pickering emulsifiers of oil-in-water emulsions. Firstly, cancer drug nanoparticles were produced through a surfactant-free emulsification procedure using the ZrP-C18 nanoplates as Pickering emulsifier. The drug nanoparticles fabricated were submicron and relatively uniform, which were ideal designs for delivery. The cytotoxicity assay confirmed the high delivery efficiency of the docetaxel nanoparticles. Secondly, nano-encapsulated phase changing materials (NEPCMs) were fabricated using amphiphilic ZrP-C18 platelets via a two-step Pickering emulsification procedure. The resultant capsules were submicron in size with remarkable uniformity in size distribution. The method's simplicity and low energy consumption suggest promise for scale-up and mass production.

Furthermore, ZrP was modified with the thermoresponsive polymer PNIPAM (poly N-isoproprylacrylamide) via covalent bonding using pre-irradiation method. ^{60}Co γ-

rays irradiation produced peroxide groups on the surface which, upon heating, initiated free radical polymerization and subsequent attachment of PNIPAM. Asymmetric Janus and Gemini ZrP-PNIPAM nanoplates were obtained by exfoliation of the layered ZrP-PNIPAM. The ZrP-PNIPAM nanoplates proved to be thermosensitive Pickering emulsifiers for controlled-release applications. Similarly, the exfoliated ZrP nanoplates were modified into ZrP-PNIPAM. The ZrP-PNIPAM monolayer aqueous suspensions proved to be good candidates to study the isotropic (I) to nematic (N) phase transition of discotic liquid crystal. The I-N transition vs thickness-over-diameter aspect ratio was investigated by adjusting temperature for a single set of samples due to the thermo-responsive property of PNIPAM on the surface. The soft ZrP-PNIPAM monolayers self-assemble into nematic liquid crystals in a wider aspect ratio than do hard disks.

ACKNOWLEDGEMENTS

I would like to express my sincere appreciation to my advisor Dr. Zhengdong Cheng; he has been a wonderful supervisor for me. I would like to thank you for all the valuable support, suggestions and encouragement in my research. I always got energy to continue on each time after discussion with you, especially at the struggling moments regarding either revising a paper or the bottle-neck of experiments. The way you think about science and research is so impressive; your advice on both my research and my career is great property to me.

I also want to thank all my committee members, Dr. M. Sam Mannan, Dr. Jorge L. Alvarado and Dr. Mustafa Akbulut, for their guidance and support throughout the course of this research. Without their help, finishing this dissertation would have been impossible. Especially, I want to express my grateful thanks to Dr. M. Sam Mannan for his financial support for most of my PhD years. I always appreciated the discussions with Dr. Jorge L. Alvarado about the research especially NEPCMs project. I would like to thank Dr. Mustafa Akbulut for letting us use the equipment in his lab. Without his understanding and support, lots of the characterizations in this dissertation could not have been achieved.

Thanks also go to my friends and colleagues and the faculty and staff in the department, for making my time at Texas A&M University a great experience. Special thanks to Dr. Andres Mejia, Dr. Min Shuai, Dr. Ya-Wen Chang, Dr. Agustin Diaz, Yi-Hsien Yu, Ilse Nava, Lechang Zhang, Abhijeet Shinde, Minxiang Zeng, Hai Li, Carlos

Mejia and Dali Huang for the wonderful ideas generated through regular discussions and the good time we had been working together.

I want to extend my gratitude to Dr. Huiliang Wang and Di Zhao from the Department of Chemistry in Beijing Normal University, for their help in the irradiation of ZrP using gamma ray. I also thank Dr. Ravikumar N Majetie, and his postdocs Dr. Melissa Guada and Dr. Raghu Ganugula from Department of Pharmaceutical Sciences, Health Sciences Center (TAMU), for their help in the drug encapsulation project. Dr. Abraham Clearfield in Chemistry Department of TAMU gave suggestions to the dissertation as well, thank you. I also appreciated the work from undergrad students Andrew Schaeffer and Matthew Carlin from Chemical Engineering department of TAMU as well as Chencan Du and Yiyi Cao from Tsinghua University, when they were interns in our lab.

Finally, thanks to my parents, my siblings, and to my husband Yongrui Wang, my sons Edward Y. Wang and Andrew C. Wang, for their support all the time. Without their understanding and love, it would behave been impossible for me to finish this dissertation.

TABLE OF CONTENTS

Page

LIST OF FIGURES

Page

LIST OF TABLES

Page

CHAPTER I

INTRODUCTION AND LITERATURE REVIEW

1.1Two dimensional materials and layered materials

Two-dimensional (2D) materials are layered materials with strong chemical bonds in-plane and weak coupling between layers. These layered structures would allow the 2D materials to be cleaved into individual layers. Since graphene was discovered, two dimensional inorganic materials have attracted more and more attentions recently in colloidal science, not only because of their high surface to volume ratio but also their quantum size effect caused by the nanosized thickness.

Besides graphene family 2D materials (graphene, hBN, BCN, fluorographene and graphene oxide), there are many new 2D materials come into researchers' attentions[1]. There are many ways to identify the types of 2D materials, here we summarize the 2D material by their component into seven different types. (1) Transition metal dichalcogenides (TMDs), who are natural abundance with diverse properties. The chemical formula of TMDs is MX_2, where M is typically transition metal groups (mostly Mo, Nb, W, Ni, V, or Re) while X is a chalcogen (typically Se, Te, or S). Examples of TMDs are: group IV and V transition-metal sulfide (TiS_2, ZrS_2, HfS_2, VS_2, NbS_2, and TaS_2) and selenide ($TiSe_2$, $ZrSe_3$, $HfSe_3$, VSe_2, $NbSe_2$, and $TaSe_2$) nanocrystals[2]. (2) Layered metal oxides, such as MnO_2, MoO_3, and $LaNb_2O_7$. (3) Layered double hydroxides (LDHs), such as $Mg_6Al_2(OH)_{16}$. (4) Metal halides, such as PbI_2 and $MgBr_2$. (5) Some other interesting families including layered III-VIs (such as InSe and GaS), the layered V-VIs,

(like Bi_2Te_3 and Sb_2Se_3), as well as metal trichalcogenides, and metal trihalides. (6) Others, including layered silicates, or clays who are exist as many different types, layered α and γ zirconium phosphates and phosphonates.

The 2D materials can be naturally obtained from the earth or from synthesis[2]. Till now, many methods have been applied to prepare 2D materials, including micromechanical exfoliation, liquid exfoliation, chemical vapor deposition (CVD), Van der Waal epitaxial growth on substrate and hydrothermal synthesis. 2D material have been greatly used in nanoelectronics devices as well as for developing innovative applications in composites, batteries, photocatalysts, sensors, nanoreactors, and nanocontainers.

Generally, in order to form stable colloidal suspensions, exfoliation of 2D materials into single or few layers are required (Figure 1). Both dry exfoliation and exfoliation in liquid phase have been developed for exfoliation. Dry exfoliation included mechanical exfoliation[3], solid-state pyrolysis[4] and intercalant-assisted thermal cleavage[5].

Exfoliation in a liquid phase usually is a very promising and highly effective approach for obtaining high-quality 2D nanomaterials in mild conditions. Sonication or intercalation have been applied for the exfoliation of 2D materials in liquid phase. Sonication can be performed in surfactant solutions, pure or mixed solvents and polymer solvents. And the intercalation method usually contains ion intercalation and polymer intercalations. Chemical modification of 2D materials also play an important role to broaden the applications.

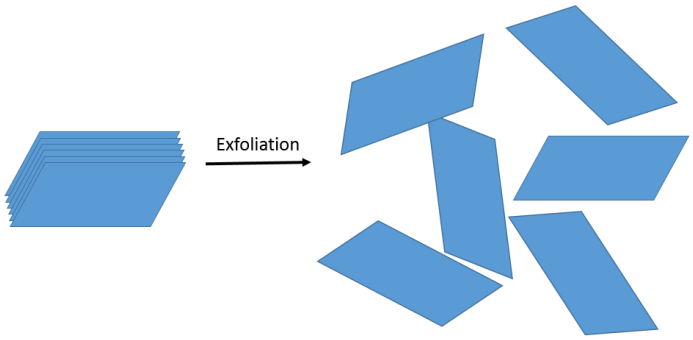

Figure 1. Example 2D material and exfoliation.

1.2 ZrP and exfoliated ZrP monolayers

1.2.1 ZrP crystals

Zirconium phosphate (ZrP), particularly α-ZrP, is a synthesized 2D inorganic material crystals. ZrP has characteristic hexagonal shape, with a chemical formula of $Zr(HPO_4)_2 \cdot H_2O$, and whose size can be engineered from 50 nm to 2 μm[6]. Normally, there are three methods to prepare ZrP, including: (1) hydrothermal[6], (2) reflux and (3) microwave assistant. The single crystal X-ray diffraction structure indicates that the zirconium atoms lie slightly above and below the layer plane and are connected by phosphate groups[7]. In each phosphate group, three oxygen atoms are bonded to three different zirconium atoms while the last one is protonated as hydroxyl (-OH) groups and points either into the interlayer or on the surface of the material. On each side, the density of hydroxyl group on ZrP plate surface is ca. 4.2 groups/nm^2 per side[8].

ZrP have been widely studied and proven to be useful for applications such as flame retardancy[9, 10], fuel cells[11], ion exchange materials[12], gas sensors[13],drug delivery[14],

composites[15, 16], solid support for heterogeneous catalysis in solvent-free or aqueous conditions[17], lubricant additives[18] and proton conductor materials[19].

1.2.2 ZrP monolayers

ZrP can be easily exfoliated into monolayers, using an interactional amines including short amine like propyl amine, tetrabutylammonium, amino alcohols or long chain amine such as Jeffamines which are commercially available polyetheramine oligomers. Ionic liquids have also been reported to exfoliate ZrP[20]. By using intercalation agent and exfoliation agents together, the surface of ZrP monolayers had been enriched. Sue's group used combination of a linear long-chain amine as exfoliation agent and short-chain amine such as cyclohexylamine and dodecylamine as intercalating agents to obtain a high effective exfoliation[21]. Mostly, ZrP was exfoliated in water. Other solvents such as acetone[22] and dimethyl sulfoxide (DMSO) were also reported to serve for exfoliation. The thickness of a naked ZrP monolayer was measured to be 0.68 nm[23] from atomic-force microscopy (AFM) data. However, there were always other chemical chains attached onto the surface depend on the intercalation agents as well as the surface modified chains. Hence, the thickness of exfoliated ZrP monolayer can be range from a few nanometers to several hundred nanometers. And the exfoliated monolayer enhance ZrP more applications. For example, the monolayer ZrP can be used as model material in discotic liquid crystals study[24, 25], since the diameter of ZrP can be controlled in the fabrication step, it is easy to obtain nanoplates with various aspect ratios. Or, the ZrP monolayer can be used as surfactants to stabilize Pickering emulsions[26, 27] and foams[28] .

1.3 Surface modification of ZrP and ZrP monolayers

1.3.1 Surface modification of ZrP crystals

As discussed in 1.1, plenty of attentions had been paid to the "layered" structure ZrP, people have worked hard in order to fully or partially exfoliate ZrP in different ways which resulted in monolayered or few-layerd ZrP respectively, with different functional surface. Only a few researches were related to the flat surface modification of ZrP. Actually, the flat surface of ZrP allow it to become an ideal platform for reactivity. One of the reason is that the disorder of alkyl modifiers due to the nanoscopic curvature of sphere particles surfaces, especially in silica, will not persist in the case of sheets like ZrP[29].

ZrP is crystalline disk, various metals including tin (Sn) and Zr have been used to "modify" ZrP by ion exchange with the proton on ZrP surface. Surface modification of ZrP with organic compounds is always a hot topic since it will broaden its application[15, 24, 30, 31]. The presence of hydrophilic P-OH groups on both layer sides of ZrP endows it various surface attachment possibilities. It is very attractive that the P-OH groups anchored to the layer surface can be replaced with P-OR or P-R groups without altering the inorganic texture of the layer (R is an organic group)[32]. One useful modification is to change the hydrophobic/hydrophilic property of the ZrP surface by interlacing the inorganic P-OH groups with suitable organic groups.

In summary, there are mainly two methods to modify ZrP based on the hydroxyl groups on the surface of the material (Figure 2). Firstly, using chemical reactions, designed organic chains were attached to ZrP via covalent bonds with the hydroxyl groups

on the surface. Years ago, Clearfield and coworkers[33] published results of the successful attachment of polyethylene glycol (PEG) onto the surface of ZrP through ether bonds, and it was achieved through multiple steps of chemical reactions. Recently, a few cases of attachment using coupling agents have been reported including epoxy-functionalized[15], isocyanate-functionalized[26] and silane-functionalized[8, 34]compounds. Secondly, using ion exchange, tetravalent metal was used to ion exchange with the protons of the surface hydroxyl groups, following by attachment of bisphosphonic acids with functional groups[35]. However, there is still restriction to graft organic chains onto ZrP due to limitation of the types of coupling agents.

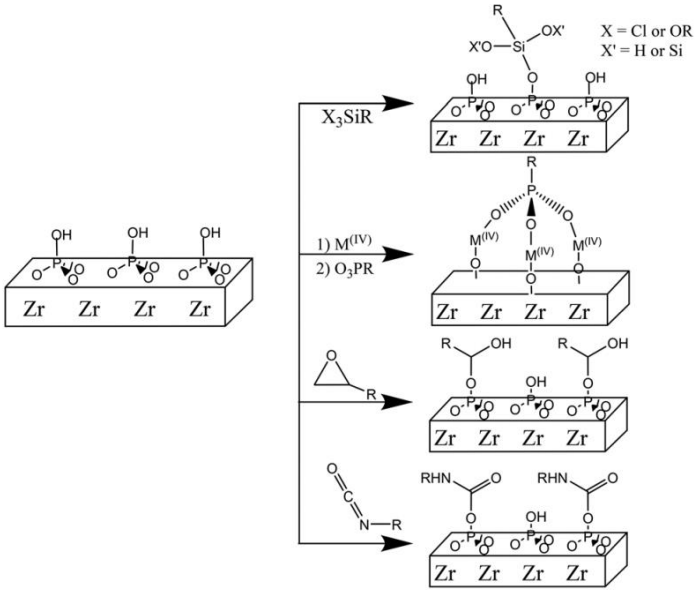

Figure 2. Summary of surface modification of ZrP[30].

Pica'g group[36] first modified partially exfoliated ZrP with dodecyl groups, using 1, 2-epoxydodecane. ZrP was firstly intercalated with propylamine, and then washed with 1M hydrochloric acid (HCl) to regenerate the hydrogen form of zirconium phosphate,

resulted in a gel. After a solvent exchange with tetrahydrofuran (THF), partially exfoliated ZrP gel was mixed with 1, 2-epoxydodecane, upon heating, dodecyl groups were attached onto ZrP through P-O-C bonds.

Besides surface modification after ZrP prepared, functional ZrP with organic group were also fabricated via a direction method. In order to produce this kind of ZrP, phosphate acid derivatives were first designed, usually through a reaction of phosphoryl chloride ($POCl_3$), and then the derivatives were used as reactor instead of phosphate acid. Dr. Clearfield and Dr. Ortiz-Avila mentioned in their book chapter that polyether and polyamine derivatives of ZrP[33, 37]. The functional ZrP synthesized via this method is not alpha ZrP anymore, the interlayer spacing varied a lot depending on the functional groups. Using similar methods, Sichuan University[38] made functional ZrP by using functional phosphate acid to synthesis the functional F-ZrP particles recently.

1.3.2 Functionalized ZrP monolayers

In terms of the surface modification of the ZrP monolayers, efforts have be developed based ob the exfoliations. A direct method to modify the ZrP monolayers is by exfoliation agents. Upon different exfoliation agent, the ZrP monolayers are functionalized correspondingly. Sue group grafting a polar polymer onto ZrP monolayers by exfoliating ZrP using Jeffamine 1000[22].

1.4 Application of surface modified ZrP and ZrP monolayers

1.4.1 Composite fillers

The applications of both ZrP and ZrP monolayers were greatly enlarged after being surface modifications. A high-temperature proton exchange membranes was produced based on the polybenzimidazole modified ZrP[39]. Functionalized (with organic component contained P and N atoms) layered α-zirconium phosphate (F-ZrP) was mixed with poly (lactic acid) (PLA) to form nanocomposites. The results showed that the addition of flame retardant F-ZrP only slightly affect PLA's thermal stability, however, the flame retardancy of PLA composites were significantly improved[38].

In recent years, increasing attention has been devoted to the use of ZrP and ZrP monolayers as fillers[36] of neutral and charged polymers, such as sulfonated polymer. To become a good polymer filler, the compatibility performance of ZrP and ZrP monolayers with polymer is the key factor, so ZrP and ZrP monolayers need to be functionalized with coupling agents which would assure sufficiently strong interaction with the polymer matrix. After modified with hydrophobic chains, the surface modified ZrP has been used to make good polymer filler[31, 37]. Till now, upon surface modification of ZrP, various polymer/ZrP nano-composites have been achieved. For example, fire retardant poly (ethylene terephthalate)(PET)/ZrP[40] was prepared via an in-situ polymerization with diethanolamine midified ZrP; high mechanical property epoxy/ZrP[41] and polyacrylamide (PAM)/ZrP[42] composites were reported by simply mix epoxy with ZrP after Jeffmine treatment. By mixing the polymer with sulfonated ZrP fillers, membranes can be designed and used for direct methanol fuel cells[43].

After surface functionalization, ZrP monolayers have been well served as polymer filler in preparation of composites[21]. ZrP monolayers after surface modification can be acted as a heterogeneous catalyst as well, Single layer ZrP nanosheets were used as heterogeneous catalysts by anchoring a high density of thiol groups on the monolayers surface[8]. The methyl amine functionalized ZrP monolayers can be served as 3D macrocellular foam[44]. Sue's group reported that ZrP monolayers exfoliated with Jeffmine M1000 would self-assemble into sematic liquid crystals would show concentration-dependent iridescence in polar organic solvent[22]. They also observed sematic liquid crystalline organization by dispersing ZrP-M1000 into epoxy[45]. The ZrP monolayers co-assembled with ionic liquid 1-*n*-butyl-3-methylimidazolium chloride resulted in a hybrid that was efficient in carbon dioxide capture[46].

1.4.2 Janus and Gemini nanoplates for Pickering emulsions

Recently, our group have developed Janus and Gemini ZrP nonoplates by surface modification of ZrP, following by fully exfoliation by tetrabutylammonium hydroxide (TBA^+OH^-). The amphiphilic Janus particles[47] and Gemini surfactants[48] are ideal candidates to generate Pickering emulsions[26]. As shown in Figure 3. The name of Janus particle originates from the ancient Roman God 'Janus' who has two opposite faces[49]. Two halves of Janus particles have distinguishable differences in chemical properties. Gemini particles are composed of three parts: a rigid or flexible spacer with two charged groups on the sides. Previous research shows that Gemini particles have a lower critical micelle concentration (CMC) than the surfactants with same molecular length[48, 50] .

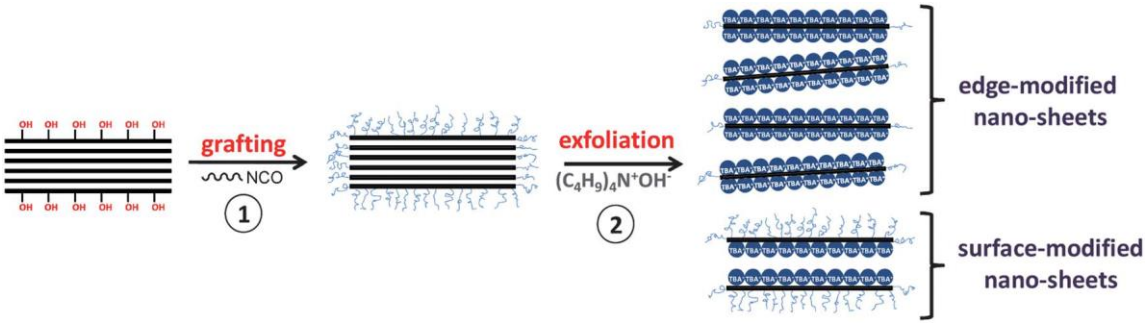

Figure 3. The 2-D schematic representation of the fabrication of surface and edge-modified amphiphilic nano-sheets[26].

Pickering emulsions are stabilized by colloidal particles[26, 51] where the apparent interfacial energy is reduced as solid particles are adsorbed onto the liquid-liquid interface, resulting in stabilized emulsions. Previous studies proved that spherical, rod-like, and discotic particles can be used as Pickering stabilizers. Inorganic particles such as silica, clay, carbon black, barium sulfate, titanium dioxide and calcium carbonate have been widely used as Pickering emulsifiers. Particularly, discotic particles with a high aspect ratio are preferred interfacial stabilizers. One of ideal candidates to generate Pickering emulsions is the amphiphilic Janus particle[47]. The Janus name refers the Roman god of portals, Janus, whose two faces look in opposite directions[49]. The two halves of Janus particles possess distinct chemical properties: one half is hydrophobic, the other, hydrophilic.

Young's equation, $\cos\theta = \frac{\gamma_{PO}-\gamma_{PW}}{\gamma_{OW}}$ (where γ is the interfacial tension, P: particle, W: water, O: oil) reveals the interfacial tension of the Pickering emulsifier at the equilibrium position. The particle adsorb onto the oil-water interface because it is partially wetted by both liquid phases, usually that's when $0^o < \theta < 180^o$. Experimental studies

showed that an intermediate θ values ($60^o < \theta < 120^o$) would produce most stable Pickering emulsions.

Depends on the value of θ, oil-in-water (O/W) emulsions or water-in-oil (W/O) emulsions were stabilized by specific particles. Hydrophilic particles ($\theta < 90^o$) preferred to produce of O/W emulsions. Accordingly, hydrophobic particles ($\theta > 90^o$) tended to produce W/O emulsions.

The remarkable advantage of Pickering emulsions is that they are more stable comparing to emulsions stabilized by molecular surfactants. The reason is due to the relatively large size of the stabilizer, which result in strong binding energies of the particles with the interface. It would require more energy for the particles to detach from the interface into the continuous phase. The desorption energy can be calculated using the equation[52]: $E_b = \pi R^2 \gamma_{OW} (1 - |cos\theta|)^2$. In the other words, Pickering emulsifiers particles with a radius R: (0.01 - 10) μm and intermediate θ are practically irreversibly attached to the interface because the large detach energy requirement (E_b : 10^2 to 10^6 k_BT, k_B, Boltzmann constant; T, temperature). Hence, the Pickering emulsion droplets are highly stable.

Pickering emulsions also have other advantages comparing to emulsions made by conventional surfactants: (1) they can be nontoxic by avoiding molecular surfactants; (2) they make stable emulsions, which is tolerant to the pH, salt concentration, temperature, and composition of the oil phase, they are able to make high internal volume fraction emulsions(HIPEs); (3) intelligent emulsions[53] can be formed by modifying the surface of

the emulsifiers; and (4) the viscosity of the emulsions can be adjusted to required practical applications by changing either the amount or the type of emulsifiers.

1.4.3 Other applications

By the surface modification, ZrP showed better absorption of enzyme so that greatly improve the catalytic activity. ZrP can be easily modified by amine, hence, it has great application as support material for immobilization of enzymes and proteins[54]. The surface of ZrP have been modified with several R functional groups including phenyl, 2-carboxyethyl, or sulfophenyl[55], which provide different surface properties when interacting with proteins. ZrP obtained by the reflux method and treatment with $ZrOCl_2$, can be successfully applied for the selective binding of phosphopeptides from complex biomixtures. For example, it had application in oligonucleotide microarrays due to the strong covalent bond between the zirconium ion and the phosphate group in single-stranded DNA molecules(ss-DNA)[56].

CHAPTER II

THE CANCER-DRUG NANOENCAPSULATION

2.1 Introduction

Drug encapsulation is a hot topic, especially in the drug delivery research and application. Various routes have been used for delivering drug. For example, microgels, liposome, drug nanoparticles incorporated with polymer or not[57-61], metal-organic frameworks (MOF)[62] et al. Drug nanoparticles have advantages in EPR (enhanced permeability and retention)[58], have attracted great attentions[63]. In terms of making drug nanoparticles, surfactants played an important role. Didodecyldimethyl ammonium bromide (DMAB), polyvinyl alcohol (PVA), poloxamer, lecithinas well as SDS have been reported to be stabilizer for making drug nanoparticles[64, 65]. However, limitation came out when the side-effect was considered regarding to the molecular surfactants residual which are toxic to human body. Efforts were suggested to wash the surfactants away after the drug nanoparticles were prepared[64], which might result in the loss of drug materials. On the other hand, the size of the drug nanoparticles was also an important parameter as it was related to the stability, cellular uptake, biodistribution, and drug release[66]. Usually, drug nanoparticle with submicron in size, that's 50 to 1000nm particularly, would hold promise for the targeted delivery[59, 66]. Apply solid particle to stabilize drug material become more and more popular since no surfactant was required to fabricate the drug particles. This surfactant-free emulsification was so-called Pickering emulsification. Pickering emulsions as prepared had advantage in the stability compared to conventional

emulsions prepared via molecular surfactant. The stability of Pickering emulsions was due to higher energy requirement for the detachment of the particle emulsifier from the interface surface. In summary, Pickering emulsification could be a good choice to prepare drug nanoparticles since it is: 1) surfactant-free; 2) higher emulsion stability would prevent the coalescing of emulsions and result in smaller drug nanoparticles.

As far as we know, only a few drug nanoparticles have been made using Pickering emulsifers. For example, starch and silica particles have been used for making drug particles. It has been proved that the drug nanoparticles stablized by solid particles behave quite different from the those stablized by molecular surfactants. As reported, the drug particles encapsulation via Pickering emulsions released much faster than those from identical emulsifier-stabilized emulsions[67]. What's more, the skin absorption of a hydrophilic model penetrant from W/O Pickering emulsions was significantly different from that of identical emulsifier-stabilized emulsions[68].

Unlike the emulsions stabilized by molecular surfactants, Pickering emulsions stabilized by particles were usually more stable when exposed to "harsh" conditions such as high salt and high temperature[69, 70]. It was widely believed that energy greater than k_BT was required to detach the particles from the oil/water interface, quantitatively depending on the particle size. The larger the particle, the more energy to detach particles from the oil/water interface. The greater energy requirement would contribute to the appealing stability of Pickering emulsions[70]. Asymmetric particles with both hydrophobic and hydrophilic properties on a single particle have proved to be more effective in emulsification when compared with symmetric particles[71, 72]. Janus and Gemini

nanoplates are two types of asymmetric nanoplates being developed for emulsification[73, 74]. By definition, Janus nanoplates are characterized by different surface modifications on either facial side, while Gemini nanoplates have different physical properties at the edge compared to facial sides[73].

Here, a method to produce drug nanoparticles of a few hundred nanometers in diameter using surfactant-free technique will be descriped. Percifically, drug particles will be fabricated with inorganic nanoplates coating on the surface. Drug nanoparticles will be fabricated via Pickering emulsification method using surface active zironium phosphate (ZrP) nanoplates. ZrP is layered crystal with haxegonal in shape, and is highly biocompatible, has been proved to be able to intercalate large amounts of drugs and sustain the release[75, 76]. The studied showed that ZrP nanoparticles improved the cellular uptake and cytotoxicity of doxorubicin to metastatic breast cancer(MDA-MB-231) cells[75]. Plate shape is optimum choice for Pikering emulsifer in terms of the emulsification efficiency[71], especially the Janus platelets. Amphiphilic ZrP nanoplates, including Janus and Gemina platelets, were obtained by exfoliation of ZrP whose surface was engineered to be hydrophobic with alkane chains. Amphiphilic ZrP have been applied in Pickering emulsions[26] as well as Pickering encapsulations[27].

The advantages are: 1) the surface active ZrP nanoplates used here is safe for drug applications; 2) the procedure is simple, and ready for mass production; 3) it can be flexibaly applied to various drug materials. And the advantages of the drug nanoparticles are: 1) no-toxic surfactants will be used for the drug nanoparticles; 2) the drug nanoparticles size is relative uniform and small; 3) small drug nanoparticles will allow the

drug to be dispersed in water instead of organic solvent the delivery procedure; 4) The drug nanoparticle are stable for various applications.

2.2 Experiments

2.2.1 Synthesis of ZrP

Zirconium phosphate (ZrP) was prepared by the reflux method: 6g of zirconyl chloride octahydrate ($ZrOCl_2 \cdot 8H_2O$) was mixed with 50 mL of 12 M phosphate acid. The mixture was loaded in a 100-mL round flask and refluxed for 24 h using oil bath at 94°C. The product was washed with deionized water three times, dried in the oven, and stocked for later use. Scanning electron microscopic (FEI Quanta 600 FE-SEM) and transmission electron microscopic (JEOL JEM-2010 TEM) characterizations were used to observe the morphology of the ZrP.

2.2.2 Preparation of ZrP-C18 Pickering emulsifier

The dried white product was ground into fine powder with mortar and pestle. Depending upon ambient humidity and the length of time after the ZrP is produced, one more drying process might be preferred to remove the resident water before the surface modification reaction by letting the sample stay in the oven overnight right before the functionalization of the ZrP surface. The crystals were suspended into extra dry toluene in a three-neck flask with a magnetic stirring bar. And the flask was set in a preheat oil bath at 90°C. Nitrogen was used to flush the sample for 10 minutes. At the same time, octadecyl isocyanate (ODI) was dissolve into extra dry toluene in a small vial and then the solution was added into the three-neck bottle under nitrogen protection. The nitrogen

was stopped 20 minutes after the ODI solution was added in and right before the stirring began. The reaction of ZrP with ODI in a 1:10 (ODI: ZrP) molar ratio at 90°C would last for 24 h under magnetic stirring. The resulting surface-modified was washed with methanol three times with centrifuge and dried overnight in an oven at 70°C.

The Janus and Gemini ZrP-C18 nanoplates were obtained by exfoliating the crystals into monolayers using tetrabutylammonium hydroxide (TBA^+OH^-) at a molar ratio of 1:1 in DI water at room temperature. Typically, 0.5 g of modified ZrP was suspended in 10 mL DI water, and sonicated for at least 2 h. And then 1.1 mL TBA^+OH^- solution was added as exfoliation agent. In order to get a fully exfoliated sample, we may need to wait for 2 to 3 days before using the ZrP-C18 nanoplates.

2.2.3 Pickering encapsulation of docetaxel nanoparticles

Here, a simple Pickering emulsification process by surface-modified ZrP-C18 platelets was performed to produce the docetaxel nanoparticles. The procedure was called emulsion–diffusion–evaporation method[60, 77]. The schematics of the procedure is shown in Figure 4. First, 0.025 g docetaxel was dissolved in 2 mL ethyl acetate (EA) in a 5-mL glass vial and sonicated for 5 mins in an ultrasonic cleaner to allow fully disolve of the drug material. 100 μL ZrP-C18 suspension (containing 5%wt of ZrP-C18) was then added into 20 mL DI water in another 50-mL laboratoray bottle. Secondly, the docetaxel solution was added dropwise into the ZrP-C18 suspension under magnetic stirring at 600 rpm. The mixture was stirring for 30 mins in the laboratory bottle with cap. Thirdly, the whole suspension was emulsified using probe sonication (8W) for 1mins resulted in docetaxel (EA) in water emulsions. 20 mL of DI water was added into the docetaxel emulsions for

dilution, which is the diffusion of the emulsions. Finally, the diluted emulsion in the uncapped laboratory bottle was magnetic stirred in the hood without cap. The sample was stirred at 800 rpm for about 3 h to allow the evaporation of organic solvent EA. The entire suspension was lyophilized using (FD-1A-50, Beijing Boyikang Laboratory Instruments Co., Ltd, China) without any wash procedure, the drug particles was collected after lyophilization.

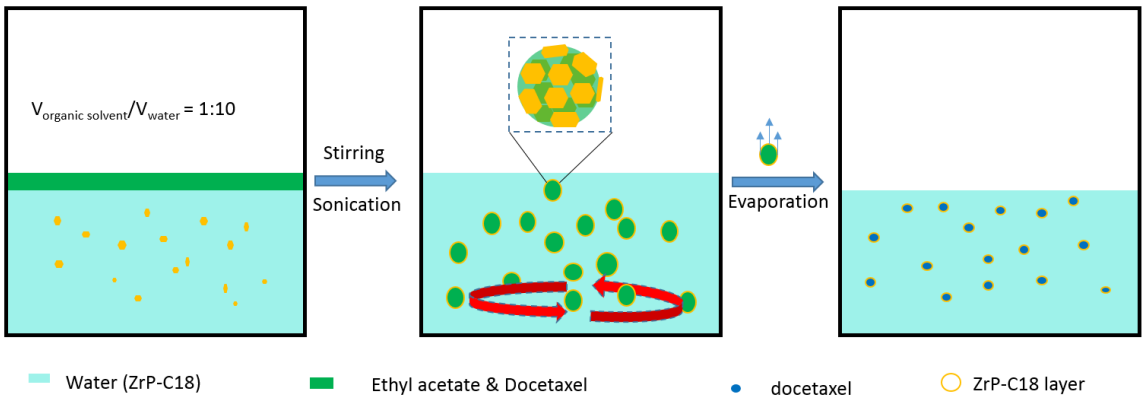

Figure 4. Schematics of the procedure to fabricate drug nanoparticles.

2.2.4 Pickering encapsulation of florescent PLGA nanoparticles

Fluorescent PLGA nanoparticles were obtained using the similar procedure as that for drug nanoparticles. Instead of docetaxel, PLGA coupled to NHS-fluorescein was used for encapsulation in order to mimic water insoluble drug properties. The preparation procedure was exactly the same as that for docetaxel nanoparticles, as shown in 2.2.3

2.2.5 Pickering encapsulation of drug/PLGA nanoparticles

Three different drug docetaxel, paclitaxel and cyclosporin were also encapsulated into nanoparticles using ZrP-C18 as Pickering emulsifier. Here, PLGA was incorporated with drug. Particularly, 20 mL DI water and 100uL ZrP-C18 (with a concentration of 4% wt) mixed together in a 50 mL laboratory bottle with cap, then added 0.025g PLGA and 0.005 g drug was suspended in 5ml ethyl acetate (EA). The emulsion–diffusion–evaporation was applied described in 2.23 for synthesis.

2.2.6 In vitro experiments

Cell culture and conditions: The human ovarian cancer cell lines, SKOV3-TR (taxane-resistant) and SKOV3-sens (taxane-sensible), as well as the breast cancer cell line SUM159 were kindly provided by Dr. Anil K. Sood (Department of Cancer Biology, U.T.M.D. Anderson Cancer Center, Houston, TX). Ovarian cancer cells were grown in Roswell Park Memorial Institute (RPMI) 1640 medium supplemented with 10% (v/v) fetal bovine serum (FBS) and 1% (v/v) penicillin/streptomycin. SUM159 cells were grown in Dulbecco's Modified Eagle medium (DMEM/F-12) supplemented with 5% FBS, 5 μg/mL insulin, 1 μg/mL hydrocortisone and 1% antibiotic/antimycotic. All cell lines were kept in a controlled humidified atmosphere containing 5% CO_2 at 37ºC. Cells were subcultured every 3-4 days when cell confluence was above 80%.

2.2.6.1 Nanoparticle uptake in ovarian resistant cancer cell line

For the cellular uptake study, SKOV3-TR cells were seeded into 6-well plates at a density of 2×10^5 cells per well in completed culture medium and were incubated under

standard cell growth conditions. After 48 h, the medium was replaced by serum-free medium containing fluorescent ZrP nanoparticles at a final concentration of 50 µg/mL for 1 h. Then, cells were washed three times with phosphate buffered saline (PBS), trypsinized and centrifuged at 400 × *g* for 5 min. The supernatant was carefully removed, the cell pellet was resuspended in PBS containing 1% bovine serum albumin (BSA) and centrifuged again at the same conditions. After centrifugation, cell suspension was analyzed by flow cytometry using FACS (Fluorescence activated cell sorting/scanning) caliber, CVM Flow Cytometry Core Facility. Cells incubated with serum-free medium were used as negative control. In order to identify cell death, propidium iodide (PI, 1 mg/mL) was added to the cell suspension at 1:1000 dilution. Flow cytometry data was analyzed using Flow Jo 9.8.5 software. Fluorescence microscopy was used to confirm the cellular internalization of the nanoparticles.

2.2.6.2 Cytotoxicity of docetaxel nanoparticles in ovarian and breast cancer cell lines

The cytotoxicity of ZrP stabilized docetaxel nanoparticles was evaluated against SKOV3-TR, SKOV3-sens and SUM159 cell lines by a colorimetric method using 3-(4, 5-dimethylthiazol-2-yl)-2,5-diphenyltetrazolium bromide (MTT assay). For this purpose, approximately $5x10^3$ cells/well in completed culture medium were seeded into 96-well plates and incubated overnight in a humidified 5% CO_2 atmosphere at 37ºC. Next, the medium was replaced by completed fresh medium containing the treatments (docetaxel nanoparticles, Blank-ZrP-C18 nanoparticles and pure docetaxel) at 4 different concentrations and cells were incubated for another 72 h under the same conditions.

Subsequently, treatments were discarded, 100 μL of MTT (0.5 mg/mL in complete cellular medium) were added to the wells and incubation was continued for 3 h. After MTT solution was carefully removed, the blue formazan crystals were solubilized by adding 100 μL/well of dimethylsulfoxide. The absorbance was determined at 570 nm using a microplate reader. Cellular medium was used as negative control (100% viable cells) and a 20% dimethylsulfoxide solution as positive control (0% viable cells). The cell viability was calculated as percentage related to the negative control.

2.3 Results and discussions

The pristine ZrP particles produced via the reflux synthesizing method are less regularly hexagonal than the ZrP particles prepared by the hydrothermal method[16]. Figure 5 shows the morphologies for numerous and single ZrP particles using scanning electron microscopy (SEM) and transmission electron microscopy (TEM), respectively.

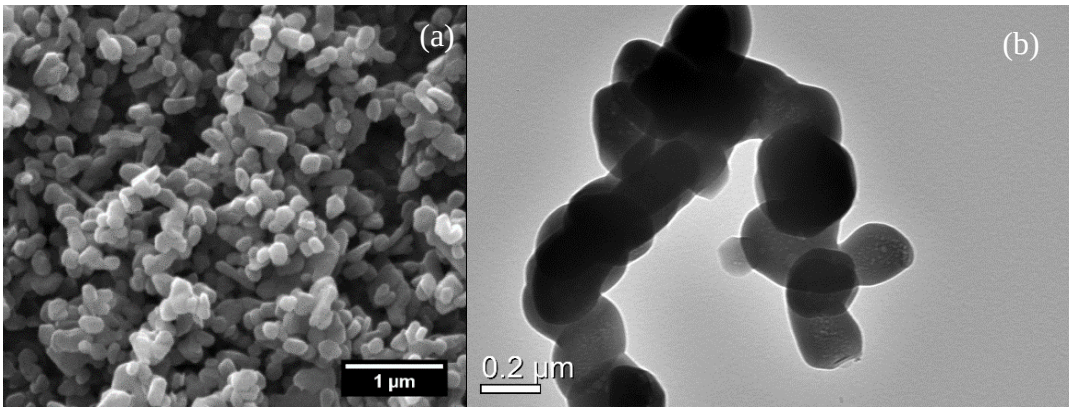

Figure 5. The (a) SEM and (b) TEM images of ZrP as prepared. The particle sizes range from 200 to 300 nm, and the thickness of the crystallites is roughly 20 nm.

In our previous study, we found that the ZrP monolayers after exfoliation has a thickness of about 0.68 nm[17]. With that information, we estimated there are about 30 layers in each pristine ZrP particle.

The ZrP particles are naturally hydrophilic due to the -OH groups on the surface. The surface modification procedure would enhance hydrophobicity of the particles. During modification, a hydrophobic coupling agent, octadecyl isocyanate (ODI), is grafted onto the exposed edges and flat surfaces of the ZrP crystals. After exfoliation with TBA^+OH^- of ZrP layer crystallites, we would obtain two Janus nanoplates, each with a hydrophobic surface and a hydrophilic surface, and about 28 Gemini nanoplates, each with a hydrophobic edge and two hydrophilic surfaces. Both Janus and Gemini nanoplates can act as surfactants to stabilize Pickering emulsions.

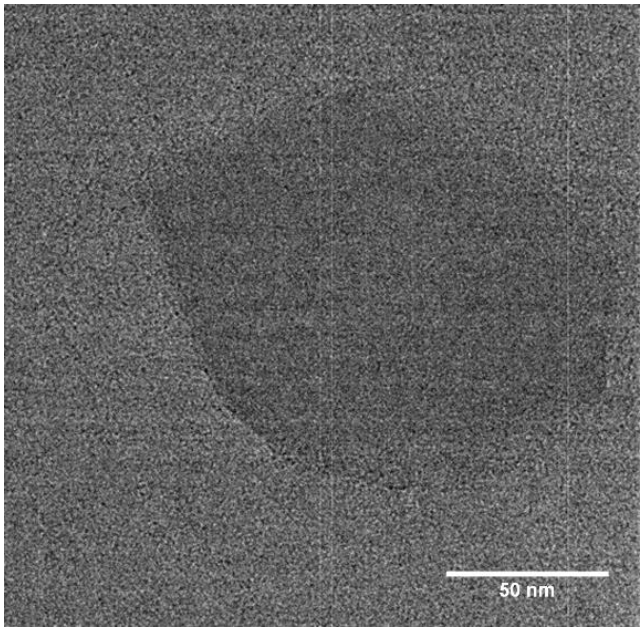

Figure 6. TEM image of ZrP-C18 after exfoliation.

After surface modification, the particle become hydrophobic. A directly phenomenon was that the dried particle powder was floated onto the water-air interface when they were suspended in water. This could require more wettability time when we did the exfoliation. The TEM image was shown in Figure 6 to reveal the nanoplate ZrP-C18 after exfoliation.

The ZrP-C18 nanoplates were able to stabilize docetaxel (EA) in water emulsions as Pickering emulsifier with energy input, such as high speed magnetic stirring and sonication. As obtained in the experiment, the docetaxel (EA) in water emulsions was formed immediately after they were added into the stirring ZrP-C18 aqueous suspension. And the emulsion droplets number were increasing under high speed magnetic stirring. Probe sonication was applied to the docetaxel (EA) emulsion to further reduce the droplet size. Once the sonication was applied, the emulsion become whiter in color, which meant smaller size and larger amount of emulsion droplets were produced. More DI water was added into the emulsion prepared for dilution. The dilution will promote the solvent diffusion under strong stirring. The solvent used here, EA, was really easy to evaporate, hence, all the solvent would escaped from the emulsion droplets left only docetaxel with ZrP-C18 coating on the outer layer. The emulsion suspension was become more and more transparent as the more and more EA evaporated. The reason was that the emulsion droplet was reduced as solvent evaporated.

Both docetaxel and PLGA can be easily dissolved in the solvent EA, sonicated in the clean sonication for 5 mins would help with the fully dissolution and dispersion. EA is a solvent that can be evaporated easily under normal temperature and pressure, and the

evaporation will happen right after it was exposed to air. This why it can be used for this emulsion–diffusion–evaporation method. However, carefully attention needed to be paid to avoid the solvent evaporation before emulsification. We concluded that, strongly magnetic stirring was required during and after the addition so that docetaxel/EA can be emulsified quickly. It was impossible for us to have a closed look into the emulsions since the highly evaporation property of the solvent EA.

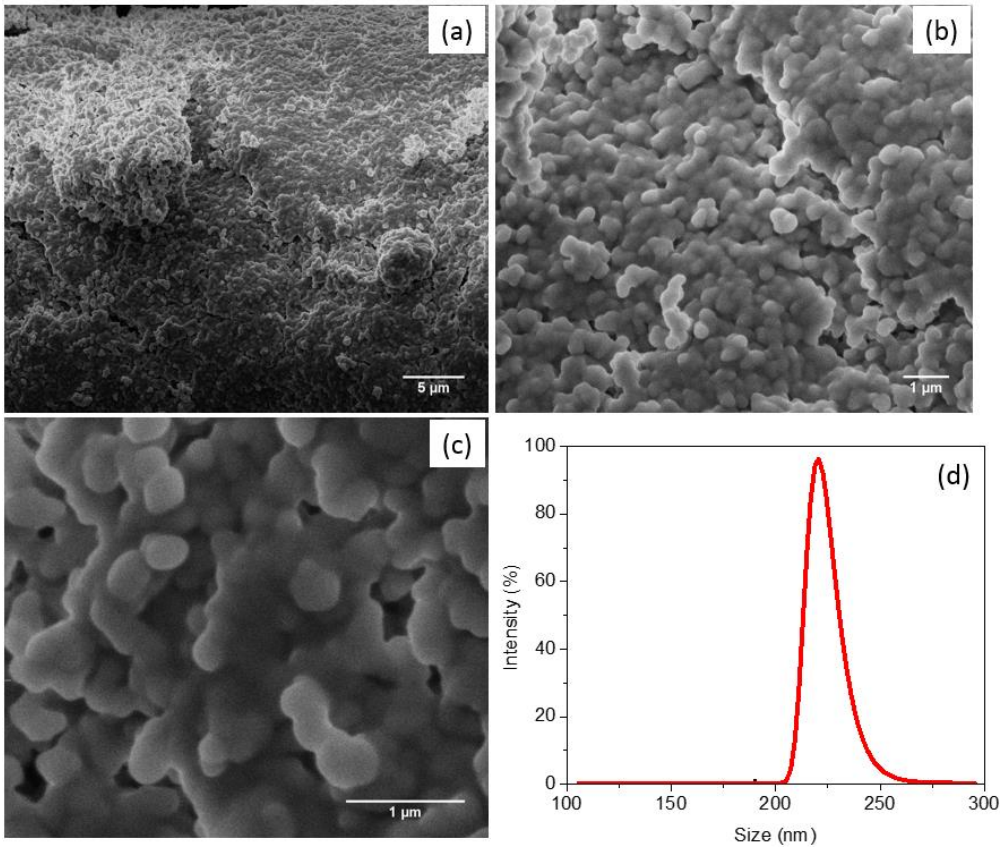

Figure 7. Docetaxel nanoparticles (NPs): (a-c) SEM images with different magnification, (d) size distribution measured by DLS.

The docetaxel nanoparticles and the PLGA were obtained directly for the lyophilization which meant 100% of docetaxel were encapsulated by the Pickering

emulsification method. The docetaxel nanoparticles were investigated using SEM (FEI Quanta 600 FE-SEM). As we can see in Figure 7 (a-c), the docetaxel nanoparticles were spherical mostly and they were relatively uniform in size. The docetaxel nanoparticles can be re-suspended in DI water to make docetaxel suspensions at various required concentrations. The aqueous drug suspensions were stable. Dynamic light scattering (DLS) measured the size of docetaxel nanoparticles to be in a range of 200nm to 270nm, the value was measured to be 220 ± 7.3 nm (Figure 7d).

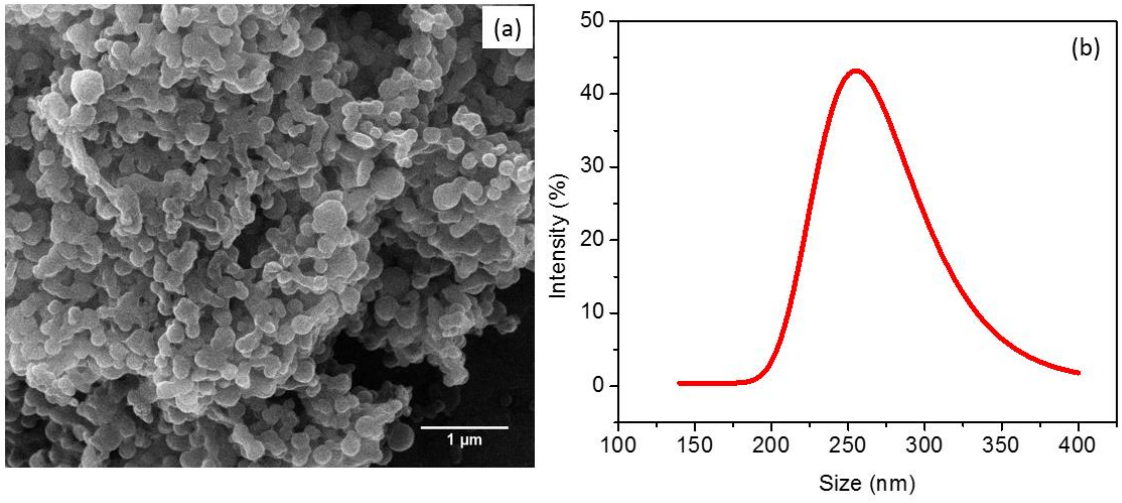

Figure 8. PLGA (with NHS- fluorescein) nanoparticles (NPs): (a) SEM images with different magnification, (b) size distribution measured by DLS.

The size of florescence PLGA nanoparticles was distributed in a range from 200 nm to 350 nm. DLS gave a measured result to be 255 ± 33nm, which was a bit larger than that of docetaxel nanoparticles (Figure 8). The possible reason might be due to the smaller density of PLGA (1.30 g/mL) compared to the docetaxel (1.38 g/mL).

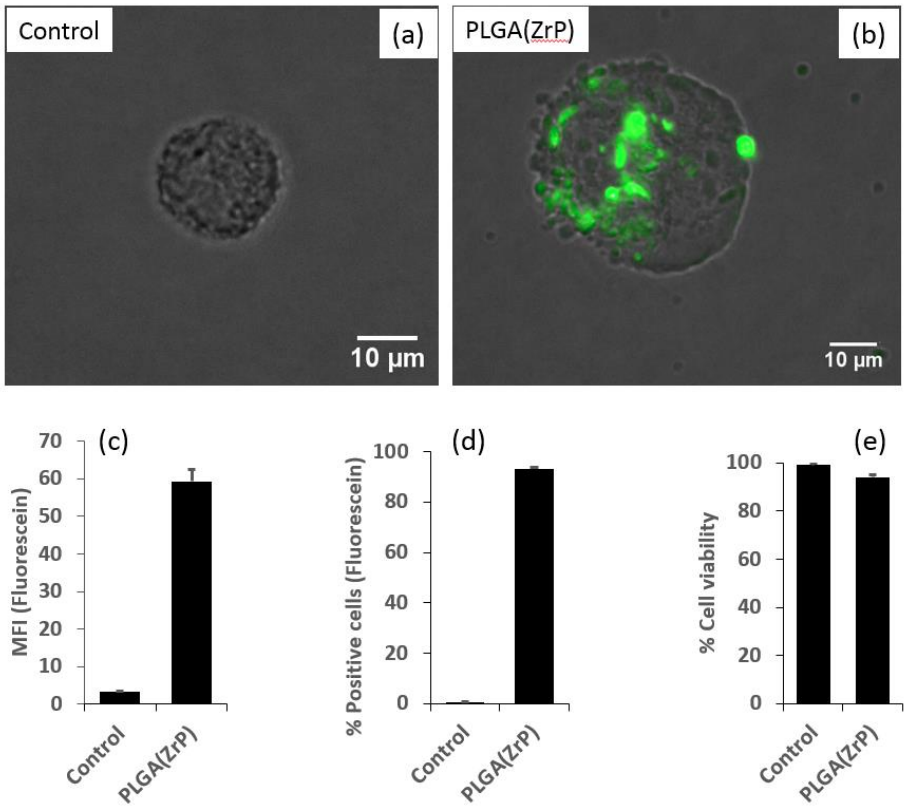

Figure 9. Representative images and FACS analysis of SKOV3-TR cells treated with 50 μg/mL of fluorescent PLGA stabilized by ZrP nanoplates for 1 h. (a, b) Fluorescence microscopy image. (c) Quantification of fluorescein in cells (mean fluorescence intensity, MFI). (d) Fluorescein positive cells. (e) Cell viability.

The mass amount of docetaxel and PLGA used to the nanoparticles were exactly the same when docetaxel nanoparticles and PLGA nanoparticles were prepared. And same amount of EA were used as solvent for both docetaxel and PLGA. Hence, we assume the number as well as the size oil-in-water emulsions for docetaxel and PLGA were similar after emulsification. However, the volume of PLGA was larger than that of docetaxel with the same mass contain. So the size of PLGA nanoparticles was larger than that of drug nanoparticlesTo evaluate the cellular internalization of the nanoparticles, human ovarian cancer cell line resistant to taxanes was used. For this purpose, the fluorescent PLGA

nanoparticles were formulated as previously mentioned. As shown in Figure 9, Zrp-C18 stabilized PLGA-fluorescein nanoparticles were internalized by the SKOV3-TR cells. The FACS analysis showed a high mean fluorescence intensity (MFI) from the cells treated with nanoparticles after 1 h-incubation.

Also, a great percentage of fluorescein positive cells was observed (Figure 9c, d), which indicates that the nanoparticles were taken up for a high percentage of the cell population. The presence of green fluorescence in the cancer cells was confirmed by fluorescence microscopy, as can be observed in the images (Figure 9a, b). In terms of the cell viability, no significant cell death was observed in cells treated with PLGA-fluorescein nanoparticles compared to the control (Figure 9e). Therefore, the ZrP-C18 nanoplates were considered to be safe to the cell during this experiment.

The cytotoxicity of docetaxel nanoparticles stabilized via ZrP-C18 together with pure docetaxel and ZrP-C18 nanoplates were studied in 3 different cell lines including human ovarian cancer (SKOV3-TR and SKOV3-sens) or breast cancer (SUM159) cell lines. The results are shown in Figure 10, where we can see that the growth of the cancer cells treated with docetaxel nanoparticles was inhibited in a dose-dependent manner in similar extent to pure docetaxel. Even better, in some cases, the docetaxel nanoparticles were more effective than pure docetaxel.

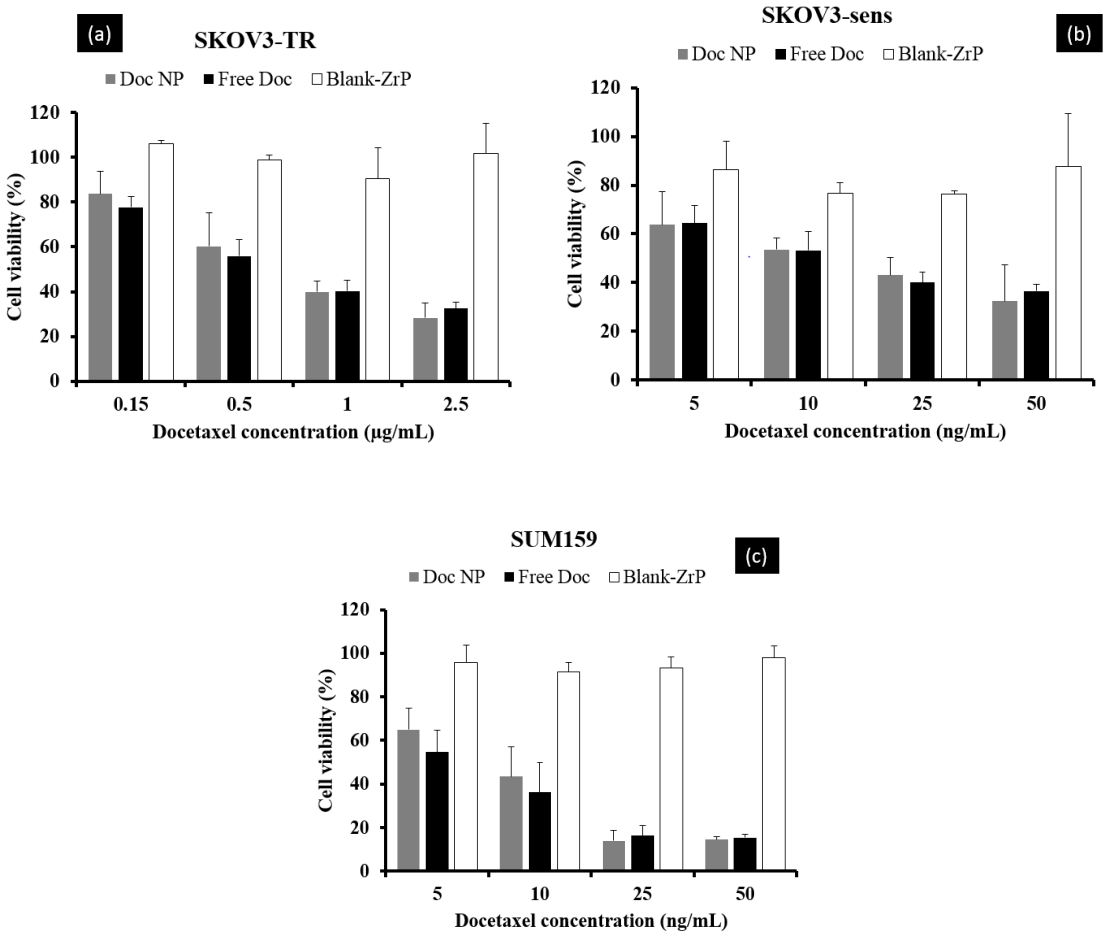

Figure 10. Cytotoxicity of docetaxel nanoparticles (Doc NP) in 3 different cell lines: (a) SKOV3-TR cells, (b) SKOV3-sens and (c) SUM159 compared to pure docetaxel (Free Doc) and plain ZrP nanoplates (Black-ZrP).

Conversely, the viability of cells exposed to ZrP-C18 nanoplates did not decrease at any of the concentrations studied after 72 h-incubation. Therefore, the cytotoxic effect of the nanoplates was attributed to the drug since ZrP-C18 nanoplates resulted safe to the cells.

PLGA/drug nanoparticles were also obtained using the same method and sample Zrp-C18 stabilizer. Two other drugs cyclosporine and paclitaxel together with docetaxel

were also used as drug model for this study. As we can see in Figure 11, the drug/PLGA nanoparticles were relatively uniform as well.

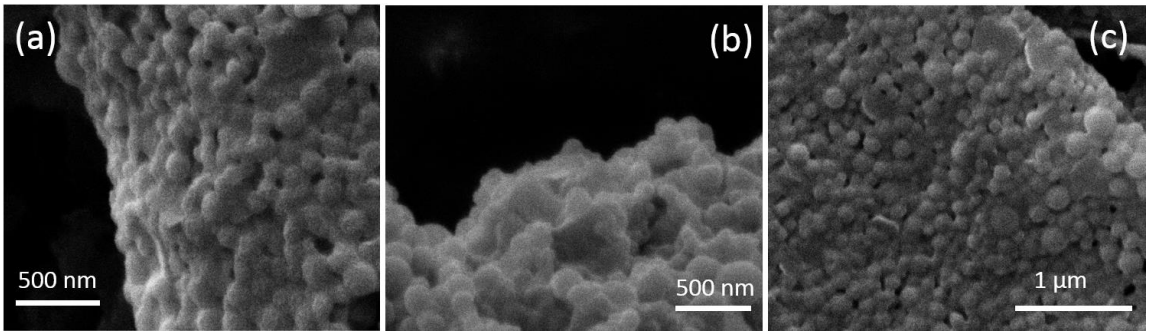

Figure 11. SEM images of drug/PLGA nanoparticles. (a) PLGA/paclitaxel, (b) PLGA/docetaxel, (c) PLGA/cyclosporin.

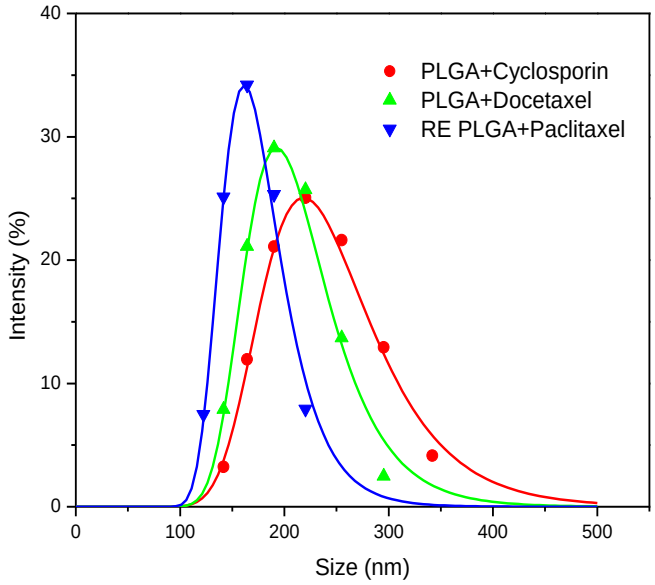

Figure 12. DLS measured the size distribution of PLGA/drug nanoparticles.

Their size distribution were indicated in Figure 12, the size for PLGA/paclitaxel, PLGA/docetaxel and PLGA/cyclosporin were 161±14nm, 192±18.7nm and 218±26 nm respectively. It is obviously that this method can be applied to other drugs and polymers. The size of drug-polymer nanoparticles prepared were similar but not exactly the same.

2.4 Conclusions

Cancer drug docetaxel were fabricated via a Pickering emulsification procedure using amphiphilic ZrP-C18 nanoplates. Fluorescent PLGA nanoparticles were fabricated using same method as well for cellular uptake experiment. The size were in a range of 200 nm to 350 nm which could be useful in drug release application. *In-vitro* studies including cell uptake and cytotoxicity were performed in ovarian and breast cancer cells. The cellular uptake experiment showed that the fluorescent PLGA nanoparticles stabilized by ZrP-C18 were internalized by SKOV3-TR cells. The cytotoxicity assay showed that the growth of cancer cells was inhibited by docetaxel stabilized by ZrP-C18 nanoplates, and the efficiency was similar to that of pure docetaxel. So, we conclude that amphiphilic nanoplates can be used as Pickering emulsifier for fabricating various hydrophobic drug nanoparticles. The Pickering encapsulation technique showed advantages in no surfactant residual, simple encapsulation process and high delivery efficiency, and it can be easily applied to prepare other drug materials nanoparticles.

CHAPTER III

NEPCMS USING PICKERING EMULSIFICATION

3.1 Introduction

Phase change materials (PCMs) which offer one of the most effective strategies for thermal energy storage have been studied since 1970's. PCMs can be organic or inorganic as well as organic-inorganic composites. Organic PCMs including paraffin (C_nH_{2n+2}) and fatty acids ($CH_3(CH_2)_{2n}COOH$), such as palmitic acid and stearic acid, inorganic PCMs can be salt hydrates (M_nH_2O). The high potential heats of the long-chain alkanes with a liquid-solid phase transition, including different carbon number of paraffin (such as n-nonadecane), endow their capability to be applied as a phase changing material. However, the moving liquid phase of PCMs and low heat transfer rate limits their practical application.

Encapsulation and microencapsulation techniques were developed to improve the heat transfer rate by increasing the totally heat exchange area. Encapsulation is defined as a procedure to entrap one substance within another[78]. The substances being encapsulated, also named core, fill, active, internal or payload phase, while the outside substance is often called shell, coating, membrane, capsule, carrier material, external phase, or matrix. Recently, Kousksou *et al*. reported thermal behavior changes during melting process for

---

Parts of this section are reprinted with the permission from Scientific Reports: X. Wang, L. Zhang, Y.-H. Yu, L. Jia, M. Sam Mannan, Y. Chen and Z. Cheng, *Scientific Reports*, 2015, **5**, 13357.

paraffin based PCMs[79].

PCMs can be applied in solar energy storage[80, 81], system coolant[82] and even thermal transfer fabrics[83]. Miniaturization of electronic devices has yielded tremendous improvements in the commercial adoption of these systems in recent years. However, the heat fluxes in these devices are high, from about 50 W/cm^2 in the current electronic chips to about 2000 W/cm^2 in semiconductor lasers[84]. The challenge in cooling such devices is that the chip temperature has to be maintained below 100 ^{o}C despite the high heat flux. Such a high heat flux imposes a practical limit on traditional cooling approaches such as forced air convection which hardly achieves more than 100 W/cm^2 heat flux. Therefore, new electronic cooling techniques are required. Possible methods include thermoelectric cooling, direct immersion pool boiling, heat pipes, liquid jet impingement or spray cooling, and forced convective boiling in microchannels. Zhang[85] compared the various cooling techniques, and concluded that microchannel is one of the most promising methods because of the material and process compatibilities with the electronics industry, device compactness, as well as the small pumping power required.

Coolants play an important role in the performance of microchannel heat exchangers. At present, pure fluids, such as water and ethylene glycol, are often used as coolants in microchannel cooling. The observed literatures show that (1) for single-phase cooling of a liquid coolant, the coolant temperature increases in the streamwise direction, as a result, the cooling performance of microchannels decreases significantly, (2) for two-phase boiling flow of coolant, the high heat flux can be removed, while keeping the coolant and the microchannel temperature constant due to the use of latent heat rather than

the sensible heat of the coolant; however, the unstable operation due to rapid bubble expansion and occasional flow reversal makes the application of the two-phase cooling difficult[86, 87].

In recent years, Lee et al[88], Mohammed et al[89] and Rimbault et al[90] have tried to use nanofluids of high thermal conductivity as coolants instead of pure coolants, but found that higher heat transfer coefficients were achieved mostly in the entrance region of microchannels and the enhancement was still weaker in the fully developed region. Ye et al[91], Farid et al[92], and Sabbah et al[93] used microcapsule suspensions as coolants to improve the thermal performance of microchannels. The microcapsules contain phase change materials which melt and solidify at a specified range of temperature. They found that the microcapsule suspensions always showed better cooling performance than pure fluids leading to lower wall temperature and enhanced heat transfer coefficients. Therefore, latent heat microcapsule suspension is a promising candidate of innovative coolant in microchannels.

Studies on the characteristics of latent heat microcapsules have showed that microencapsulated PCMs prepared by conventional methods, such as spray drying and situ polymerization, is generally in microscale size[94, 95]. These microcapsules can easily fracture or cause clogging problem in microchannel flows and during pumping. Therefore, developing new technologies to encapsulate PCMs at nanoscale is necessary. Nanosize can help to increase mechanical stabilization and mobility of PCMs. Moreover, nanoencapsuled PCMs (NEPCMs) can further increase total heat exchange area, thus

enhancing the heat transfer rate between the coolant and the microchannel wall, reducing the mass flow rate and pump energy consumption.

Liang et al. reported a micro-scale MEPCMs [96]. However, smaller PCMs core-shell structures are rarely reported. A nano-scale encapsulated PCMs can further increase the totally heat exchange area, thus increasing heat transfer rate. Moreover, a smaller size in structure can also help to increase the mobility of PCMs which may be applied as coolant favorably.

In order to make nanoencapsulated phase changing material core-shell structures, small droplets of the alkane core should be dispersed in solution. During the emulsification, stable nano emulsions of alkane will be preferable. In this work we are trying to optimize emulsifying process by employing Pickering emulsification. Pickering emulsions are emulsions stabilized by colloidal particles[26, 97].

Only a few encapsulated PCMs via Pickering emulsification have been reported[98], but PCMs encapsulated by Janus and Gemini Pickering emulsifiers was rarely studied. In previous Pickering encapsulation study, high energy input, such as probe sonication, was needed to produce stable emulsions in a similar way that conventional emulsions are made, due to the energy barrier between the particle suspended in the aqueous solution and the water-oil interface[26, 98, 99].

In this work, we are trying to optimize the emulsifying process by employing a Pickering emulsion procedure. The rigid Janus and Gemini particles provided robust support for the inner paraffin.

3.2 Experiment

3.2.1 Two-step Pickering emulsification to fabricate NEPCMs

Here, a simple two-step Pickering emulsification process by surface-modified ZrP platelets as mentioned in 2.2 was performed to produce the NEPCMs. The entire procedure is shown in Figure 13. The low interfacial energy introduced by our modified ZrP particles can stabilize nanoemulsions and enable a narrow size distribution. Also, due to the low interfacial energy, we can generate the alkane nanoemulsions easily by manually shaking the suspensions. The low energy input requirement suggests the feasibility of applying this method to mass production of the NEPCMs for commercial application.

First, 0.02 g nonadecane was melted in 1 mL deionized water, and then mixed with 1 mL ethanol co-solvent and 100 µL ZrP-C18 suspension (containing 5%wt of ZrP-C18). The mixture was gently shaken for 30 seconds, which produced the nonadecane in water (oil in water, O/W) emulsions for the next step. In the second step, 100 µL styrene monomer together with 0.0016 g initiator azobisisobutyronitrile (AIBN) were added into the O/W emulsions produced in the first step, and the new mixture was manually shaken for another 30 seconds. Finally, the entire NEPCMs precursor was transferred into a 70°C oven for 4 h, allowing for the full polymerization of styrene, with polystyrene as the shell. The NEPCMs sample were raised with warm DI water (50°C) for twice and then dry using a freezing dry machine.

For the scale-up test, we used 100 times more materials: 4g nonadecane, 20mL styrene, 20 mL ZrP-C18 suspension and 100 mL DI water and 100 mL ethanol, and followed the two-step Pickering emulsification procedure.

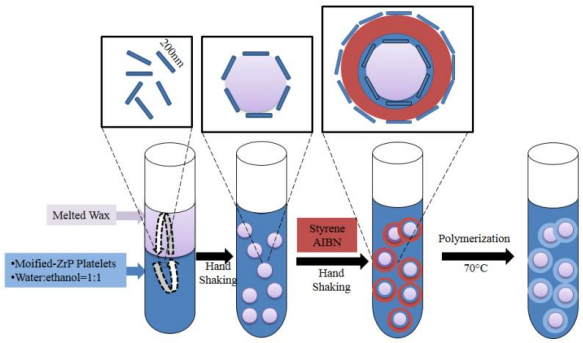

Figure 13. Schematic of NEPCM fabrication via two-step Pickering emulsification.

3.2.2 Characterization of PCM emulsions

The nonadecane in water emulsions was investigated using confocal microscope (laser scanning confocal microscope Nikon A1R). DLS was applied to measure the size distribution of nonadecane/water emulsions. The measurement was done using a diluted suspension of nonadecane/water emulsions suspension. Original measured data from DLS was exported, and the Software Origin was used for the fitting and calculation.

3.2.3 Characterization of NEPCMs

Confocal microscopy images were taken using laser scanning confocal microscope Nikon A1R, upon dye-treated NEPCMs sample. Nile red was added into the nonadecane

after melting at a very low concentration about 1ppm. Fluorescein isothiocyanate (FITC) was used dye the outside aqueous phase.

SEM was used to investigate the morphology of NEPCMs. In order to prepare specimen for the SEM image observation, a tiny drop of NEPCMs suspension was added onto a double size carbon tape on a SEM stage, the sample was dried in the over before loaded into SEM equipment.

Dynamic light scattering (DLS, Malvern Instruments Ltd. England) was applied to measure the size distribution of NEPCMs. Usually, the measurement was done using a diluted suspension of NEPCMs suspension right after sonication using clean sonication machine. Original measured data from DLS was exported, and the Software Origin was used for the fitting and calculation.

The thermal behavior of the NEPCMs was measured using differential scanning calorimetry (DSC, TA Instruments, United States) under normal nitrogen conditions. the NEPCMs specimen was held first at 0°C for 2 minutes, then heated from 0°C to 50°C at a rate of 5°C/min, and finally cooled to 0°C at a controlled rate of 5°C/min.

DSC was also used to characterize the thermal stability, particularly, NEPCMs was tested using NEPCMs after 100 and 200 heating-cooling cycles. The thermal cycling was performed in a P×2 thermal cycle machine (Thermo Electron Corporation, USA). The first 100 cycles were performed at a fast heating-cooling rate of 3°C/s. The heating-cooling rates for the second 100 cycles followed those used for DSC measurement, 5°C/min heating to 50°C and then 5°C/min cooling to 0°C, staying at both 0°C and 50°C for 30 seconds.

3.2.4 Further development of NEPCM using PMMA shell

Instead of using PS as the shell of NEPCM, poly methyl methacrylate (PMMA) was also used to prepare NEPCMs. The procedure was exactly the same, using two-steps Pickering emulsification, but change the monomer from styrene to methyl methacrylate (MMA).

Two other mixing methods, magnetic stirring as well as probe sonication were applied for emulsification. The materials used for three different methods were exactly the same, 200mg of nonadecane added into a vial containing 1 mL DI water, 100 µL ZrP-C18 nanoplates suspension and 1 mL ethanol. After the first step emulsification, 100 µL of MMA monomer and 0.0016g AIBN were added for the second step emulsification.

For the probe sonication method, everything was the same as we did for 3.2.1 but the emulsification method. Instead of manually shaking, probe sonication (at 8W) was applied to the mixture at the nonadecane water interface for emulsification.

Magnetic stirring was applied for the emulsification. The stirring was applied during the polymerization which was carried out in a heated oil bath on a stir plate. The oil bath was maintained at 75 °C and was continuously stirred at roughly 300 rpm. Just like the hand-shaking and sonication methods, the water, ethanol, nonadecane (wax), and the ZrP-C18 surfactant were added to a glass bottle; however, in this case, a stir bar was also added, the glass bottle was submerged 80% in hot oil, and the bottle was left to heat and stir for 45 minutes with the lid closed. Once the emulsification was complete, the MMA monomer and AIBN initiator were added and the bottle was left, tightly closed, for 4 h to allow the completely polymerization.

3.3 Results and discussions

With a small amount (0.024 % wt to the aqueous phase) of the ZrP Janus and Gemini nanoplates, nonadecane in water (Oil/Water) emulsions were generated by 30 seconds of gentle manual shaking. No high energy input (i.e. sonication) was required. A laser scanning confocal microscope was used to characterize the morphology of the nonadecane/water emulsions. The nonadecane, however, easily solidified at room temperature when one small drop of the emulsion solution was loaded onto a glass slide before the observation under microscope. As a result, we were imaging the solidified nonadecane/water emulsions, in the other words, nonadecane droplets, under the confocal microscope.

Figure 14 showed the microscopic image of the nonadecane droplets, the size of which was quite uniform, 524 ± 91 nm, as measured by dynamic light scattering measurement. When we were performing the two-step Pickering emulsification, however, the nonadecane was still liquid since a small amount of monomer styrene and initiator AIBN were added into a bulk emulsion solution right after the first manual shaking, cooling the solution only slightly, but the bulk temperature of the solution remained above the melting temperature of nonadecane.

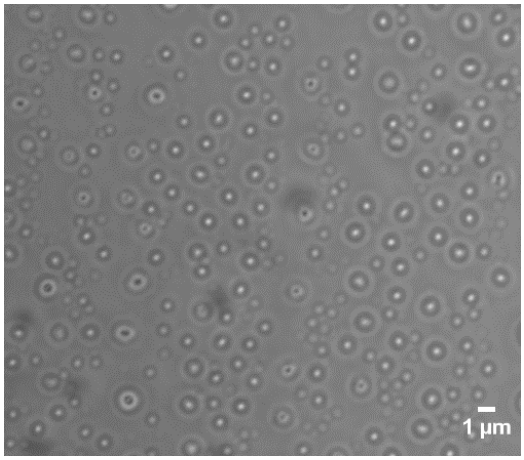

Figure 14. Microscopic image of nonadecane/water droplets by confocal microscope. The emulsion droplets with a light halo were out of focus.

After the second Pickering emulsification, manual shaking gently again for 30 seconds after addition of monomer and initiator, nonadecane/water/styrene/water multiple emulsions were obtained. The confocal images of the NEPCMs before drying, as shown in Figure 15, indicated the multiple structure of the NEPCMs. The green color came from the fluorescein isothiocyanate (FITC) the aqueous phase while the red color came from the Nile red in the nonadecane. Both colors showing together in the image meant there were a small water layer between the nonadecane and PS after the NEPCMs were fabricated. This assumption could be explained by the emulsion stabilization mechanism as well.

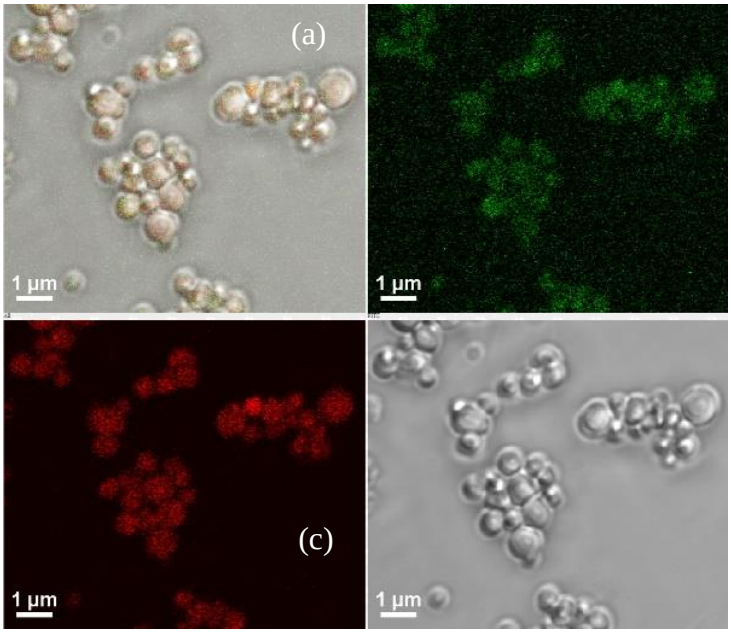

Figure 15. Confocal image of NEPCMS. (a) Double fluorescent labelling indicates locations of aqueous phase (fluorescein isothiocyanate, FITC) and nonadecane (Nile Red), (b) green channel showing FITC fluorescein fluorescence, (c) red channel showing Nile red fluorescence and (d) white light showing the NEPCMs without fluorescence.

Hence, we proposed a schematic for the two-step Pickering emulsification procedure. As shown in Figure 13, the nonadecane-in-water emulsions together with the hydrophobic initiator would be the oil phase for the second step emulsification. By the polymerization of styrene at 70 °C, a core-shell structure was created in which the phase changing material nonadecane was the core and the polystyrene was the shell.

Figure 16 show the SEM image of NEPCMs. They were relatively uniform, as shown in Figure 17, the size of these NEPCMs was measured by DLS to be 734 ± 110 nm.

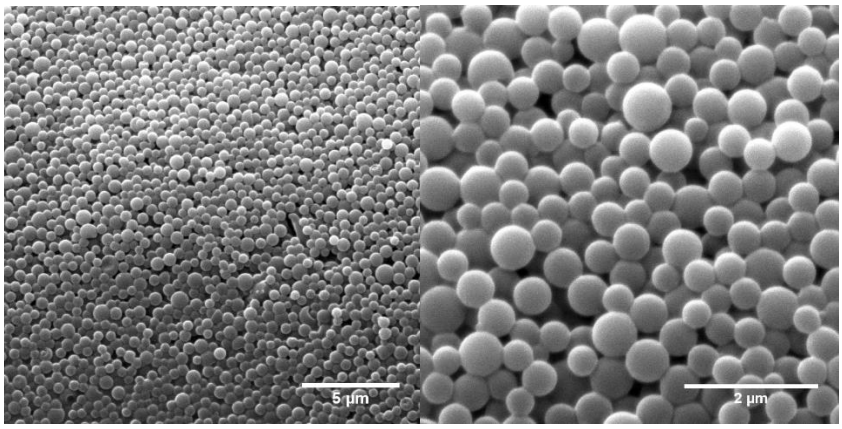

Figure 16. SEM images of NEPCMs particles.

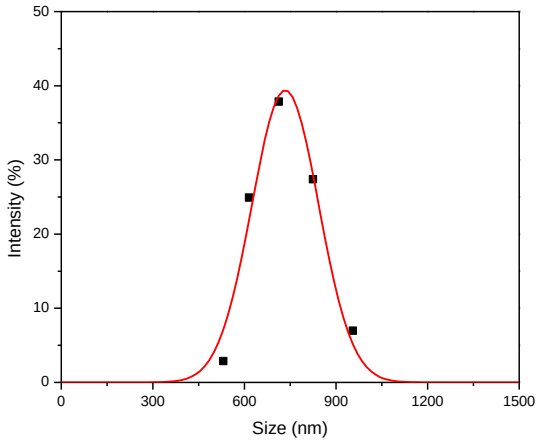

Figure 17. Size distribution for NEPCMs as measured by DLS.

When we used more materials to synthesize NEPCMs, in a 250 mL reusable glass media bottle, we were able to produce 10g NEPCMs with similar quality (as shown in Figure 18).

Figure 18. Mass produce of NEPCMs of 10g. A) Right after prepared, b) after drying.

We know that the thickness of the shell layer of NEPCMs was about 110 nm by simple calculation. There are two advantages to the two-step emulsification to produce NEPCMs. First, only a small amount of energy is required for the emulsification procedure. The ability to produce Pickering emulsions using low energy input is due to decreased surface tension in the water phase caused by the addition of ZrP-C18 nanoplates[8] and the co-solvent ethanol together. Moreover, the size of either nonadecane/water emulsions or NEPCMs was quite uniform. Employing modified ZrP, rather than molecular surfactants, promotes formation of more stable Pickering emulsions due to the limited coalescence in the solid-stabilized emulsions as described by Arditty[100]. The nanoplates absorbed on the water-oil interface prevents coalescence of Pickering emulsion droplets and, therefore, hinders creation of larger emulsion droplets. Prevention of coalescence, in other words, promotes formation NEPCMs with uniform size distribution.

The thermal behavior of the NEPCMs was measured using differential scanning calorimetry under normal nitrogen conditions. Heat flow versus temperature was obtained

via DSC characterization, with results shown in Figure 19. As temperature increased from 0 to 50°C, there were two endothermic peaks for pure nonadecane at 24.00°C and 34.12°C[101]. The first endothermic peak at 24.00°C was due to the rotator phase of n-alkanes below the melting temperature. The second endothermic peak at 34.12°C indicates the melting temperature. In the cooling process, two exothermic peaks were obtained. The crystallization point was 29.79°C, and the nonadecane was converted to stable crystal phase at 20.25 °C, at which temperature it was trapped in the face-centered orthorhombic rotator phase.

As for the NEPCMs, however, their thermal behavior was quite different (Figure 19). Three endothermic peaks appeared in the heating process, 22.77°C, 32.30°C, and 36.95°C. The peak at 22.77°C was attributed to the change from orthorhombic crystal to rotator phase, and the peaks at 32.30°C and 36.95°C were due to the conversion from rotator phase to metastable phase and metastable phase to liquid phase, respectively. Three exothermic peaks appeared in the cooling process, 32.90°C, 29.47°C and 14.67°C. The peak at 32.90°C was attributed to the exothermic peak for nonadecane transitioning from isotropic liquid to new metastable phase. The big exothermic peak at 29.47°C was caused by the transition from metastable phase to rotator phase; at 14.67°C, the rotator phase became orthorhombic crystal.

Comparing the DSC thermal behaviors of the NEPCMs to that of pure nonadecane, we found that there was one additional peak in both heating and cooling procedure for NEPCMs than occurred for pure nonadecane. For example, there was a new endothermic peak at 36.95°C in the heating procedure and a new exothermic peak at 32.90°C in cooling

procedure. The new peaks were caused by the surface freezing of the encapsulated nonadecane, which caused the encapsulated nonadecane become a metastable phase. Moreover, the positions of either endothermic peaks or exothermic peaks of NEPCMs were delayed slightly compared with those of pure nonadecane. This is normal for most encapsulated phase changing materials, and can be improved by adding better thermal conductivity materials into the shell of encapsulated materials.

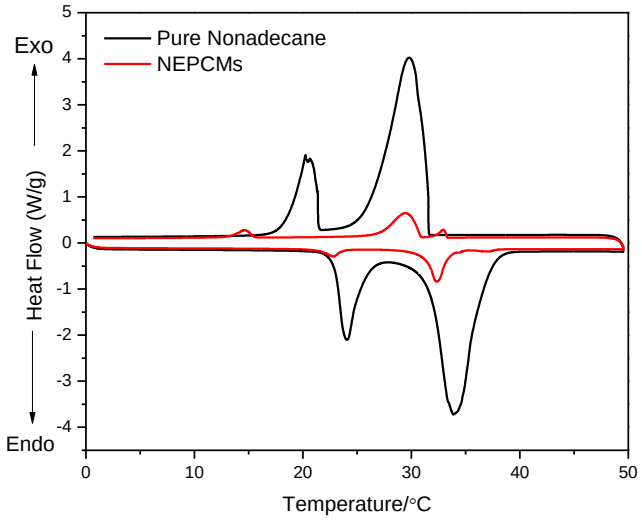

Figure 19. DSC traces of pure nonadecane and NEPCMs

Two more series of DSC measurements were carried out on the same NEPCMs sample to obtain the stability of this material (Figure 20). The thermal cycling was done in a P×2 thermal cycle machine. The DSC curve for NEPCMs, after 100 cycles at a fast heating-cooling temperature rate of 3°C/min, shown as blue line in Figure 20, almost duplicated the first curve (red line), which is the thermal curve for NEPCMs with no

thermal cycle. The green line in Figure 20 shows the DSC curve for the same sample after 100 cycles at exactly the same temperature conditions as for DSC characterization. It was found that the peaks were located at almost the same temperature for the three curves, proving the stability of the NEPCMs. The height of the peak for the 100-cycle curve, however, was slightly lower that the curve depicting no cycling; and similarly, the height of the peak after 200 cycles was slightly lower than that for 100 cycles.

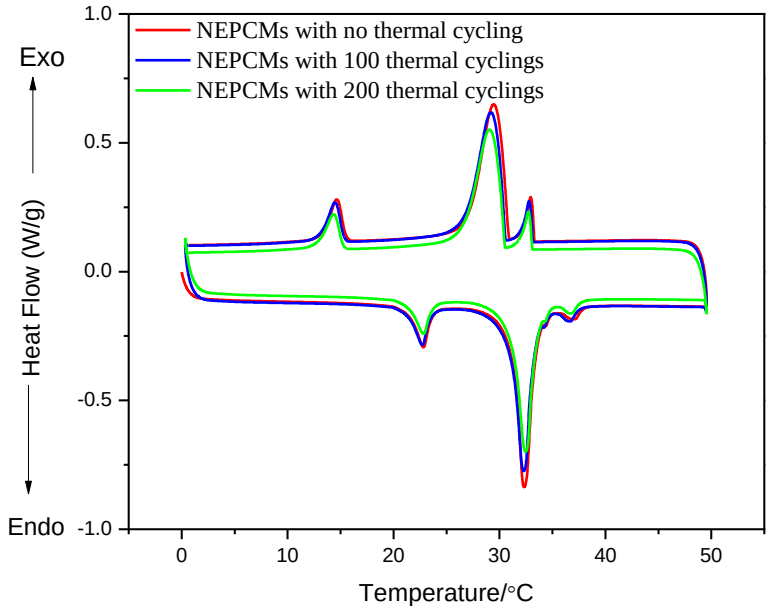

Figure 20. DSC traces of NEPCMS before and after heating-cooling processes.

Encapsulated phase change materials suspensions function as effective micro-channel coolants[93]; however, the encapsulated PCMs engineered to date, which measure several tens of microns, tend to fracture or clog the micro-channels due to their relatively large size[102]. Smaller encapsulated PCMs, such as NEPCMs, are rarely fabricated.

Reducing the particle size of encapsulated PCMs enhances their mechanical stability and mobility. Moreover, NEPCMs present a larger total heat exchange area in comparison with conventional encapsulated PCMs, enhancing heat transfer rate between the coolant and micro devices, thus reducing mass flow rate and pump energy consumption. NEPCMs, therefore, are favorable as micro-channel coolants. NEPCMs also serve in other applications, including solar energy storage media[80, 81], building temperature regulators[103], and thermal transfer fabrics[83]. To build up core-shell structures of NEPCMs, small droplets of the phase change materials core, such as paraffin, are dispersed in solvent. During emulsification, a stable nanoemulsion of paraffin is preferable.

The encapsulation efficiency of nonadecane in NEPCMs was determined from the following equation (1) [101]. Encapsulation efficiency determined the amount of PCMs which had been encapsulated over the total PCMs added as material, it was depended on the encapsulation quantity. Less than 100% encapsulation efficiency meant some of the PCMs hadn't been encapsulated.

$$Encapsulation\ efficiency(\%) = \frac{\Delta H_{NEPCMs}}{\Delta H_{nonadecane} \cdot \frac{nonadecane/styrene}{\frac{nonadecane}{styrene}+1}} \times 100\% \quad (1)$$

where ΔH was the latent heat of the materials; nonadecane/(styrene) was the mass ratio of core (nonadecane) over shell (styrene) in the equation; and $\Delta H_{nonadecane}$ and ΔH_{NEPCMs} were the latent heat of nonadecane and NEPCMs measured by DSC, respectively. So the encapsulation efficiency of NEPCMs mentioned above was 55.9%. The efficiency here was not as high as that of many microencapsulated phase changing materials, but was competitive with some NEPCMs stabilized by molecular surfactants[104].

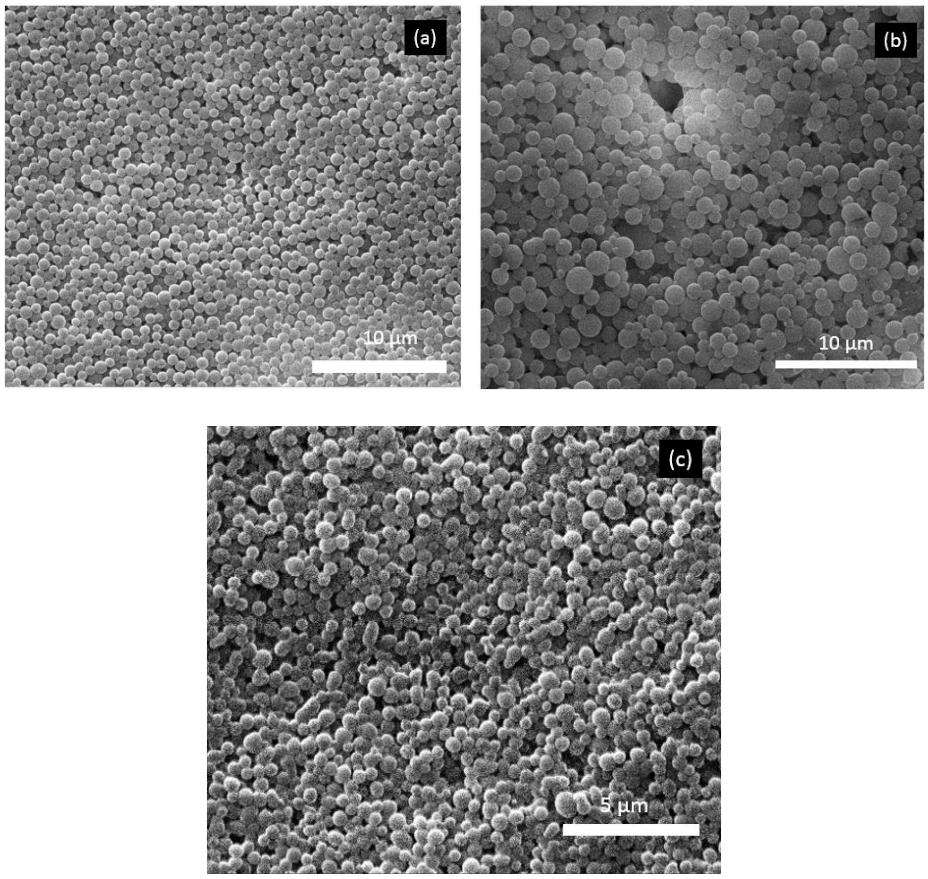

Figure 21. SEM images of NEPCMs with PMMA shell fabricated using three different emulsification mixing methods: (a) Manual shaking; (b) probe sonication; (c) magnetic stirring.

The possible reasons for the relatively low encapsulation efficiency were proposed as following: 1) although the NEPCMs size was relatively uniform, there was a possibility that some NEPCMs had higher nonadecane to PS (nonadecane/PS) ratio and tended to cream to the top of the suspension, and these kind of samples would be discarded in the washing procedure. 2) It was also possible that some of the nonadecane/water emulsions were demulsified in the second emulsification and failed to be encapsulated any more, which would lower the encapsulation efficiency as well. In our experiment, when the

polymerization was finished and the whole samples were cooled down to room temperature, we did noticed that there were a small layer consisted of NEPCMs and waxy nonadecane on the top of the suspensions, we assumed these NEPCMs had a higher nonadecane/PS ratio.

We can easily change the shell material to other polymers by simply applying other monomer for the second step emulsification. PMMA (poly methyl methacrylate) was used as alternative shell material as well. Three different methods were applied for the mixing to emulsify the emulsions. However, we found that the higher energy input didn't improve the quality such as size distribution of the NEPCMs. As we can see in Figure 21, the NEPCMs prepared using general manual shaking produced the best NEPCMs in terms of size distribution.

3.4 Conclusions

In conclusion, a two-step Pickering emulsification procedure was designed to create nano-encapsulated phase changing materials (NEPCMs). The method with simplicity and low energy consumption suggest promise for scale-up and mass production. Surface-modified amphiphilic zirconium phosphate (ZrP) platelets were fabricated as the Pickering emulsifiers, nonadecane was chosen as the core phase changing material and polystyrene, as the shell material. The resultant capsules were submicron in size with remarkable uniformity in size distribution, which has rarely been reported. Differential scanning calorimetry (DSC) characterization showed that the capsulation efficiency of NEPCMs. They were found to be thermal stable, as characterized by the

DSC data for the sample after 200 thermal cycles. This method can be extended to fabrication of other PCMs with various shell materials.

NEPCMs exhibited superior mechanical stability and mobility when compared with the well-developed micro-encapsulated phase change materials (MEPCMs). Also the exterior particle structure can provide extra mechanical integrity for phase changing material. In our case, we apply these materials to reduce the surface tension significantly between oil/water interfaces. Thus, micelles can be easily generated by manually shaking using ZrP-C18 nanoplates as Pickering emulsifier. NEPCMs find useful applications in thermal management, including micro-channel coolants; solar energy storage media; building temperature regulators; and thermal transfer fabrics.

CHAPTER IV

SURFACE MODIFICATION OF LAYERED ZRP WITH PNPAM AND THERMOSENSITIVE PICKERING EMULSIONS

4.1 Introduction

PNIPAM (poly n-isopropylacrylamide)[105] is a synthetic polymer able to respond to external stimuli such as temperature, pH, or ionic environment. It has a liquid critical solution temperature (LCST) of 32 ºC; below this temperature it behaves as hydrophilic material and above 32 ºC, it precipitates out of the water solution thus becoming hydrophobic. This reversible response can be triggered by pH or temperature; consequently, its use in drug delivery and biosensing applications is of great importance. PNIPAM has been previously attached to materials such as graphene[106-108] and slilica cores[109] but it has never been put on layered structures such as ZrP. Moreover, our desire to graft PNIPAM onto the ZrP surface comes from the interspace between layers of ZrP, since it has been reported to serve as the matrix for cisplatin[110], rhodamine[19] and doxorubicin[14] intercalation. Therefore, exploiting the grafting of stimuli-responsive PNIPAM on layered crystals of ZrP is of considerable interest for smart materials as they can create thermoresponsive carriers for anticancer or other type of drugs.

Parts of this section are reprinted with the permission from Chemical Communication: X. Wang, D. Zhao, I. B. N. Medina, A. Diaz, H. Wang, A. Clearfield, M. S. Mannan and Z. Cheng, *Chemical Communications*, 2016, **52**, 4832-4835.

Gamma rays have been reported to serve in both irradiation polymerization[111] and pre-irradiation polymerization[112-114]. By producing peroxide groups which decompose into free radicals to initiate polymerization on the surface of water-suspended organic and inorganic particles, ^{60}Co γ-rays have proved an effective method for grafting polymers onto the surface of polystyrene macromolecular microspheres[113], graphene[112], and imogolite[114], and resulted in crosslinking hydrogels. This is a simple and effective method for inducing polymers growth on the surface of ZrP crystals. It will open a door for polymers modification on ZrP surface, as well as various potential applications of both amphiphilic ZrP nanosheets[27] and surface active layered materials[34].

Layered alpha-zirconium phosphate disks with surface modification of hydrophobic alkane have proved to be useful in stabilization of Pickering emulsions[26] and Pickering encapsulations[27], especially after being exfoliated into nanoplates. In other words, the two unique physical properties— hydrophilicity and hydrophobicity—exist in one single particle. Other surface functionalizations developed on the asymmetric particles include magnetic, catalytic, optical, electrical, or responsive (temperature or pH)[72, 115].

PNIPAM has been investigated for possible applications in tissue engineering and drug delivery[116]. Pure PNIPAM microgel[53], particles of PNIPAM with copolymers[117], or organic particle with PNIPAM grafting have been used as Pickering emulsifiers to stabilize thermosensitive water/oil emulsions[53, 117, 118]. Until now, only limited research in inorganic-based thermosensitive Pickering emulsifiers has been reported[118, 119]. To the best of our knowledge, the inorganic particles were restricted to silica particles. Usually

hydrophobic silica was treated with PNIPAM to become the Pickering emulsifier[120]. Covalently bonding between the inorganic particle and PNIPAM was reported less often in the literature. Yang's group prepared a Janus polymer (PNIPAM)/inorganic (silica) composite nanosheets as Pickering emulsifiers to stabilize thermosensitive O/W emulsions with a high polydispersity[121]. Disk-like thermosensitive Pickering emulsifiers, however, have rarely been reported.

4.2 Experiment

In this section, we present the synthesizing method of ZrP crystalline disks, ^{60}Co γ-rays irradiation to produce peroxide groups and the pre-irradiation polymerization of PNIPAM on the ZrP surface. Ultraviolet-visial spectroscopy (UV-vis), Fourier transform infrared spectroscopy (FTIR), Solid-state nuclear magnetic resonance (SSNMR) as well as thermogravimetric analysis (TGA) were used for characterization of the samples.

4.2.1 Synthesizing of ZrP

ZrP used in this paper were synthesized by the hydrothermal method[6]. Following a typical preparation method, H_3PO_4 (3 M) and zirconium (IV) oxychloride octahydrate ($ZrOCl_2 \cdot 8H_2O$, 10 wt%) were reacted at 200 °C for 5 h to yield a white product. The product was centrifuged, washed three times with deionized water (DI), and dried in the oven overnight at 65 °C. Then it was ground into powder and saved for future use.

4.2.2 Pre-irradiation polymerization for the surface modification

Two grams of dry ZrP powder were suspended in 20 ml DI water for an aqueous ZrP suspension. This suspension was irradiated with ^{60}Co γ-rays (dose rate: 5 kGy/h)

under oxygen flow for 6 h) to generate peroxide groups on ZrP. An aqueous suspension of 5 mL containing 1 ml of irradiated ZrP suspension and 0.1g *N*-isopropylacrylamide monomer (re-crystallized in a mixture of toluene and hexane) were added to a 10-ml test tube with a septum stopper. The mixture was purged via nitrogen bubbling for 20 min. The sealed test tube was then placed in a 50 °C water bath where the free radical polymerization reaction took place for 24 h, allowing PNIPAM grafting on ZrP. The modified ZrP-PNIPAM suspension was washed with DI water for three times.

4.2.3 Proof of the peroxide group produced by ^{60}Co γ-rays irradiation

To determine the amount of peroxide groups produced on the ZrP surface, the classical iodometric method was used [122]. In a particular procedure, 2 mL of irradiated-ZrP suspension was injected into a 50 mL round-bottom three-neck flask, followed by injecting 10 mL of isopropyl alcohol, and further bubbled with nitrogen for 15 min to remove the air before 0.3 g of NaI was added. The suspension was heated and refluxed for 30 min. After the reaction, the yielded suspension was diluted to a total volume of 100 mL. The molar concentration of I_3^- formed was measured with a UV-Vis spectrometer (Shimadzu UV-1800). As a control experiment, the non-irradiated ZrP suspension was also characterized using the same procedure.

To get a direct proof of the successful peroxide groups attachment. Irradiated ZrP suspension was treated by freezing-dry, and then were characterized by FTIR. The FTIR was performed using a Bruker Tensor 27 spectrometer in an attenuated total reflection (ATR) mode with a diamond ATR Prism Model Helios. Non-irradiated ZrP was characterized using same method for comparison.

4.2.4 Proof of attachment of PNIPAM on the ZrP

FTIR, the same procedure as shown in 4.2.3, was used to characterize the non-grafted ZrP and PNIPAM-grafted ZrP (ZrP-PNIPAM) powder. The attachment of PNIPAM chains on the surface of ZrP were also confirmed via CP-MAS (Cross Polarization Magic Angle Spinning) Solid State NMR experiments. The $^{31}P\{^{1}H\}$, CP $^{31}P\{^{1}H\}$ and CP $^{13}C\{^{1}H\}$ MAS NMR experiments were performed with a Bruker Avance-400 spectrometer (400 MHz for ^{1}H nuclei) using a standard 4-mm MAS probe head at a spinning rate of 10 kHz. Standard one pulse (direct nuclear excitation) and/or CP pulse sequences were applied in these experiments at the contact times of 2 (^{13}C nuclei) and 6 (^{31}P nuclei) milliseconds. The external standards used for ^{13}C and ^{31}P NMR experiments were TMS and H_3PO_4 solution, respectively.

Dry samples of pristine ZrP and ZrP-PNIPAM, as well as pure PNIPAM were used for thermogravimetric analysis (TGA, Q500 TA Instrument.) measurements to quantify the amount of PNIPAM grafted onto the surface. The samples were heated from room temperature to 800 °C at a heating rate of 10 °C/min under a mixture of air and N_2 (9:1).

4.2.5 ZrP-PNIPAM Pickering emulsifiers preparation

After ZrP-PNIPAM was synthesized, the sample was lyophilized using a freezing dryer (FD-1A-50, Beijing Boyikang Laboratory Instruments Co., Ltd, China) at 50 °C ($\backsim$15 Pa) for 48 h after preparation. The layered ZrP-PNIPAM aqueous suspension, which was held in a plastic tube, was dipped into liquid nitrogen to allow the water to be frozen suddenly, and the frozen sample was transferred into the freezer dryer where the water

was sublimated into gas under vacuum. A white puff-like sample was obtained after lyophilization.

ZrP-PNIPAM nanoplate Pickering emulsifiers were obtained by exfoliating 1 g of ZrP-PNIPAM in 30-mL water using 2.2 mL 40 wt% tetrabutylammonium hydroxide (TBA^+OH^-). The molar ratio of ZrP to TBA^+OH^- is 1:1; hence, the concentration of ZrP-PNIPAM was about 3.1 wt%. The ZrP nanoplates suspension used in this manuscript for comparison was obtained by exfoliating 1g of ZrP without PNIPAM surface modification following the same procedure.

4.2.6 IFT measurement

IFT was measured using a spinning drop tensiometer (Grace Instrument M6500, USA), using cyclohexane as the oil droplet. For the aqueous phase, both ZrP-PNIPAM and ZrP nanoplates were suspended into DI water at a concentration of 0.09 wt%. The temperature was set to the target temperature and held for 5 minutes before the values were recorded.

4.2.7 Dodecane/water emulsions stabilized by ZrP-PNIPAM

Dodecane in water emulsions were prepared using ZrP-PNIPAM nanoplates as Pickering emulsifiers. One mL dodecane, dyed with magdada red, was mixed with 4 mL DI water in a glass vial. 100 μL of ZrP-PNIPAM suspension was added to be as emulsifier. After manually shaking for about 30 seconds, dodecane was emulsified into the dodecane in water emulsion. The whole suspension was divided into two new vials. One sample

stayed at room temperature, while the other one was put into a 65 °C oven. The stability of these two samples would be record using camera.

4.2.8 Fabrication of PS particles

50 µL of ZrP-PNIPAM suspension as prepared in 4.2.7 was diluted by addition of 950 µL DI water. 100 µL styrene and 0.016g AIBN was added into the diluted ZrP-PNIPAM suspension. Styrene in water emulsions were fabricated by manually shaking in a manner similar to that used for the dodecane/water emulsions in 4.2.7. Then the whole specimen was heated to 65 °C and the polymerization of styrene proceeded for 5 h. The morphology of PS particles was obtained using a scanning electron microscope (FEI Quanta 600 FE-SEM).

4.2.9 Controlled release test

A controlled-release test was carried out using 4-cyano-4'-pentylbiphenyl (5CB) as oil phase. Particularly, 100 µL of 5 CB, 900 µL DI water and 50 µL of ZrP-PNIPAM suspension was mixed together and manually shaken for about 30s. The resulting emulsion suspension were filled into a capillary (diameter: 0.2×4 mm) by capillary force, then the capillary was sealed with epoxy. Then the sealed capillary was investigated under a microscope with crossed polarizer with a temperature-controlled stage. The temperature was set to 40 °C and allowed to rest for about 10 minutes until the temperature became stabile. The capillary was then put on a glass slide (which was used as holder) for investigation under the microscope.

4.3 Results and discussions

The hydrothermal method with 3M phosphorus acid and 5 h reaction time produced thin ZrP. SEM image of ZrP was shown in Figure 22. Individual ZrP disks could be identified easily. The edge of the each ZrP disk was clear.

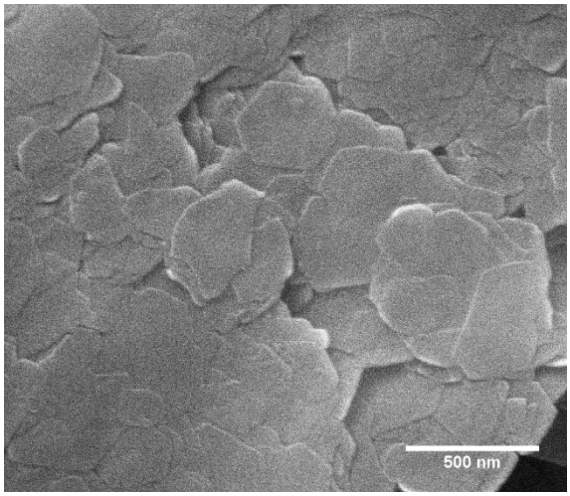

Figure 22. ZrP prepared using hydrothermal method using 3 M H_3PO_4 and reacted for 5 h.

The SEM images of ZrP-PNIPAM are shown in Figure 23. The morphology of ZrP-PNIPAM looked quite different for the specimens prepared by different before taking SEM. Two drying methods were applied to obtain samples for SEM. Indicated in Figure 23 (a, b), the SEM image was taken on the sample that was a drop of ZrP-PNIPAM suspension and dried in the air at room temperature. A surface indicated the successful PNIPAM polymer grafting on the ZrP surface.

Figure 23 (c, d) indicated the surface morphology of ZrP-PNIPAM after freezing dried. Individual particle could be found, but the edge were not as clear as we obtained from pristine ZrP, as shown in Figure 22, we believe that was due to the PNIPAM polymer on the surface.

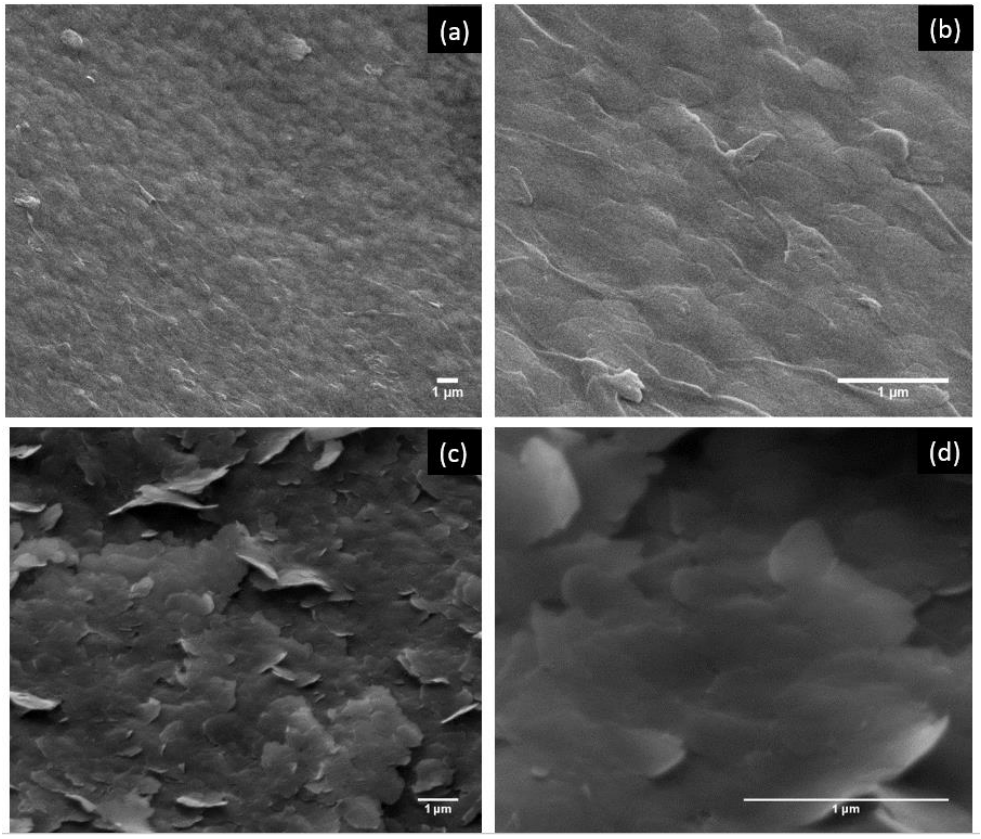

Figure 23. SEM images of ZrP-PNIPAM. (a, b) sample was dried in room temperature; (c, d) Freezing dry sample.

Dynamic light scattering (DLS) had been used to measure the size of ZrP and ZrP-PNIPAM particles, as shown in Figure 24. The size of pristine ZrP was

295±134nm, after grafting with PNIPAM, the particle size increased to 531±200nm.

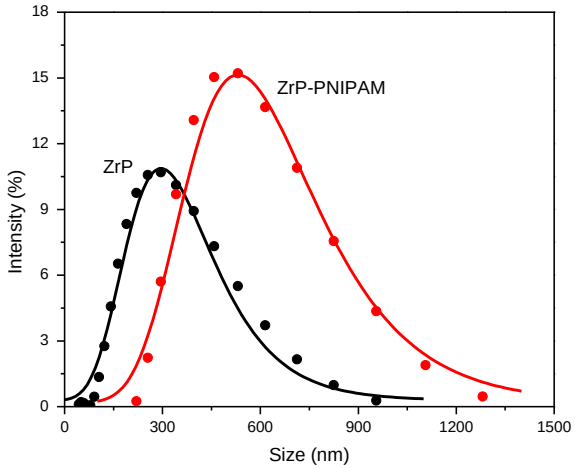

Figure 24. Size of ZrP and ZrP-PNIPAM measured by DLS.

Figure 25 shows the UV-Vis spectra of iodine (in the form of I_3^-) produced in the irradiated ZrP and the control sample (non-irradiated ZrP) after reacting with sodium iodide (NaI). The peaks at 293 nm and 361 nm indicate the existence of I_3^-, which was produced by the oxidation of I^- to I_2. The I_2 concentrations in irradiated ZrP and non-irradiated ZrP were 0.0144 mol/L and 0.000391 mol/L, respectively, the irradiated sample produced about 37 times more I_2 than the non-irradiated one. The small amount of I_2 in the non-irradiated ZrP might be due to ambient oxygen, which can oxidize some I^- to I_2, as it was difficult to avoid contact with air during the sample dilution procedure and UV-Vis measurements.

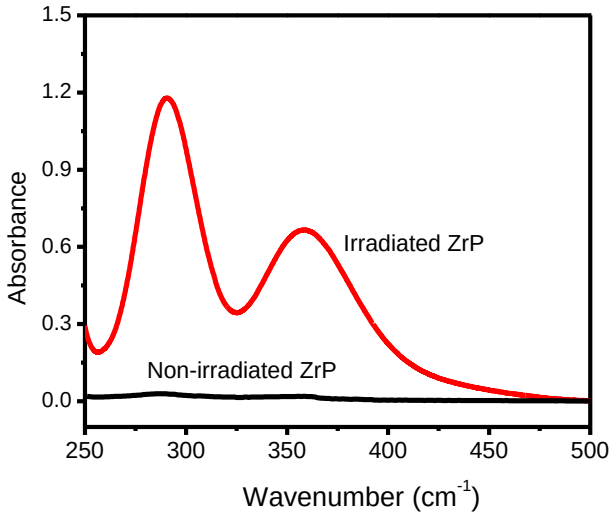

Figure 25. UV-Vis spectra of the irradiated and non-irradiated ZrP suspensions after reacting with NaI.

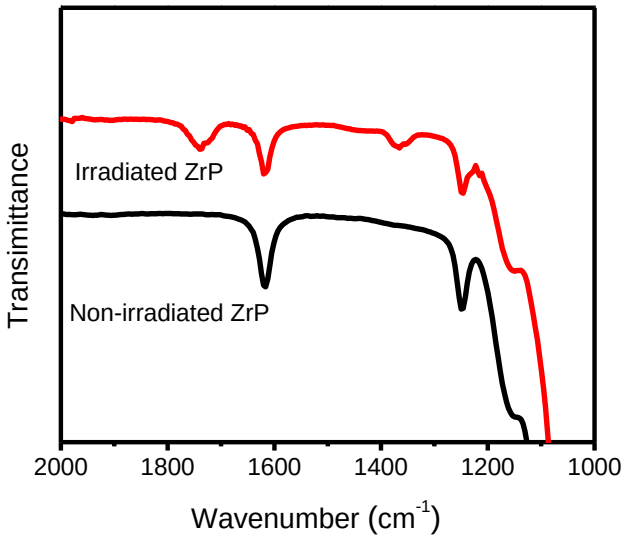

Figure 26. FTIR spectra of the irradiated and non-irradiated ZrP.

The FTIR spectra for irradiated and non-irradiated ZrP are shown in Figure 26. Two more peaks in the irradiated ZrP sample at 1735 and 1365 cm^{-1} are assigned to the new phosphorus peroxide group O=P(OOH)- produced during the irradiation procedure.

Figure 27 shows the procedure for the grafting of PNIPAM onto the surface of ZrP. The –OH terminal group on the surface of ZrP[26] allows the production of peroxide groups –(OOH) upon exposure of the suspension to ^{60}Co γ-rays irradiation under bubbling oxygen gas, and the peroxide groups were produced randomly on ZrP surface after irradiation. The peroxide groups on the ZrP surfaces decompose upon heating to generate radicals, which initiates the grafting polymerization of N-isopropyl acrylamide monomers to yield PNIPAM chains grafted onto the disks.

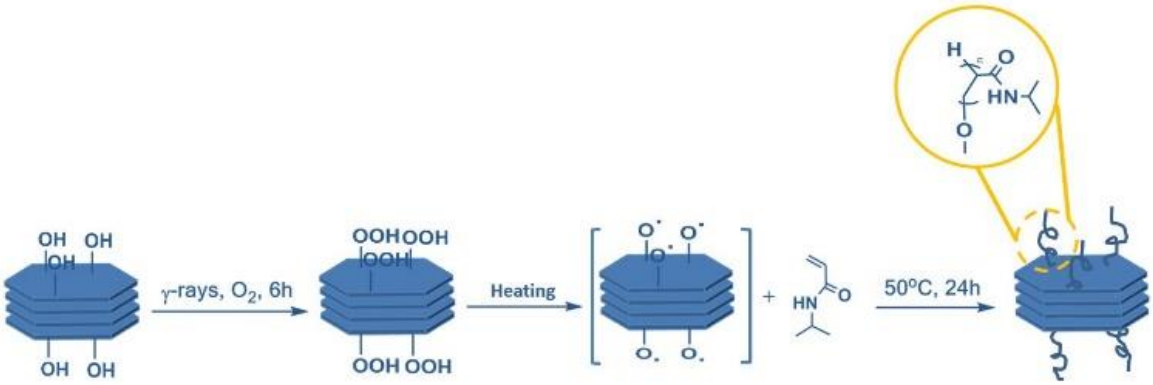

Figure 27. Proposed mechanism for the surface modification of ZrP disks for PNIPAM grafting.

We claimed the polymerization was a normal free radical polymerization procedure due to the type of peroxide initiators employed here, and the reaction was very fast at the beginning, started from the point when free radicals were produced. The comparison of non-grafted ZrP and PNIPAM-grafted ZrP (ZrP-PNIPAM) (red line) FTIR

spectra is shown in Figure 28. We observed the presence of new and characteristic bands for the attachment of PNIPAM chains and we assigned them as follows: 3254 cm^{-1} (secondary amide N-H stretching), 2864 to 2964 cm^{-1} (-CH_3 asymmetric and symmetric stretching), 1629 cm^{-1} (secondary amide C=O stretching), and 1533 cm^{-1} (secondary amide N-H bending).

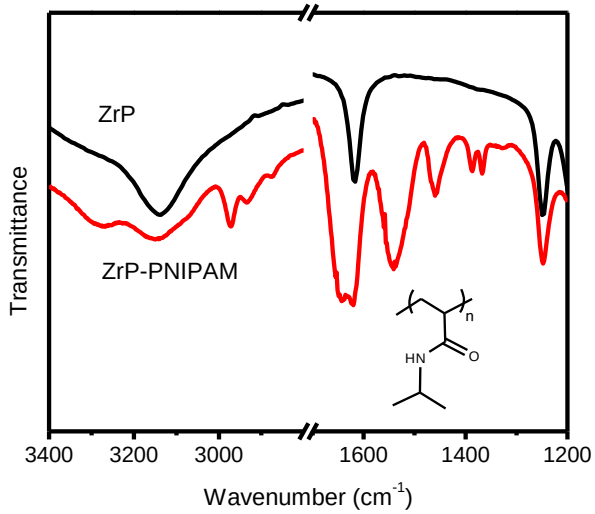

Figure 28. FTIR spectra of the pristine ZrP (black) and PNIPAM-grafted ZrP (red).

The CP $^{31}P\{^1H\}$ MAS NMR spectrum of the compound (Figure 29a) shows two resonances at -18.8 and -20.5 ppm. The most intense signal at -20.5 ppm can be assigned to the orthophosphate group of ZrP. The orthophosphate group consists of a phosphorus atom bonded to three Zr atoms through three oxygen atoms. The weak resonance at -18.8 ppm is also characteristic of ZrP. There are no dramatic changes ongoing from CP to the spectrum obtained by direct excitation (see the $^{31}P\{^1H\}$ MAS NMR spectrum (Figure 29a). Only a non-intense shoulder appears at -22/ -23 ppm. This shoulder is better seen by

subtraction of the CP $^{31}P\{^{1}H\}$ spectrum from the $^{31}P\{^{1}H\}$ spectrum in Figure 29a. Typically this non-intense shoulder could be assigned to the dehydrated phase of ZrP and/or to a P-O-C linkage in a modified ZrP surface. Given that our sample was polymerized in water (≤ 50°C) and dried at 70°C, we can safely assume that this signal should belong to the P-O-C linkage in a modified ZrP surface and confirms the attachment of the polymer chains.

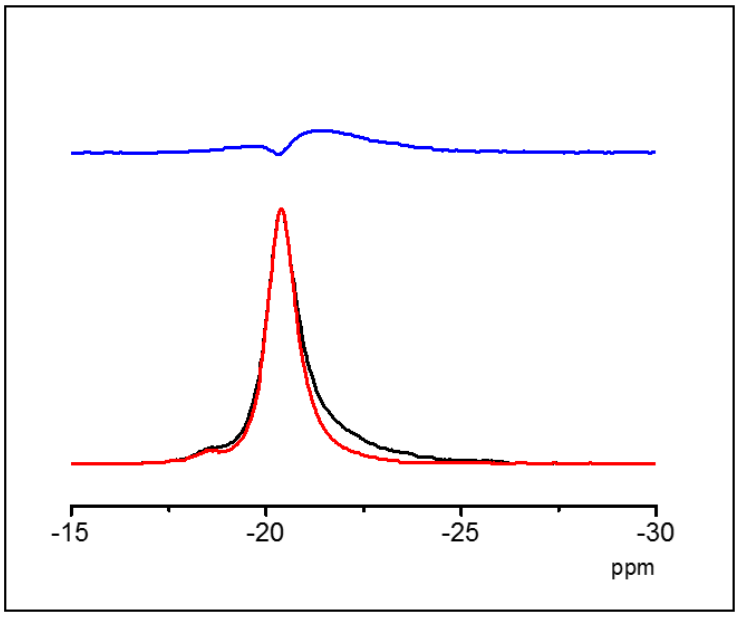

Figure 29. The $^{31}P\{^{1}H\}$ (black) and CP $^{31}P\{^{1}H\}$ (red) MAS NMR spectra recorded at a spinning rate of 10 kHz in a sample of ZrP- PNIPAM(bottom). Subtraction of the CP $^{31}P\{^{1}H\}$ spectrum from the $^{31}P\{^{1}H\}$ spectrum (top).

The ^{13}C CP MAS NMR spectrum (Figure 30) shows resonances at 174.8, 41.1, 34.1, and 22.2 ppm, corresponding to polymer units. According to the layered nature of our material and low coverage, the peaks showing the chemical bonding between the polymer and ZrP are weak (interpretation of $^{31}P\{^{1}H\}$ MAS NMR), thus the corresponding

^{13}C NMR peaks may be masked by the intense peak at 41.1 ppm. Nevertheless, the presence of the other peaks qualitatively confirms the presence of polymer units.

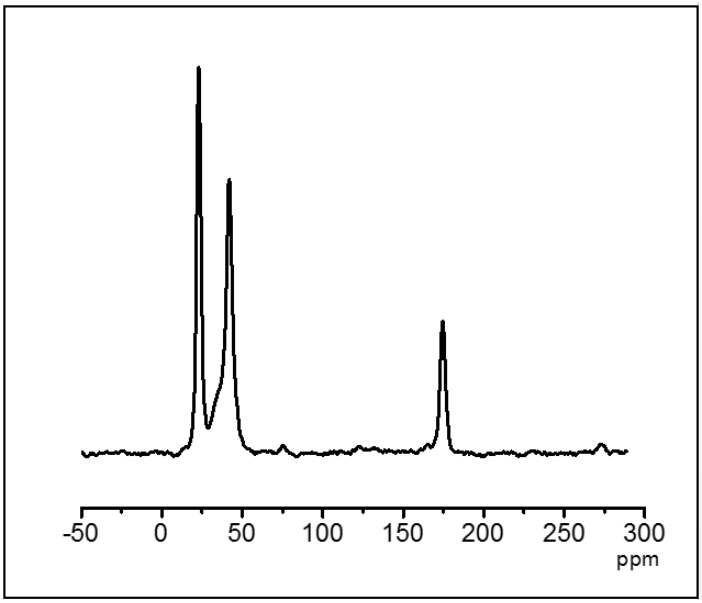

Figure 30. The CP ^{13}C {^{1}H} MAS NMR spectrum recorded at spinning rate of 10 kHz.

The randomness of peroxide groups on ZrP by ^{60}Co-γ irradiation would initiate free radical polymerization randomly on the particle surface, we assumed the PNIPAM chains were homogenously distributed on layered ZrP. Dynamic light scattering measurement measured the size of ZrP and ZrP-PNIPAM to be 295±134nm and 531±200nm respectively (Figure 24). By simply estimation, we calculated the thickness of PNIPAM layer on the ZrP to be 118nm.

To further identify the mass ratio of PNIPAM to ZrP, dry samples of pristine ZrP and ZrP-PNIPAM, as well as pure PNIPAM were used for thermogravimetric analysis (TGA, Q500 TA Instrument) measurements to quantify the amount of PNIPAM grafted

onto the surface (Figure 31). The samples were heated from room temperature to 800 °C at a heating rate of 10 °C/min under a mixture of air and N_2 (9:1). The total weight loss of pristine ZrP was about 12%, with two major weight losses wherein the sample was completely dehydrated (first loss at 100 °C) and the condensation of the phosphate groups (second loss at 500 °C). The phosphate groups was condensed to the end product zirconium pyrophosphate [$Zr(O_3POH)_2 \cdot H_2O(s)$ + heat (700°C) → $2H_2O(g)$ + $ZrP_2O_7(s)$] [31] .The pure PNIPAM was burned away below 600°C in three steps.

The weight loss of the modified ZrP-PNIPAM sample occurred in three events, as is found in similar organically modified ZrP materialsm[26, 31, 34], and the total weight loss was 38%, with a total weight loss of 38% [$(C_6H_{11}NO)_n$@$Zr(O_3POH)_2 \cdot H_2O(s)$ + heat (up to 700°C) → $2H_2O(g)$ + $ZrP_2O_7(s)$ + $CO_2(g)$ + $NO_x(g)$]. All solvent (water here) is expected to be lost below 150 °C. The resulting weight loss occurring anywhere from 200°C to 400°C is presumably the loss of the PNIPAM. Finally, the condensation of the monohydrogenphosphate to the pyrophosphate occurs roughly between 450°C and 600°C which also concedes with the final PNIPAM weight loss. By calculating from the amount of the final product, 62% here, we were able to estimate the amount of ZrP through the reaction shown above, which is 70.4% out of the total ZrP-PNIPAM sample. As a result, the surface coverage of ZrP with PNIPAM was 29.6%.

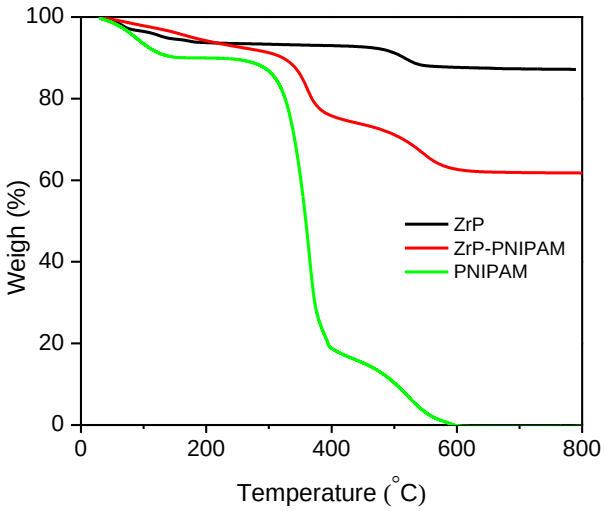

Figure 31. TGA of pristine ZrP (black) and pure PNIPAM (green) along with ZrP-PNIPAM (red).

In summary, by using ^{60}Co-γ irradiation under oxygen flow, we have successfully produced peroxide groups on the layered ZrP. To the best of our knowledge, this is the only method to induce peroxide groups onto layered ZrP so far. These peroxide groups would act as initiator to initiate NIPAM monomer directly onto the ZrP surface later upon heating. The PNIPAM chains were proved to be connected to layered ZrP via covalent band (−P−O−C−). This is a new method to functionalize inorganic layered ZrP with polymers, it can be suitable for other layered inorganic particles and other water soluble monomers as well, and will eventually contribute to the inorganic-polymer composites study and their applications.

Layered ZrP-PNIPAM was exfoliated into Janus and Gemini nanoplates using an intercalation agent, tetrabutylammonium hydroxide (TBA^+OH^-). As shown in Figure 32,

for each layered ZrP-PNIPAM, two Janus nanoplates and several Gemini nanoplates, depending on the number of layers, were obtained after exfoliation. The tetrabutylammonium ion (TBA^+), as well as PNIPAM, was attached to the surface of ZrP via electrostatic interaction due to the hydroxide (−OH) groups between the ZrP layers, enabling layered ZrP-PNIPAM to be exfoliated.

The thickness of the ZrP layers used here was about 10 nm, hence about 15 nanoplates were produced from each layered ZrP, since the monolayer ZrP was 0.68 nm. Hence, the ZrP-PNIPAM suspension contained about 13% Janus and 87% Gemini nanoplates after exfoliation. As we discussed in previously, the thickness of PNIPAM layer was 118 nm. The intercalation agent TBA^+ thickness was about 1 nm, which was much smaller than the PNIPAM chains.

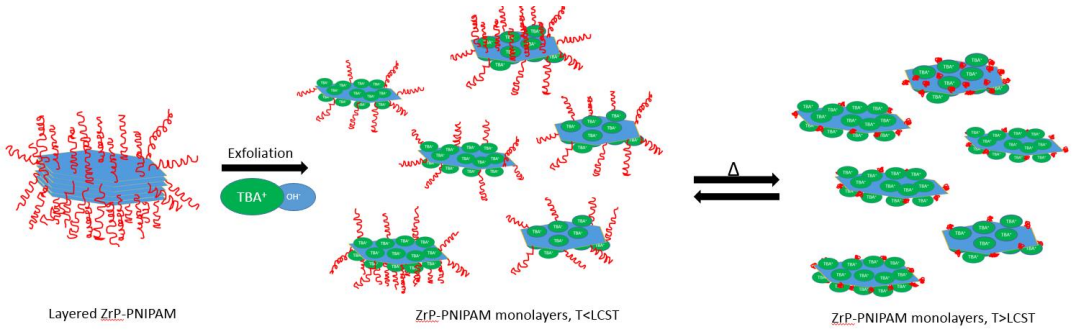

Figure 32. Exfoliation of layered ZrP-PNIPAM into Janus and Gemini nanoplates.

The size (hydrodynamic diameter) of monolayer ZrP-PNIPAM nanoplates was measured using DLS, as shown in Figure 33. The size of ZrP-PNIPAM nanoplates was around 500 nm at temperatures below 30 °C. The size suddenly decreased to around 300 nm as temperature increased from 30 °C to 35 °C. The sudden size decrease of ZrP-

PNIPAM nanoplates as temperature decreased was due to the attached PNIPAM experiencing a lower critical solution temperature (LCST), around 32 °C, as shown in Figure 32. As temperature climbed higher than LCST, the PNIPAM suddenly collapsed onto the ZrP surface. The monolayer ZrP-PNIPAM had a temperature-responsive property in range of 30 °C to 35 °C. At temperatures above 35 °C, PNIPAM grafting did not increase the size of ZrP-PNIPAM nanoplates compared to ZrP without modification due to the shrinking of PNIPAM chains.

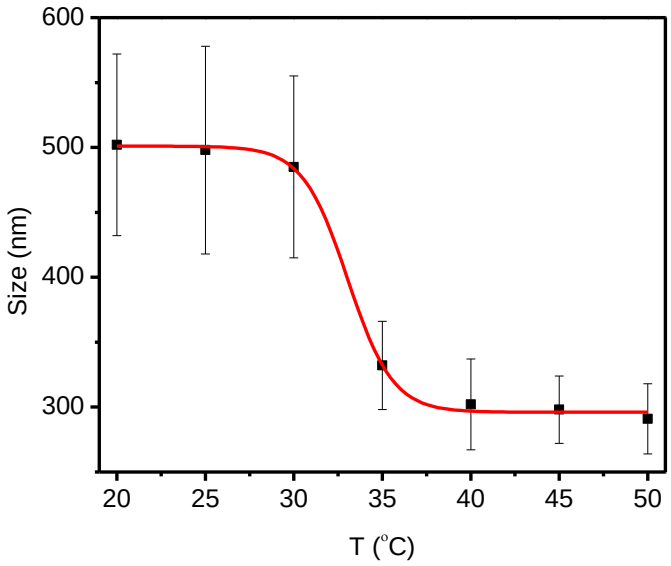

Figure 33. Size of monolayer ZrP-PNIPAM as a function of temperature measured by DLS.

The oil/water interfacial tension (IFT) is one of the most important parameters characterizing surfactants, especially in the water flooding of enhanced oil recovery (EOR) [123]. Usually, for surfactants used for producing O/W emulsions, the smaller a surfactant's IFT, the better the emulsifier performance as surfactant. As to the Pickering

emulsifiers, the ability to reduce IFT was still a useful parameter to determine emulsifier capability[124].

The interfacial tension between cyclohexane and water in the presence of ZrP-PNIPAM or exfoliated ZrP nanoplates was measured by spinning drop tensiometer (Grace Instrument M6500, USA) at various temperatures (Figure 34). The concentration of both nanoplates was 0.09 g/mL. The IFT of pure cyclohexane/water was reported to be in the range of 48 mN/m to 51 mN/m [125], decreasing inversely with temperature [126]. By addition of exfoliated ZrP nanoplates into the aqueous phase, the IFT was greatly reduced to 12.2 ± 0.3 mN/m, and again, the IFT value decreased as temperature increased. The situation was much different when ZrP-PNIPAM nanoplates were added into the suspension; in this case, the IFT was further reduced overall to about 2.1 ± 0.3 mN/m. More importantly, the trends were quite different in the ZrP-PNIPAM suspension. From 25 °C to 30 °C, the IFT slightly decreased. As the temperature increased further, the IFT suddenly increased at 35 °C, and the IFT kept increasing with temperature.

The IFT of the ZrP-PNIPAM suspension was less than that of ZrP nanoplates suspension, indicating that the PNIPAM modification endowed the ZrP nanoplates with more hydrophobicity. Hence, we concluded that PNIPAM chains would be more likely to stay in the oil phase instead of in the aqueous phase compared to TBA^+. The sudden IFT increase at 35 °C was consistent with the LCST of PNIAM, so we concluded that the PNIPAM shrinking at temperatures above its LCST caused an increase in IFT of the ZrP-PNIPAM suspension. To the best of our knowledge, this is the first quantitative measurement of an increasing IFT across the LCST of PNIPAM.

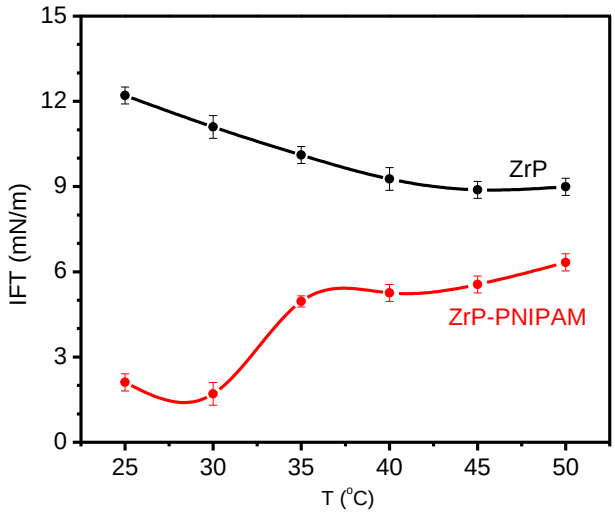

Figure 34. IFT of ZrP-PNIPAM and ZrP nanoplates as a function of temperature.

The ability to reduce IFT indicated that ZrP-PNIPAM nanoplates can be used as a Pickering emulsifier. Oil/water emulsions have been stabilized using ZrP-PNIPAM nanoplates alone (Figure 35); for instance, dodecane/water emulsions can be easily emulsified by gentle manual shaking using ZrP-PNIPAM as emulsifiers. A temperature-responsive capacity was also obtained by noting the visible change from the photos: the dodecane/water emulsions were totally coalesced after sitting in an oven at 65 °C oven for just 5 minutes. This was due to the temperature responsive property of PNIPAM chains grafting on the Pickering emulsifiers. As the temperature exceeded LCST, the change of PNIPAM would lead to the coalescence of emulsions, as already indicated by the increasing IFT as discussed above.

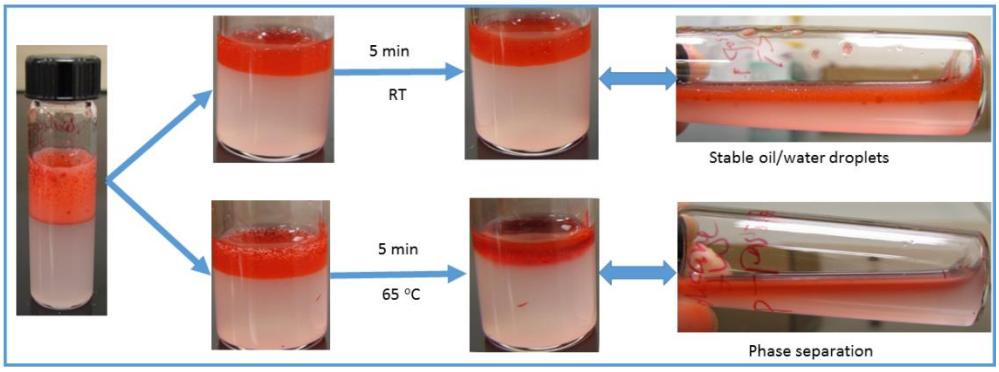

Figure 35. The stability of dodecane (magdala red)/water emulsions stabilized via ZrP-PNIPAM nanoplates at room temperature and 65 °C.

To further study the behavior of oil/water emulsions stabilized by ZrP-PNIPAM nanoplates, polystyrene (PS) particles were fabricated and imaged by SEM. First, styrene together with initiator (AIBN) in water emulsions were obtained by manual shaking using ZrP-PNIPAM as Pickering emulsifier. The whole specimen was then heated to 65 °C to allow the polymerization of styrene. The morphology of PS particles would somehow indicate the oil/water emulsions stabilized by ZrP-PNIPAM nanoplates. The total volume used for the emulsification procedure here was 1 mL, and the sample was set in a 65 °C oven right after emulsification, which would enable instant decomposition of the initiator, azobisisobutyronitrile (AIBN). Hence, the polymerization occurred right after emulsification. In this case, the styrene/water emulsions were "frozen" so that their morphology could be well studied.

The PS particle precursor (monomer together with initiator in water droplets) was emulsified at temperatures below and above LCST of PNIPAM, room temperature (around 20 °C) and 65 °C, respectively, to study the temperature-responsive performance

of ZrP-PNIPAM emulsifiers. As shown in Figure 36, the PS particles emulsified at 65 °C were much larger and much more polydispersed overall than PS particles emulsified at room temperature. The PS particles emulsified at room temperature were less than 1 μm in diameter while the size of PS particles emulsified at 65 °C ranged widely, from several micrometers to tens of micrometers.

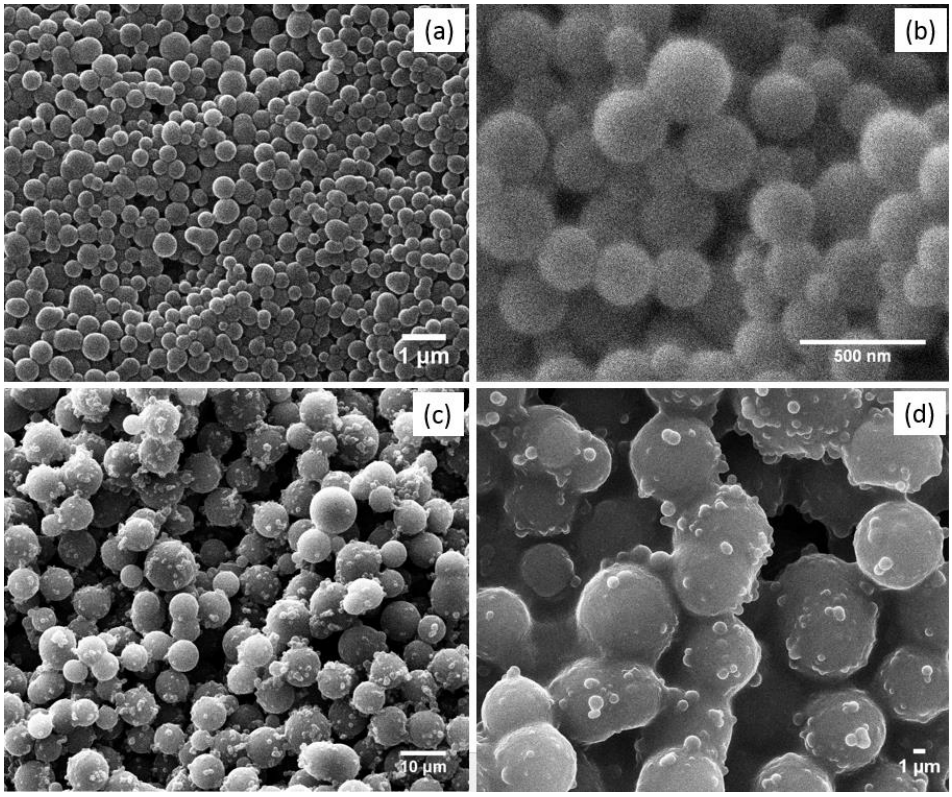

Figure 36. SEM images of PS particles stabilized by ZrP-PNIPAM nanoplates at room temperature (a, b) and 65 ^{o}C (c, d).

The great difference apparent between the PS particles prepared at room temperature and those prepared at 65 °C indicates the different emulsification capability of ZrP-PNIPAM nanoplates at temperatures below and above LCST of PNIPAM. The

results were consistent with their IFT values as well. At room temperature, the IFT of the mixture was greatly reduced by addition of Pickering emulsifier ZrP-PNIPAM nanoplates, and the styrene/water emulsions were small. Even after heating procedure, the PS particles were still relatively uniform. The IFT of ZrP-PNIPAM suspension increased, however, and the emulsions more coalesced easily, producing larger-size emulsions, which resulted in larger PS particles.

Due to the temperature responsive property, PNIPAM has been applied in various controlled-release fields [116] .A controlled-release behavior of the emulsions stabilized by ZrP-PNIPAM nanoplates was carried out using 4-cyano-4'-pentylbiphenyl (5CB) as model material. 5CB, a hydrophobic material with birefringence property under crossed polarized microscopy, was used as the oil phase. After mixing 5CB, ZrP-PNIPAM nanoplates, and water, the mixture was shaken manually for emulsification, resulting in 5CB in water emulsion droplets. The emulsions were filled into a capillary and then sealed with epoxy. The capillary was observed under crossed polarized microscopy with a temperature-controlled stage. As shown in Figure 37, once the temperature was switched to 40 °C, the droplets began to coalesce, merge, and enlarge with time. Finally, all droplets were broken and coalesced into a bulk oil phase after 240 seconds. In other words, by switching temperature, from below to above LCST, the model material was fully released after 4 minutes. If the droplets were saved under room temperature, however, they were quite stable. As shown in Figure 37b, the 5CB emulsions did not show significant difference even after 20 days' aging.

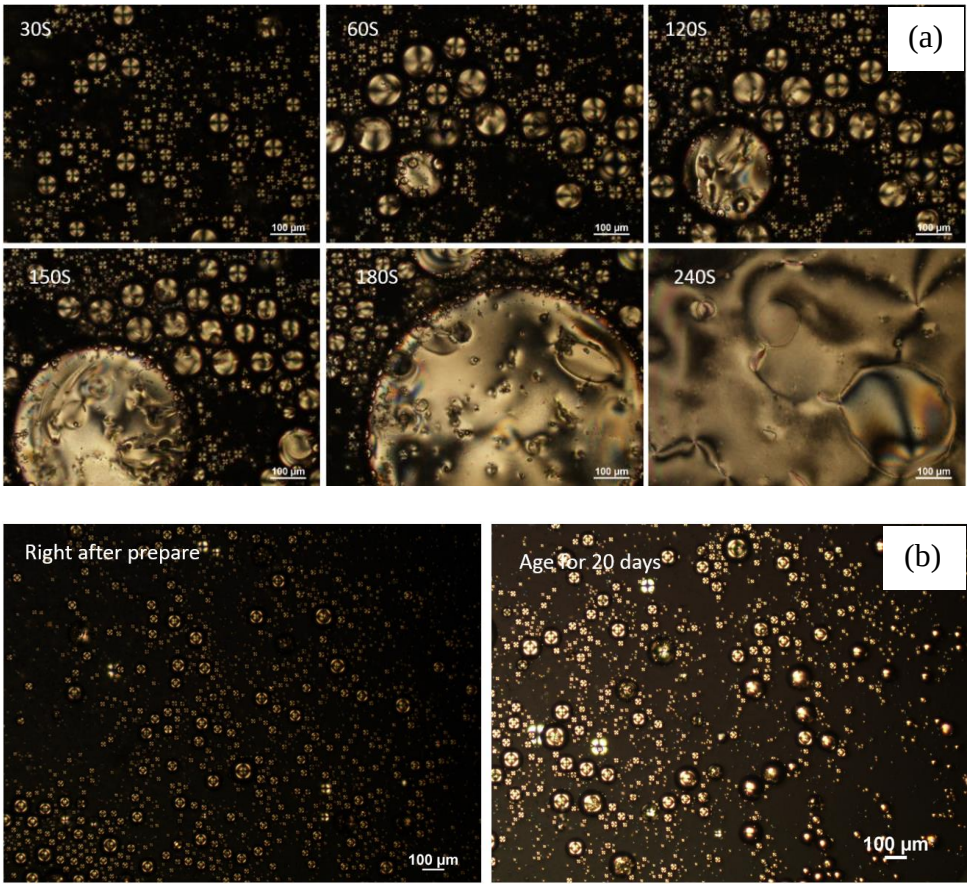

Figure 37. Controlled release test of ZrP-PNIPAM using model material. The droplets stabilized by ZrP-PNIPAM nanoplates were investigated at (a) 40 °C and (b) room temperature. The (a) group images were taken at the same location at 40 °C.

As discussed above, ZrP-PNIPAM nanoplates could serve as a good Pickering emulsifier candidate. The oil/water emulsions stabilized by ZrP-PNIPAM remained stable for a long period of time. The emulsions, however, were coalesced immediately as temperature rose, and totally broken in 4 minutes. Hence, we believe that ZrP-PNIPAM is an ideal emulsifier for controlled release applications since it is able to fabricate stable oil droplets with fast response.

4.4 Conclusions

In summary, by using ^{60}Co-γ irradiation under oxygen flow, we have successfully produced peroxide groups on the metal phosphate ZrP crystalline disks. These peroxide groups would act as initiator to graft PNIPAM directly onto the disk surface. This is a new method to functionalize metal phosphates particles with polymers with covalently bonds, and will contribute to the inorganic-polymer composites study and applications.

Asymmetric ZrP-PNIPAM nanoplates have been fabricated and proved to be thermosensitive Pickering emulsifiers. The nanoplates first showed the capability of reducing IFT at oil/water interface, and then the ability to produce stable oil/water emulsions. The nanoplates also proved to be temperature-responsive. For the first time, quantitative measurement showed IFT increasing with temperature above LCST of PNIPAM. In additional, the PS particles emulsified by ZrP-PNIPAM were much larger and far more polydispersed when the emulsified temperature was above the LCST of PNIPAM compared to those at temperature below LCST. A controlled-release experiment was realized by investigating the coalescence behavior of oil droplets stabilized by ZrP-PNIPAM nanoplates, when being heated to 40 °C. The resuαlts indicated that the droplets were stable at room temperature but would be “released” easily at 40 °C. Hence, we conclude that ZrP-PNIPAM nanoplates can be a very good candidate as thermosensitive Pickering emulsifier for controlled release areas, for example, in drug delivery.

CHAPTER V

SURFACE MODIFICATION OF EXFOLIATED ZRP MONOLAYERS WITH PNIPAM AND THERMOSENSITIVE DISCOTIC LIQUID CRYSTALS

5.1 Introduction

Liquid crystals are anisotropic fluids, which can be from by anisotropic (discotic, bowlike and rod-shaped) molecules (particles). The liquid crystal materials exhibit spontaneous orientational order is nematic phase. Since Langmuir discovered in 1938 that clay particles exhibit a discotic nematic phase [127], discotic liquid crystals of colloidal suspensions have been a growing field of scientific investigation [128]. Onsager predicted platelets could make an isotropic-to-nematic (I-N) transition [129]. Computer simulations of the I-N transition have been performed for discotic particles with different aspect ratios [130]. Lekkerkerker et al. obtained different liquid crystal phases, including nematic and columnar phases, from toluene suspensions of discotic gibbsite particles [131]. Graphene oxide aqueous suspensions have also been investigated for the formation of liquid crystals [132]. Temperature-sensitive colloidal crystals of spheres show a long history of study.

Monodispersed PNIPAM spheres have been used to investigate crystallization and melting by changing temperature [133, 134]. Temperature-sensitive discotic liquid crystals, however, had not been realized before. Our group studied charged ZrP platelets of various

---

sizes to investigate the I-N phase transition [135].

Here, we grafted PNIPAM onto the ZrP platelets to obtain thermo-sensitive discotic liquid crystals. By adjusting the temperature, we were able to vary the aspect ratio of the ZrP-PNIPAM so that we could study the aspect ratio dependence of the I-N transition. Our results showed that the phase diagram of ZrP-PNIPAM was consistent with that predicted by the Onsager-Parsons theory, and the nematic phase shows up at a higher aspect ratio in soft disks than in hard disks.

5.2 Experiment

5.2.1 Synthesis of ZrP

Hexagonal α-ZrP crystals with multiples layers were synthesized by the hydrothermal method. ZrP platelets (around 1 μm in diameter) were obtained by exfoliating 1g of α-ZrP crystals in 30 mL water using 2.2 mL 40%wt tetrabutylammonium hydroxide (TBA^+OH^-). The molar ratio of ZrP to TBA^+OH^- is 1:1. The aqueous ZrP platelets suspensions with a concentration of 0.03 g/mL were then irradiated with ^{60}Co γ-rays (dose rate: 5 kGy/h) under oxygen flow for 6 h to generate peroxide groups on the surface of the ZrP platelets.

5.2.2 Pre-irradiation of ZrP monolayers suspensions

An aqueous suspension of 5 mL containing 2.5 mL of ^{60}Co γ-rays irradiated ZrP platelets and 0.1 g *N*-isopropyl acrylamide (re-crystallized in a mixture of toluene and hexane) were added to a 10-mL test tube with a septum stopper. The mixture was purged with nitrogen bubbling for 20 min. The sealed test tube was then placed in a 50°C water

bath, where the polymerization reaction continued for 24 h. The produced ZrP-PNIPAM platelets were centrifuged, washed with deionized water twice, and re-suspended in water for further analysis.

5.2.3 Graft PNIPAM onto ZrP monolayers

ZrP-PNIPAM suspensions of 1 mL with different particle concentrations were prepared by diluting a mother sample with deionized water. The samples were then put into an oven (Napco vacuum oven, Model 5831) with the target temperatures (20°C, 35°C, and 50°C) under atmospheric conditions. Sample photographs were taken with sample set briefly outside the oven between a cross-polarizer and a fluorescent light shining from behind.

5.2.4 Characterization of ZrP-PNIPAM monolayers

In order to prove the successful PNIPAM grafting onto exfoliated ZrP monolayers, characterizations were performed similar to those done for the layered ZrP. Basically, UV-Vis were used to prove the successful production of peroxides groups on the exfoliated ZrP monolayers surface. And FTIR was used to prove the attachment of PNIPAM on exfoliated ZrP.

DLS was used to measure the particles size of ZrP-PNIPAM monolayers at different temperatures. In the measurement, the temperature was set to target temperature and equilibrant for 5 mins before we do the measurement.

5.2.5 Conversion of ZrP-PNIPAM monolayers concentration to volume fraction

The volume fractions for the mother suspension was calculated as follows: weighting out a certain volume (V_1) of ZrP-PNIPAM suspension (m_1) and let the water evaporate to m_2 at 50 °C oven, with the weight difference assumed to be free water in the sample. We found the following: the mass of water M is equal to m_1-m_2, the volume of water V_2 is equal to M/ρ, where ρ is the density of water, 1 g/mL. Then we get the volume fraction of the ZrP-PNIPAM sample at 50 °C as ϕ which is equal to (V_1-V_2)/V_1.

The volume fraction at 20°C and 30°C were converted from their volume fraction at 50°C based upon the thickness ratio since the lateral size was fixed. As we know, the thickness of the ZrP-PNIPAM at 20°C and 30°C was 23.4 and 15.9 times more, respectively than that at 50°C. The volume fraction of platelets was proportional to their thickness; hence, we obtained volume fractions of the samples at 20°C and 30°C by multiplying their volume fractions at 50°C by 23.4 and 15.9, respectively.

The set of samples for liquid crystal phase diagram were diluted from the mother suspension, so their volume fractions were calculated based on the volume fraction of mother suspension. For example, in a case of the sample with 50% percent dilution (0.5 mL mother suspension addition to 0.5 mL DI water), the volume fraction of this sample is half that of the mother suspension.

5.3 Results and discussion

Pristine layered α-ZrP prepared via hydrothermal method was hexagonal in shape, and the size was around 1μm, as shown in Figure 38. ZrP Monolayers can be obtained by exfoliating with tetrabutylammonium hydroxide (TBA^+OH^-) in deionized (DI) water. The

size distribution of ZrP monolayers was shown in Figure 39. By Fitting into extreme distribution using peak function, we get the polydispersity of the ZrP sample, σ=24±2%. The size was measured to be 964.5 ±231 nm using DLS.

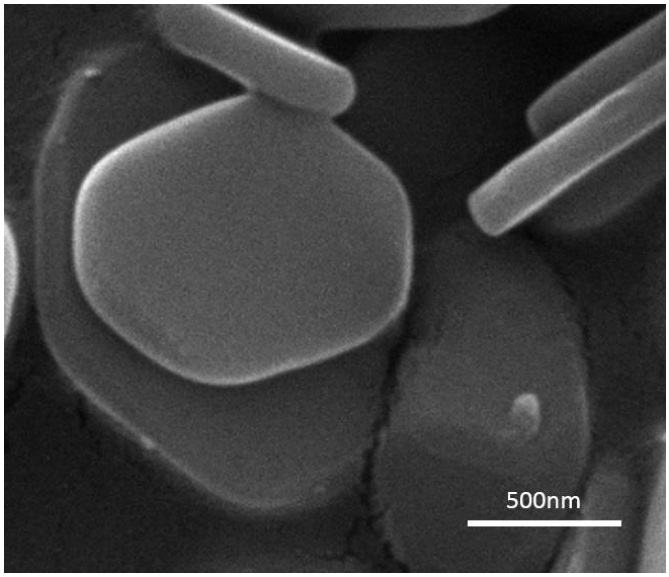

Figure 38. SEM image of the pristine ZrP by hydrothermal method of 12M H_3PO_4 and reacted for 24 h.

Pre-irradiation method was used to prepare the ZrP-PINPAM platelets. Aqueous TBA^+OH^- exfoliated ZrP platelet suspensions were first irradiated with ^{60}Co γ-rays under O_2 ambience to produce peroxide groups on the ZrP surfaces. The peroxide groups were later decomposed into free radicals by heating, enabling the initiation of polymerization of N-isopropylacrylamide monomers to form PNIPAM polymers, as we discussed in Chapter IV.

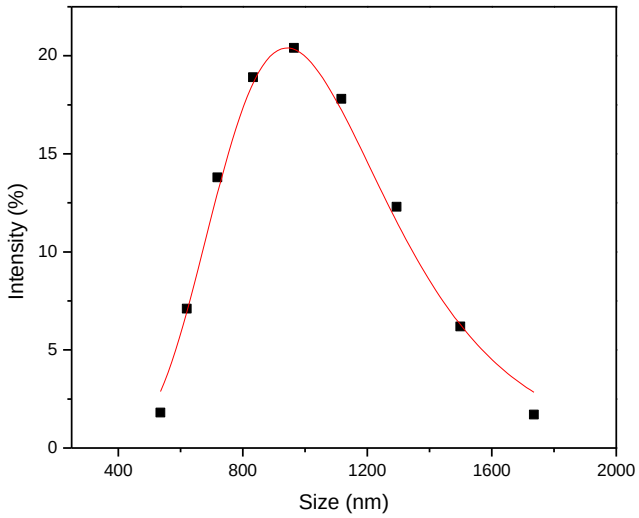

Figure 39. Size distribution for exfoliated ZrP monolayers as measured by DLS. The lines are fit to the extreme distribution function.

To determine the amount of peroxides produced on the ZrP platelet surface, the classical iodometric method was performed. 2 mL of irradiated ZrP suspension was injected into a 50 mL round-bottom three-neck flask, followed by injecting 10 mL of isopropyl alcohol, and further bubbled with nitrogen for 15 min to remove the air before 0.3 g of NaI was added. The suspension was heated and refluxed for 30 min. After the reaction, the yielded suspension was diluted to a total volume of 100 mL. The molar concentration of I_3^- formed was measured with a UV-Vis spectrometer (Shimadzu UV-1800). As a control experiment, a ZrP platelet suspension without gamma-rays irradiation was also reacted with NaI, diluted, and measured with UV-Vis as well.

Figure 40 shows the UV-Vis spectra of the amount of iodine produced using the gamma irradiated ZrP platelets and the control sample with non-irradiated ZrP platelets. After reacting with NaI, the peaks at 293 nm and 361 nm indicate the existence of I_2, which is produced by oxidation of I^-. The absorption peaks show that the amount of I_2 produced by gamma irradiated ZrP platelets (solid line) is much greater than the amount of I_2 produced by the control (dashed line). The small absorption peaks of the dashed line might be due to the oxygen from the air, which can oxidize some I^- to I_2, as it was difficult to avoid contact with air during the sample dilution procedure and the UV-Vis measurements.

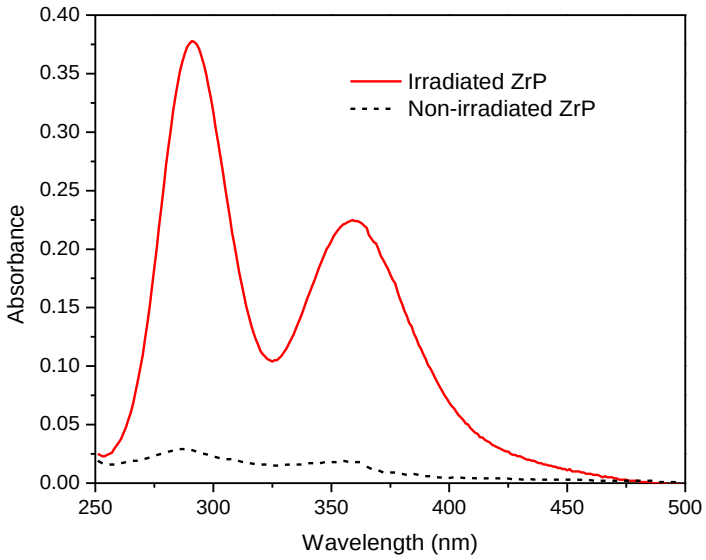

Figure 40. UV-Vis spectra measuring the amount of I_2 produced by irradiated and non-irradiated ZrP.

When the ZrP platelets (0.03 g/mL) were irradiated with ^{60}Co γ-rays in the presence of oxygen, peroxides, X-OOR, and X-OOH, where X stands for the ZrP platelets,

and R stands for a short alkyl group from tetrabutylammonium (TBA^+OH^-), were formed on the surface of the ZrP platelets, and also on the TBA chains, which were attracted to the surface of ZrP platelets by the amine groups. The pre-irradiated polymerization was previously used to make composite hydrogels [113], where the peroxide groups were proved using the iodometry method to be fabricated successfully using organic chemicals with ^{60}Co γ-rays under the O_2 ambience.

Poly *N*-isopropylacrylamide (PNIPAM) was fabricated by initiation of free radicals generated from the hemolysis of peroxide groups on ZrP surface and TBA groups, which attached to the ZrP surface. Each peroxide group was decomposed into two free radicals (XO· and HO·/RO·) by heating to 50°C under the N_2 atmosphere. The free radicals on the ZrP surface (XO·) would initiate the free radical polymerization of the *N*-isopropylacrylamide monomer to form PNIPAM grafted on the ZrP platelets. Similarly, the peroxide groups on the TBA group will decompose and initiate monomers to form PNIPAM.

Upon completion of the 24 h reaction, a white, viscous suspension product was formed. The product became a more transparent and less viscous when it was cooled to room temperature (20°C). The temperature-dependent behaviors indicated the success in the fabrication of PNIPAM polymers, which was further confirmed by the FTIR measurements. The as-prepared ZrP-PNIPAM suspensions were washed twice with deionized water, removing most of the free PNIPAM polymers produced by the small radicals (HO·/RO·) that were not on the ZrP surfaces. After washing, the ZrP-PNIPAM

became clearer, and was used as the mother suspension for all further experiments. The SEM image of ZrP-PNIPAM monolayers was shown in Figure 41.

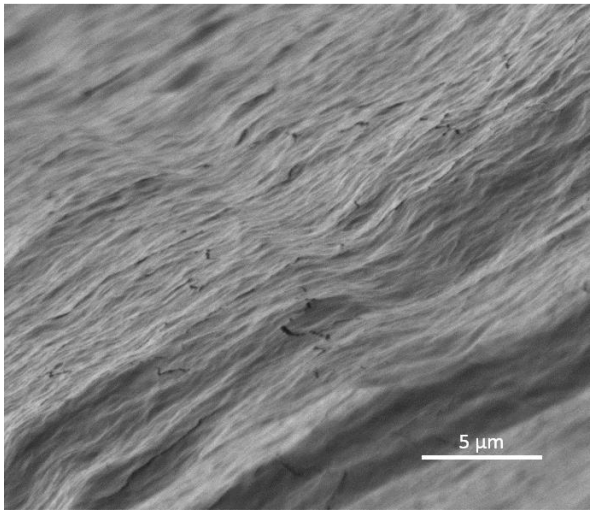

Figure 41. SEM image of ZrP-PNIPAM monolayers.

FTIR was performed using a Bruker Tensor 27 spectrometer in an attenuated total reflection (ATR) mode with a diamond ATR Prism Model Helios. The FTIR spectrum of ZrP and ZrP-PNIPAM platelet suspensions are shown in Figure 42. We observed the characteristic bands corresponding to the PNIPAM chains: the band for -C=O at 1624 cm^{-1} and the band for N-H at 1542 cm^{-1}, which did not appear for the ZrP sample, thus proving that the PNIPAM had been successfully grafted onto the ZrP surface using the pre-irradiated polymerization.

The sizes of the ZrP-PNIPAM platelets were measured by dynamic light scattering (DLS). According to our previous study, the TBA-exfoliated ZrP platelets have a fixed thickness of 2.68 nm. Grafting of PNIPAM polymer onto the ZrP surface changes the thickness of the ZrP-PNIPAM platelets. We assumed the lateral dimension of the ZrP was

not affected by the PNIPAM grafting. The thickness of the ZrP-PNIPAM platelets at various temperatures, therefore, can be calculated by measuring the diffusion of the platelets using DLS. The diameter of the ZrP platelets used for PNIPAM grafting was 891±270 nm. Figure 43 showed how the thickness of the ZrP-PNIPAM platelets varied with increasing temperature from 20°C to 60°C. The thickness decreased suddenly around 35°C, and then varied slightly from 35°C to 60°C. It is well known that PNIPAM has a phase transition around 30°C. In our case, ZrP-PNIPAM reached its smallest thickness above 35°C.

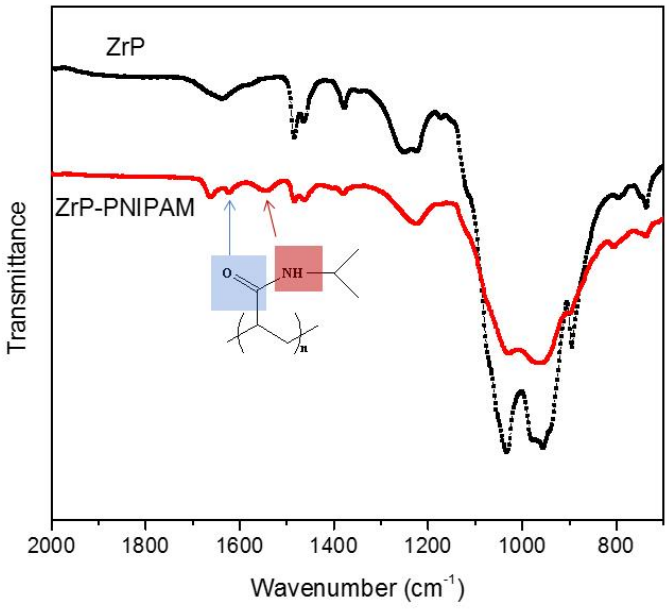

Figure 42. FTIR spectra of both TBA-exfoliated ZrP and ZrP-PNIPAM.

The sketches in Figure 43 illustrate how the ZrP-PNIPAM behaves before and after phase transition temperature; in this case, at 20°C and 50°C, respectively. The

PNIPAM chains on the surface of ZrP platelets were one-end-anchored free polymer chains at 20°C, and shrank to become smaller polymer coils at 50°C. As a result, the thickness of the ZrP-PNIPAM decreased at higher temperature. We simply fitted the thickness data with a smooth curve, and obtained the thickness of ZrP-PNIPAM at 50°C, which was 14.8±2.4 nm. The thickness at 50°C was about 23.4 times thinner than that at 20°C.

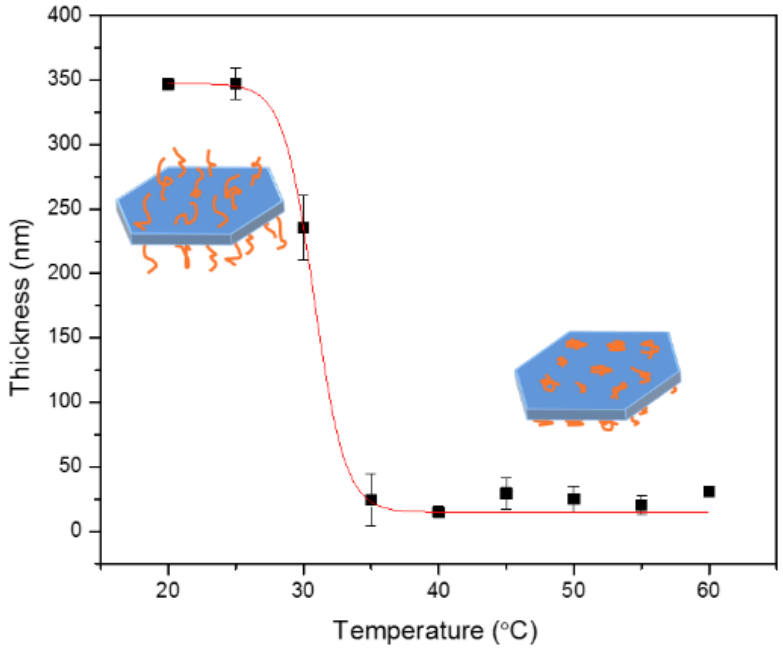

Figure 43. The dependence of ZrP-PNIPAM platelet thickness on temperature. The temperature-dependent behavior of ZrP-PNIPAM is shown schematically.

A set of ZrP-PNIPAM aqueous suspensions with different concentrations was used to establish the phase diagram at 20°C, and then at 50°C. As the concentration increased, there was an I-N phase transition. The nematic phase would settle to the bottom,

while the isotropic phase would move to the top under gravity, since it is less dense than the nematic phase. It took about two days for the samples in the coexistence to show a clear I-N interface at 20°C, and about five days at 50°C.

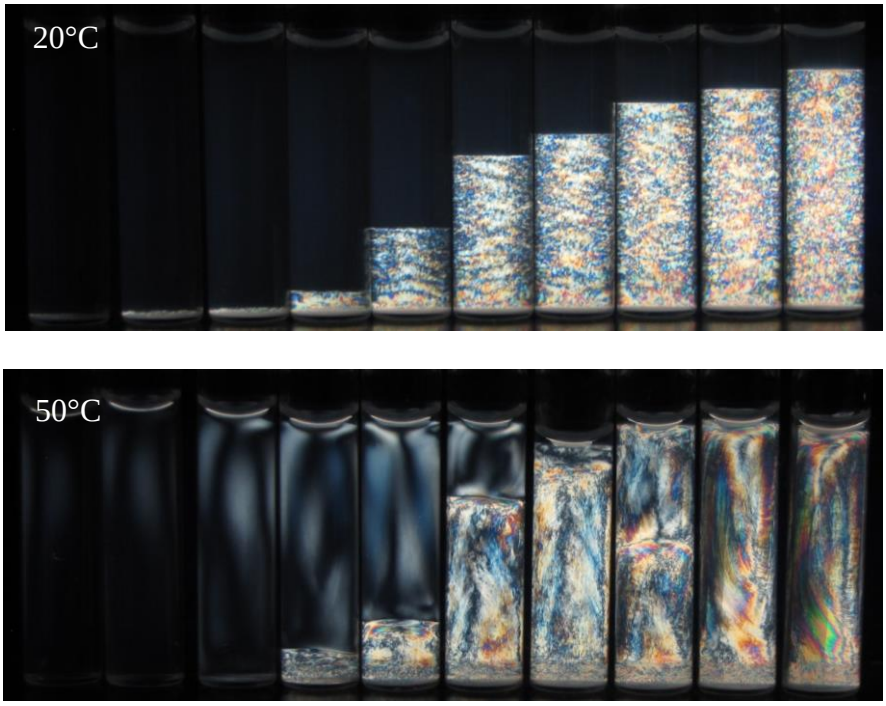

Figure 44. Cross-polarizing photographs of aqueous ZrP-PNIPAM suspensions at 20°C and 50°C. The ZrP-PNIPM concentration from left to right: 0.003, 0.0045, 0.006, 0.00675, 0.0075, 0.00825, 0.009, 0.00975, 0.0105 and 0.012 g/mL.

Figure 44 presents the cross-polarizing graphs of the ZrP-PNIPAM at 20°C and 50°C, respectively. Both sets of samples were kept at target temperature for 5 days. The colorful nematic phase textures at 50°C were different from that at 20°C. For the samples with concentrations of 0.00675, 0.0075, and 0.00825 (g/mL, particle to water), ZrP-PNIPAM showed sharp interfaces after 5 days at both temperatures. There were always sharp I-N interfaces for the ZrP-PNIPAM samples with higher concentrations, namely

0.009, 0.00975, 0.0105 and 0.012 g/mL at 20°C; however, at 50°C, higher concentration samples did not show interfaces, as they had a full nematic phase. The full nematic phase started to show up at a concentration of 0.00975 g/mL at 50°C. Nevertheless, even the highest concentration of ZrP-PNIPAM studied here did not have a full nematic phase at 20°C. The birefringent texture appearing in the isotropic phase at 50°C resulted from convection, which was induced by a temperature gradient since the photographs were taken at room temperature.

The I-N interface can move when isotropic and nematic phase separated due to density difference, also, the nematic phase can be compressed with time due to gravity. Cross-polarizing photographs were taken for the samples at a periodic sequence after mixing. Figure 45 presents the photographs for the 0.012 g/mL sample. The nematic fraction for this sample was obtained by normalizing the measured height of the nematic phase to the measured height of the total sample.

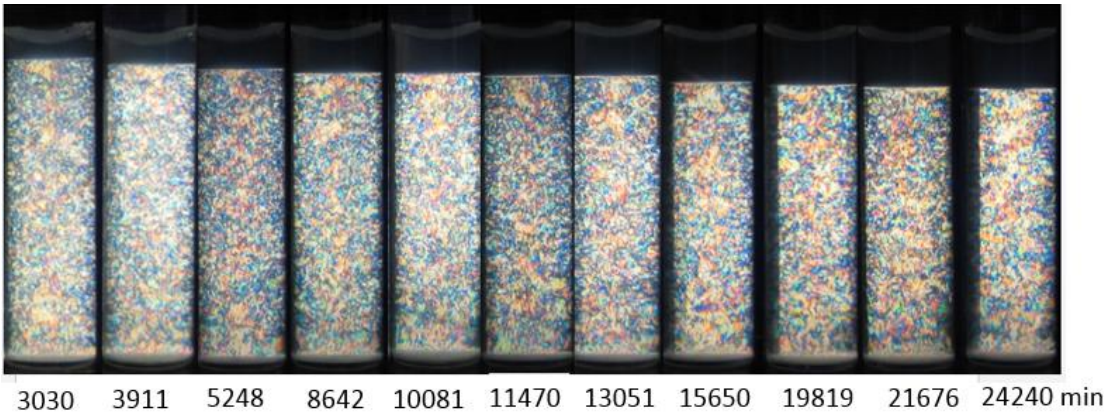

Figure 45. Cross-polarizing photographs of the 0.012 g/mL sample at 20°C at various times after mixing.

A plot of the nematic fraction versus time is shown in Figure 46. The equilibrium nematic fraction of the sample was obtained by extrapolating back to time zero. The intercept of the fitting line is 0.932±0.001, so we fixed 0.932 as the equilibrium nematic volume of this sample.

The first three data points in Figure 46 indicate sedimentation of the grains of nematics. The linear part, from 5,000 min to 12,500 min, indicates the compression of the nematics in gravity. The further decrease of the height of the nematics at time beyond 22,500 min is due to the phase transition from the nematics to another phase, which took place at the bottom part of the nematics. This procedure was used for all the samples at 20°C, 30°C and 50°C.

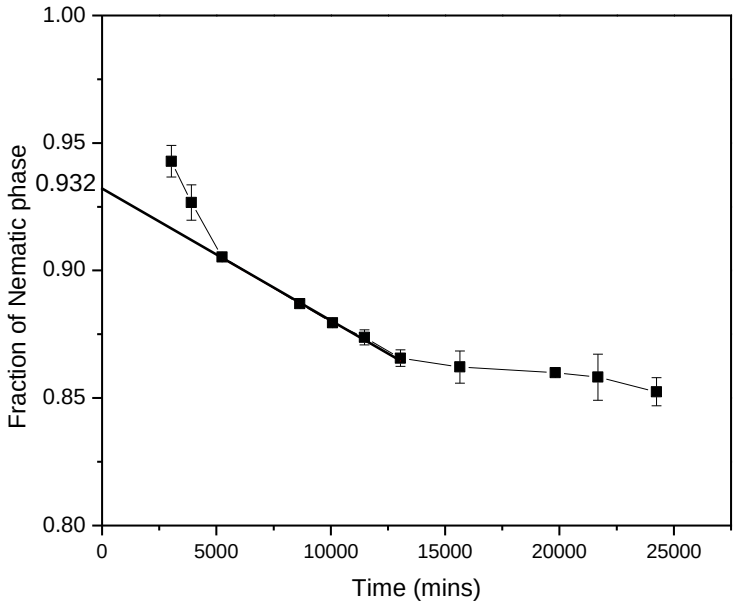

Figure 46. Determination of the equilibrium nematic fractions of the samples. The fraction of the nematic phase as a function of time. The solid line indicates the linear extrapolation to time zero after sample mixing.

A diagram of nematic fraction of ZrP-PNIPAM platelets versus the volume fraction at 20°C (circle) and 50°C (square) were plotted in Figure 47. The nematic fractions were obtained using the equilibrium height of the nematic phase normalized by the sample heights. Since the nematic phase would be compressed with time due to gravity, a time sequence of cross-polarizing photographs were taken for each single sample, then the equilibrium nematic fractions were obtained by extrapolating the time-dependent nematic fraction to time zero.

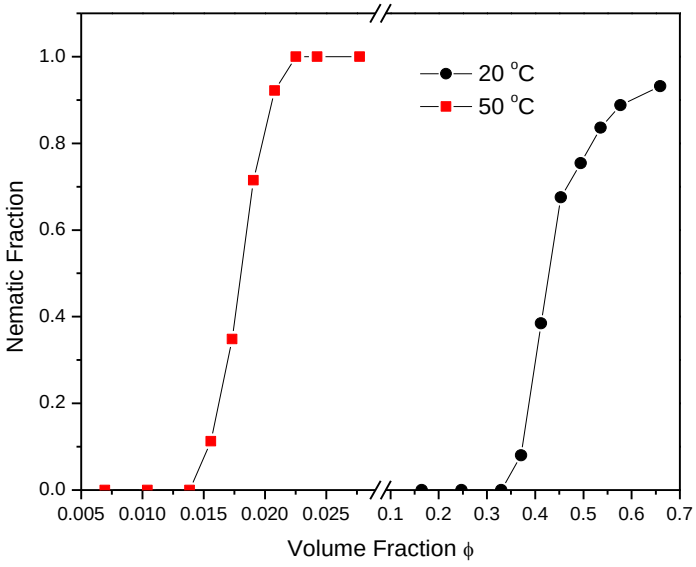

Figure 47. The fraction of nematic phase as a function of the platelets volume fraction ϕ.

The phase diagram of ZrP-PNIPAM at 50°C shifted to lower volume fraction compared with 20°C. Also, the width of the I-N transition at 50°C was narrower than that at 20°C. According to previous research about the effect of the polydispersity of hard particles on the I-N transition, the larger particles preferred to stay in the nematic phase

rather than in the isotropic phase, and the disparity in the number of larger to smaller particles in isotropic and nematic phase would increase as the polydispersity increased. In our case, the shrinking of PNIPAM on the ZrP surface at 50°C reduced the thickness of the ZrP-PNIPAM, hence their volume fraction. The reduction in thickness would decrease the aspect ratio, defined as the ratio of diameter over thickness, of the ZrP-PNIPAM since the diameter of the platelet did not change.

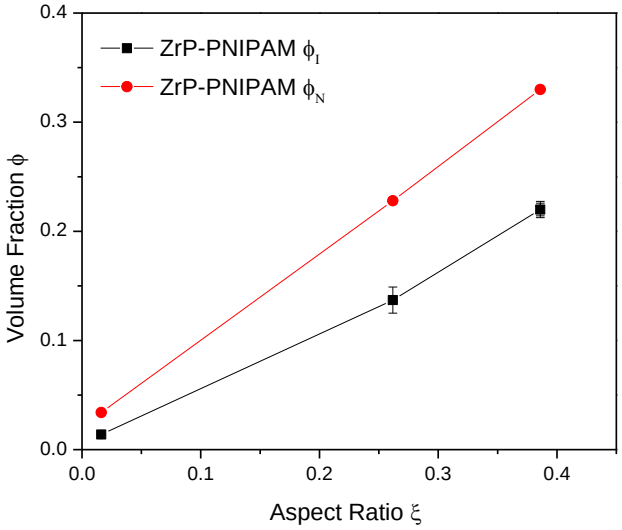

Figure 48. ϕ_I- ξ and ϕ_N - ξ of ZrP-PNIPAM.

When the temperature increased from 20°C to 50 °C, the aspect ratio (ξ) of ZrP-PNIPAM platelets decreased from 0.386 to 0.0162, the width of I-N transition became narrower, as shown in Figure 48, I-N transition width ($\Delta\phi_{I\text{-}N}$) [130] became smaller. It is obvious that the higher the polydispersity, the wider the I-N transition for ZrP. The aspect ratio of ZrP-PNIPAM at 20°C (ξ =0.386) and 30 °C (ξ =0.226) were much higher than that of ZrP (ξ=0.01, 0.002), so we were not comparing these two points to ZrP. At 50 °C,

ZrP-PNIPAM has an aspect ratio of 0.0162, which is closer that of ZrP, we found that the effect of polydispersity on ZrP-PNIPAM was consist with that on ZrP, as shown in Figure 48, the green star laid in between the two curves of ZrP.

As shown in the curves of Figure 49, the higher the polydispersity, the wider the I-N transiton. The black line indicated the ϕ_I-ξ of ZrP, the ϕ_N-ξ of ZrP were shown as the dash, dot and dash-dot line as the polydispersity increased. The dash-dot line was the one furthest away from the black line while the dot line was nearest one, which indicated that the distance between ϕ_I-ξ and ϕ_N-ξ line increased as the polydispersity increased for ZrP. By comparing the ϕ_I-ξ and ϕ_N-ξ curve of ZrP-PNIPAM with that of ZrP, we found that the distance between ϕ_I-ξ and ϕ_N-ξ curve of ZrP-PNIPAM was in a similar scale length to that for ZrP. Hence, we concluded that the polydispersity effect on ZrP-PNIPAM were similar to that on ZrP.

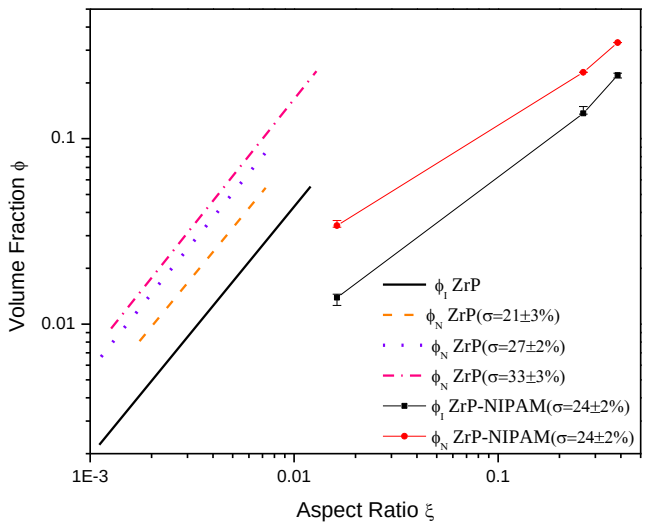

Figure 49. log-log plot of ϕ_I- ξ and ϕ_N – ξ for ZrP-PNIPAM, comparing with ZrP with various polydispersities[130].

To gain a better understanding on how the aspect ratio affects the ZrP-PNIPAM phase diagram, the I-N transition was also studied at 30°C. As shown in Figure 43, the thickness of the ZrP-PNIPAM platelets were 346±3 nm, 235±25 nm, and 14.8±5.9 nm at 20°C, 30°C, and 50°C, respectively. The aspect ratio for the sample at 20°C was 1.5 times and 23.4 times larger than that at 30°C and 50°C, respectively. Obviously, the aspect ratio can be easily adjusted by temperature. The advantage of the ZrP-PNIPAM platelets is that we were able to use just one set of samples to study the phase diagram of the I-N transition with various aspect ratios.

Figure 50 presents the log-log plot of the I-N transition volume fraction ϕ versus aspect ratio ξ of ZrP-PNIPAM platelets (red circles and solid fitting line). The ϕ-ξ curve for charged ZrP platelets[135] (black squares and solid fitting line), two curves of oblate hard spherocylinders (OHSC) free energy calculation[136] (green dotted lines), and Onsager-Parsons theory[137] curve (blue short dotted line) were also plotted for comparison. The ϕ-ξ of ZrP-PNIPAM can be fitted into a linear line, which had a similar tendency as the ϕ-ξ line of ZrP system [135], OHSC free energy calculation, Onsager-Parsons theory, and the I-N transition of cut spheres [130].

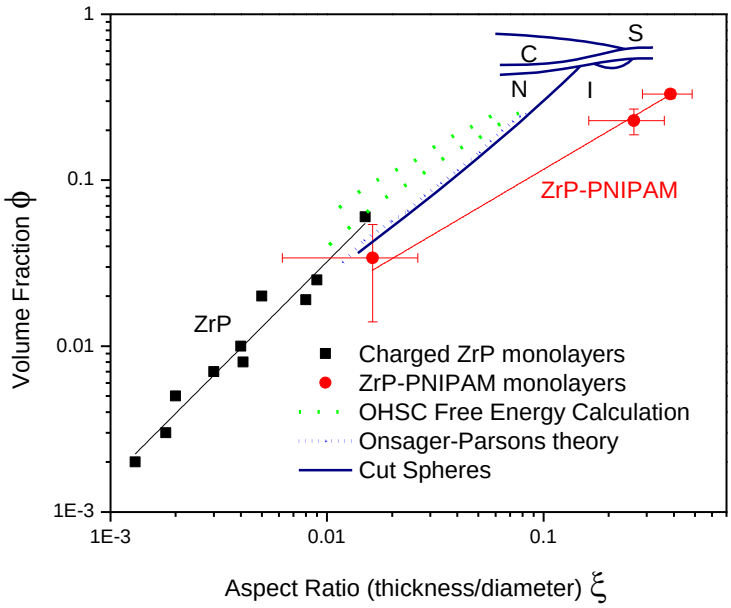

Figure 50. The dependence of the I-N transition on aspect ratio.

The slopes of the OHSC free energy calculation curves are 3.81 ± 0.11 and 3.12 ± 0.78, respectively, while Onsager-Parsons theory has a similar slope of 3.15 ± 0.05. The slope of charged ZrP platelets, 3.95 ± 0.36, is close to the theoretical calculations, but the data is for a smaller aspect ratio range. The curves of charged ZrP and the Onsager-Parsons theory are consistent with each other, and might be two different parts of the same continuous curve. The slope of I-N transition curve for cut spheres[130] is 3.27 ± 0.06, which is similar to the charged ZrP samples. The slope for ZrP-PNIPAM, 0.80 ± 0.01, however, is significantly smaller than any of mentioned slopes. In addition, the phase diagram of cut spheres[130] indicates that liquid crystals exist only when ξ is smaller than 0.25, as shown in Figure 50 (solid navy lines). For ξ = 0.1, there were isotropic (I), nematic (N), columnar (C), and solid (S) phases; for ξ = 0.2, there were isotropic, columnar, and solid phases; for

ξ = 0.3, there were only isotropic and solid phases. As observed here for the ZrP-PNIPAM soft platelets, the nematic phase still exists for aspect ratios as high as 0.33. Hence, by modifying with PNIPAM, charged ZrP platelets became soft ZrP-PNIPAM platelets, and the I-N transition curve shifts towards higher aspect ratio with a much less steep slope.

5.4 Conclusions

In summary, thermo-sensitive discotic liquid crystals were fabricated using the pre-irradiated polymerization of temperature-sensitive poly(*N*-isopropylacrylamide) (PNIPAM) on the surface of ZrP platelets. To the best of our knowledge, this is the first time that temperature-sensitive discotic liquid crystals were obtained. By changing environmental temperature, the thickness of the ZrP-PNIPAM was changed; the aspect ratio of ZrP-PNIPAM was about 23.4 times smaller at 50°C than at 20°C. As a result, the phase diagram of ZrP-PNIPAM platelets was shifted to lower volume fraction as temperature increased. The dependence of the I-N transition on the aspect ratio agrees with our previously result on charged ZrP platelets, as well as the OHSC free energy calculation and Onsager-Parsons theory. Moreover, we were able to study the I-N phase diagram in volume fraction versus aspect ratio by adjusting the temperature, using only one set of ZrP-PNIPAM samples. The nematic phase can exist at a higher aspect ratio for the soft ZrP-PNIPAM disks than for the hard cut spheres.

CHAPTER VI

SUMMARY AND FUTURE WORK

6.1 Encapsulation using amphiphilic ZrP-C18 nanoplates

6.1.1 Summary

In Chapter II and Chapter III, amphiphilic ZrP-C18 nanoplates have been used as Pickering emulsifiers for encapsulation. Two different kinds of material have been successfully encapsulated. One was cancer drugs, the other was PCMs. The cancer drugs were encapsulated into uniformly and submicron drug nanoparticles which were promising for delivery. And the PCMs were encapsulated into capsules in submicron meters NEPCMs, using polymers as hard shells. NEPCMs would be useful in energy storage.

The stability of Pickering emulsions contribute to both encapsulations of drugs and PCMs. The stability of emulsions prepared prevent the coalescence of emulsions which would form larger emulsions and hence resulted in higher polydispersity. Thanks to the stability of drug (EA)/water emulsions, we were able to obtain drug particles that were uniform and small. Thanks to the stability of PCMs/water emulsions as well as the double emulsions later in the second step emulsification, we were able to obtain submicron NEPCMs.

In additional to the stability of Pickering emulsion that contribute to the size of drug nanoparticles and NEPCMs, there were still some other advantages by using ZrP-

C18 as stabilizer and Pickering encapsulation to prepare drug nanoparticles and NEPCMs. For the drug nanoparticles, surfactant–free was really important because the drug nanoparticles would be used in human body. And most of molecular surfactant residual would be toxic that need to be carefully removed after drug nanoparticles were fabricated.

As to the NEPCMs, two merits were presented: low energy input requirement and simple emulsification procedure. Low energy input was required for the two-step Pickering emulsification procedure. This would be important regarding to energy saving. Moreover, the procedure was simply which would enable the production of NEPCMs to be easily scaled-up.

6.1.2 Future work

The study of amphiphilic ZrP-C18 nanoplates as Pickering emulsifiers will be continued. For a better understand of ZrP-C18 nanoplates behavior as emulsifiers, we will compare ZrP-C18 nanoplates to molecular surfactants. Other materials will be encapsulated using ZrP-C18 nanoplates as well. For example, molecular hydrophobic liquid crystal materials will be encapsulated into liquid crystal droplets for defect studying.

What's more, only O/W emulsions have been investigated so far. In the future, ZrP nanoplates will be further modified so that it can be helpful in stabilization of W/O emulsions.

6.1.2.1 Compare ZrP-C18 Pickering emulsifier to molecular surfactant SDS

ZrP-C18 nanoplates were used alone or with SDS to stabilized PS particles. Herein, 900 μL DI water, 100 μL styrene with 0.0016g AIBN was added into a 2-mL glass

vial, and then hand shaking for 30 seconds to emulsify the O/W emulsions. The whole emulsion suspensions were put into 65 °C oven for 4 hours, allowing fully polymerization of styrene monomers.

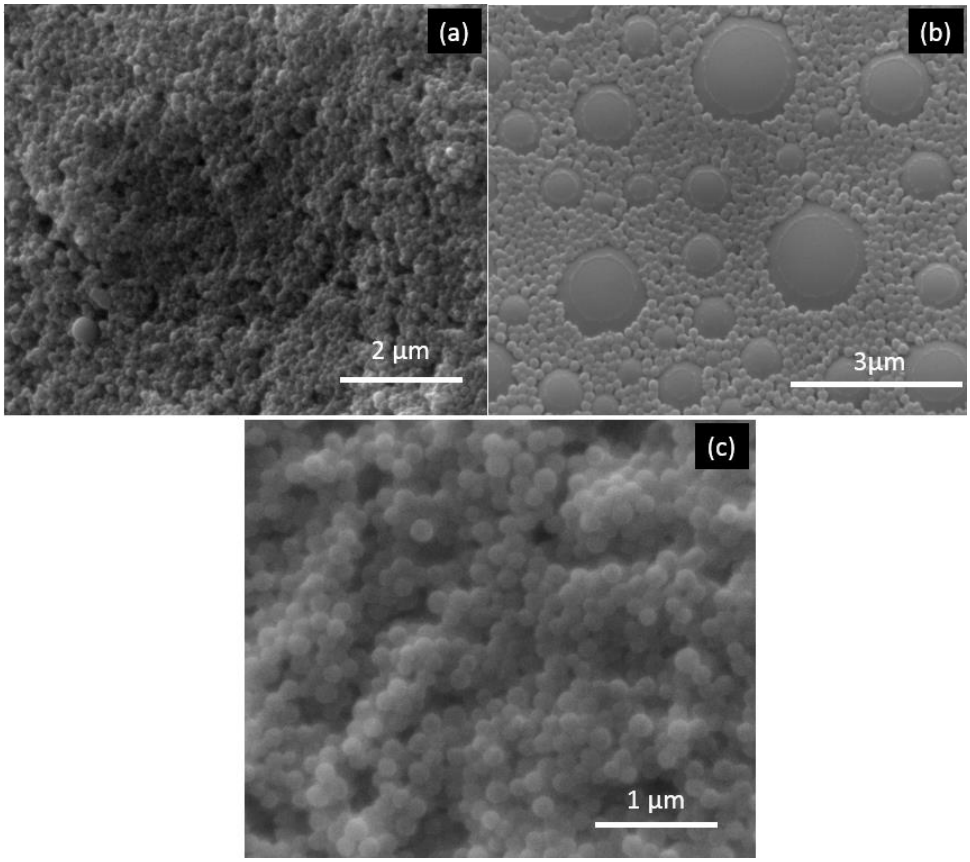

Figure 51. SEM images of PS particle stabilized by (a) 0.1% wt ZrP-C18, (b) 0.1% wt SDS and (c) 0.05% wt ZrP-C18 and 0.05 %wt SDS.

As indicated in Figure 51, by using ZrP-C18 nanoplate, SDS or their mixture to stabilize PS particles. It is clear that most of PS particle stabilized by SDS were relatively small but we still had some PS particles that were very large (Figure 51b). The PS stabilized by ZrP-C18 didn't have huge particles, while the polydispersity of PS particles

stabilized by ZrP-C18 alone was also high (Figure 51a). However, the PS particle stabilized by the mixture had the lowest polydispersity as well as smallest size (Figure 51c).

Table 1 shows the size of PS particles stabilized by different concentrations of ZrP-C18, SDS or ZrP-C18 nanoplates plus SDS measured by DLS. The results were mostly consistent with the SEM results, at the same concentrations, ZrP-C18 nanoplates produced larger PS particles compared to SDS. And the mixtures produced most uniform and smallest PS particles. It should be pointed out that the number of big PS particles produced by SDS didn't indicated well by the DLS results.

Table 1. The size of PS stabilized by different concentrations of ZrP-C18, SDS or ZrP-C18 and SDS mixture.

Concentration (%)	ZrP-C18(nm)	SDS(nm)	ZrP-C18+SDS(nm)
0.1 %wt	340±103	211±81	199±37
0.2%wt	246±54	208±79	193±43
0.4%wt	209±46	162±71	197±48
0.8%wt	206±85	117±53	138±41
1%wt	190±55	125±66	133±27

This example also proved that Pickering emulsifiers ZrP-C18 nanoplates prevent the coalescing of emulsions. By using the same amount of ZrP-C18 nanoplates and SDS, initially, the emulsions stabilized by ZrP-C18 nanoplates were larger than those by SDS, as indicated in Figure 51 and Table 1. However, the emulsions stabilized by SDS were coalesced into larger ones which resulted in the extra-large PS particles. For further study, efforts may focus on investigation of emulsions coalescing to better understand the advantage of the Pickering emulsifiers.

6.1.2.2 Liquid crystal encapsulation

Liquid crystals (LCs) exhibit various topological defects: point defects, line defects, loops, disclinations and dislocations. Liquid crystal defects extend not over distances of several atoms as in solid state physics, but rather tens of micrometers. The larger defects together with birefringence property makes LCs comparably easy to be studied by polarizing optical microscopy (POM) and digital image acquisition.

It is widely appreciated that the supramolecular ordering of LCs can be impacted by confinement, and it is generally accepted that size dependent ordering of LCs reflects a subtle competition between bulk and interfacial physicochemical factors. Plenty of approaches have been applied for adjusting LC droplet size (in a relevant size range) with rigorous control over interfacial chemistry, temperature, and other key parameters of the system.

Herein we are using Pickering emulsification to fabricate monodisperse droplets of the nematic LC 4’-pentyl-4-cyanobiphenyl (5CB) which is a typical nematic liquid crystal. 5CB droplets were fabricated via Pickering emulsification. ZrP-C18 nanoplates were suspended in DI water as water phase, and LC material 5CB to be used as oil phase. As shown in Figure 52 , by gentle manually shaking, 5CB-in-water emulsions could be easily fabricated using using ZrP-C18 nanoplates. The droplets were relatively uniform, with a size around 2μm, and typical nametic defect were obtained under POM (Figure 53).

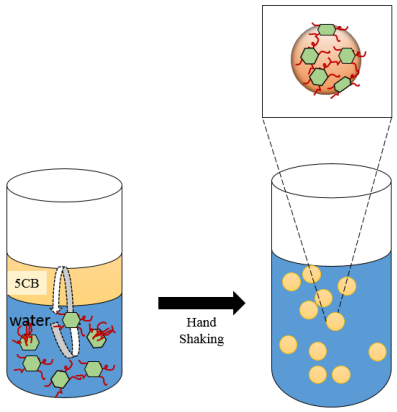

Figure 52. Schematic of 5CB droplets fabricated via Pickering emulsification.

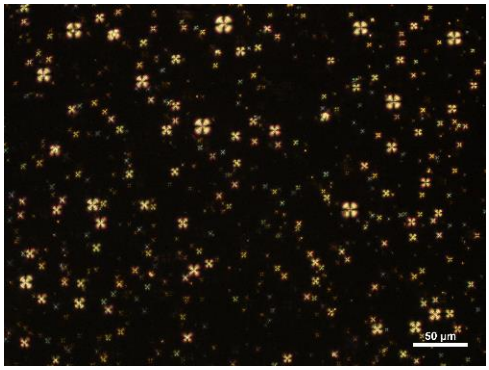

Figure 53. 5CB droplets under POM.

In the future, by varying the solvent, the surface modified ZrP-C18 nanoplate concentration, the mixing method and the 5CB to water ratio, we will be able to fabricate various size 5CB droplets.

6.2 Thermosensitive ZrP monolayers

6.2.1 Summary

In Chapter IV, layered ZrP disks were first modified with PNIPAM using a pre-irradiated polymerization[138] technique, the PNIPAM was grafting onto ZrP disks surface

by covalent bonding. ZrP-PNIPAM was then exfoliated into monolayers using TBA^+OH^-. ZrP-PNIPAM monolayers obtained after exfoliation were then used to stabilize O/W emulsions and to fabricate polystyrene (PS) particles as Pickering emulsifiers. The controlled release behavior was studied using a model material 5CB. 5CB was hydrophobic molecular liquid crystal, which was emulsified by ZrP-PNIPAM monolayers to form O/W emulsions droplets. By controlling temperature, the release of the droplets was observed under a crossed polarized microscope. This study marks the first time that asymmetric thermosensitive ZrP-PNIPAM monolayers were applied in the controlled release areas as a Pickering emulsifier.

In Chapter V, exfoliated ZrP monolayers were modified with PNIPAM using the same method. The ZrP-PNIPAM monolayers were excellent materials to study the I-N phase transition of discotic liquid crystal since we can control the aspect ratio of the ZrP-PNIPAM monolayers by varying temperature. The results showed that the I-N transition of ZrP-PNIPAM was in the same range as previous study from both experimental results and theoretical calculations.

6.2.2 Future work

(1) ZrP-PNIPAM monolayers will be uses to stable drug materials that will be released by arising temperature;

(2) ZrP monolayers will be modified with PNIAPM after removing the exfoliated agent. In this case, it would be interesting to study the thermosensitive liquid crystal, where all the PNIPAM are covalently grafted onto ZrP monolayers. Or, instead of

individual ZrP-PNIPAM monolayers, we may able to obtain thermosensitive ZrP-PNIPAM gels with well-defined 3D structures.

6.3 Further development of amphiphilic nanoplates emulsifiers

6.3.1 Glucose modification of ZrP-C18

So far, we haven't show the performance of ZrP-C18 after being modified with hydrophilic polymers. The OH and TBA^+ groups on ZrP enable the hydrophilicity. It would interesting to see how the ZrP-C18 Pickering emulsifiers would be improved after being grafted with some hydrophilic groups.

As shown in Figure 54, ZrP-C18 nanoplates were further modified with glucose after exfoliation. Tin chloride ($SnCl_4$) was used to remove the TBA^+ groups on the ZrP surface. And then D-glucose 6-phosphate di sodium salt hydrate ($C_6H_{11}O_6$-$Na_2PO_3 \cdot xH_2O$) was added to graft glucose onto the ZrP-C18 by ion exchange.

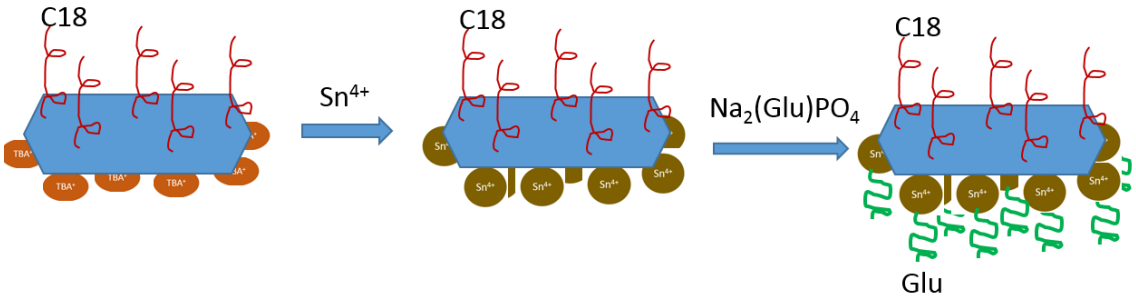

Figure 54. Schematic of functionalization of ZrP-C18 nanoplates with glucose to be Glu-Sn-ZrP-C18 nanoplates.

Glu-Sn-ZrP-C18 nanoplates can be used to stabilize W/O emulsions as well. As indicated in Figure 55, dodecane in water emulsions was stabilized using Glu-Sn-ZrP-C18

nanoplates at an oil to water ratio of 1:9, and the concentration of Glu-Sn-ZrP-C18 was 0.1 %wt. The size of the emulsions was in micrometers and they were relatively uniform.

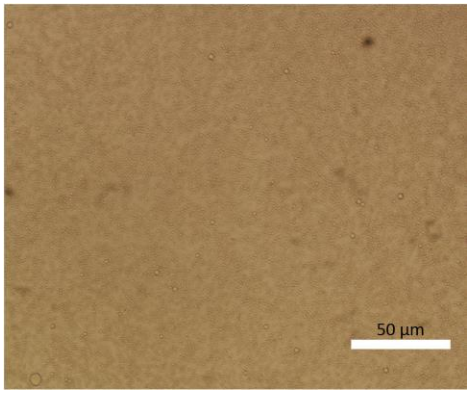

Figure 55. O/W emulsions stabilized by Glu-Sn-ZrP-C18 nanoplates.

The air-water interface surface tention of the Glu-Sn-ZrP-C18 nanoplates suspensions at various concentration were measured using Wilhelmy plate. As indicated in Figure 56, we can easily tell that after surface modification of glucose. The surface tension of the suspensions was increased compared to the ZrP-C18 nanoplate suspensions at the same concentrations.

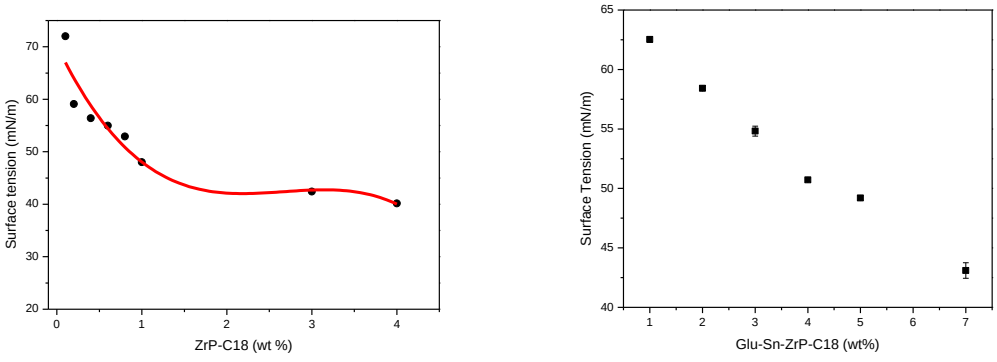

Figure 56. The surface tension of Glu-Sn-ZrP-C18 nanoplates (left) compared to ZrP-C18 nanoplates (right).

One advantage of the Glu-Sn-ZrP-C18 nanoplates was that the viscosity can be adjusted easily. As shown in Figure 57, the viscosity of Glu-Sn-ZrP-C18 nanoplates suspensions were measured using Paar Physica MCR300 Rheometer. As the suspension concentration increased, the viscosity was decresed as shear rate increased. The higher the suspension concentration, the higher the viscosity. We concluded that it was effective to increase the viscosity of the suspension by grafting glucose onto the ZrP-C18 surface by replacing TBA groups.

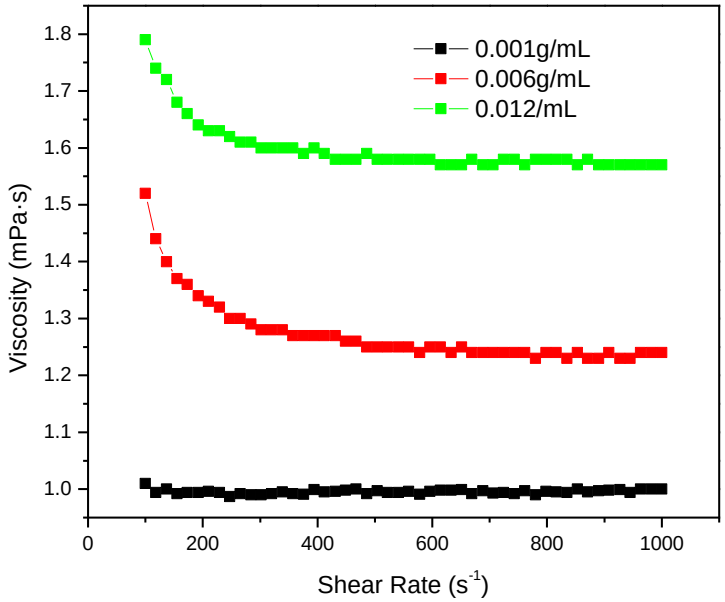

Figure 57. Rheology of Glu-Sn-Zr-C18 nanoplates suspensions at different concentrations.

In the future, depend on the requirement, other hydrophilic materials such as polyethylene glycol (PEG), can also be used to modify the ZrP-C18 nanoplates. Hence the

viscosity can easily be adjusted by grafting high molecular weight hydrophilic polymers onto the ZrP-C18 nanoplates.

6.3.2 Water in oil Pickering emulsions

As discussed before, for Pickering stabilizers, one key factor is the contact angle (θ) between the particle and the oil/water interface which was indicated by the hydrophobicity of the particles. The higher the hydrophobicity, the more possibility that W/O emulsions would be fabricated. The ZrP-C18 we prepared so far were more like to prepare O/W emulsions. More hydrophobic Pickering emulsifiers are needed in terms of making W/O emulsions.

In order to fabricate more hydrophobic Pickering emulsifiers. The ZrP disks prepared by reflux method was firstly exfoliated using TBA^+OH^- as we did before. And extra diluted HCl (pH = 2) solution was added into the suspension to recreate the OH groups on the exfoliated ZrP nanoplates. The suspension became gel-like material right after the addition of HCl. The ZrP nanoplate gel was washed with DI water three times to remove extra HCl and TBA^+ groups. Secondly, the ZrP nanoplate gel was freezing dried to become a puff-like material. Thirdly, a surface modification was carried onto this puff-like material using ODI in toluene. The surface modification procedure was exactly the same with that for layered ZrP as described in 2.2.2.

The result material was modified with C18 both sides to become C18-ZrP-C18 nanoplates. C18-ZrP-C18 nanoplates been employed to prepared W/O emulsions, as shown in Figure 58, water in dodecane emulsions were fabricated using C18-ZrP-C18

nanoplates with an oil/water ratio at 9:1. The emulsions were investigated under optical microscope as well (Figure 59).

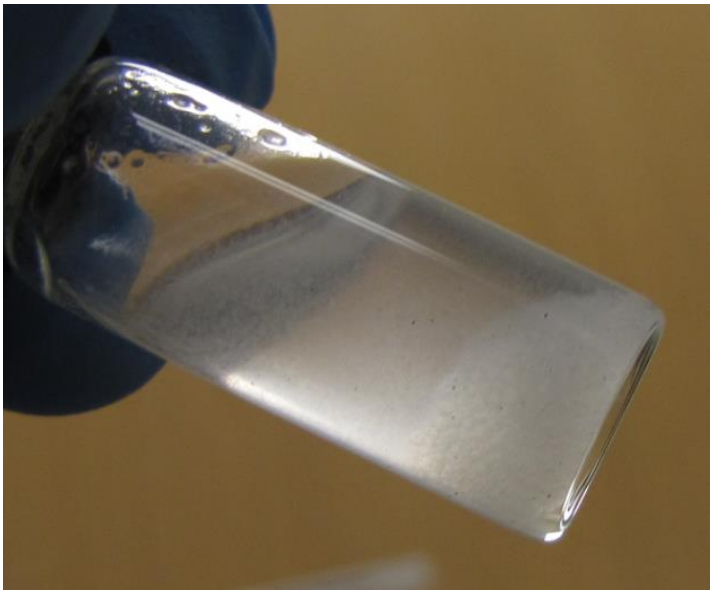

Figure 58. W/O emulsions stabilized by C18-ZrP-C18 nanoplates.

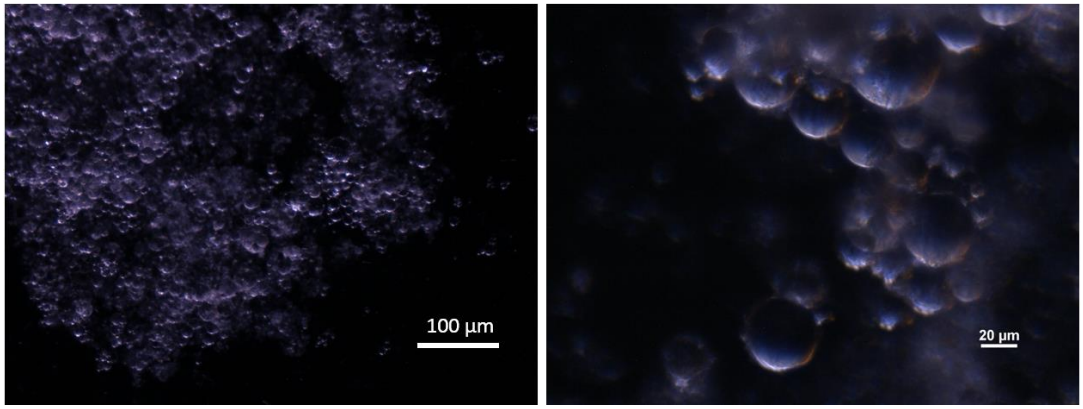

Figure 59. W/O emulsions by C18-ZrP-C18 nanoplates under optical microscope.

In the future, detailed properties of the C18-ZrP-C18 nanoplates will be studied, for example, the surface tension of the suspensions. The encapsulations application will

also be greatly widen by using the emulsifier to stabilize W/O emulsions. Hydrophilic materials will be encapsulated. For example, the inorganic PCMs salt hydrates can be encapsulated. What's more, micro/nano hydrogels can be also obtained for the drug deliveries.

REFERENCES

1. V. Nicolosi, M. Chhowalla, M. G. Kanatzidis, M. S. Strano and J. N. Coleman, *Science*, 2013, **340**, 1226419 (1-20).
2. S. Jeong, D. Yoo, J.-t. Jang, M. Kim and J. Cheon, *Journal of the American Chemical Society*, 2012, **134**, 18233-18236.
3. K. S. Novoselov, D. Jiang, F. Schedin, T. J. Booth, V. V. Khotkevich, S. V. Morozov and A. K. Geim, *Proceedings of the National Academy of Sciences of the United States of America*, 2005, **102**, 10451-10453.
4. J.-M. Li, *Nano Letters*, 2008, **8**, 1382-1385.
5. J.-M. Li, *Applied Physics A*, 2010, **99**, 229-235.
6. M. Shuai, A. F. Mejia, Y.-W. Chang and Z. Cheng, *CrystEngComm*, 2013, **15**, 1970-1977.
7. J. M. Troup and A. Clearfield, *Inorganic Chemistry*, 1977, **16**, 3311-3314.
8. Y. Zhou, R. Huang, F. Ding, A. D. Brittain, J. Liu, M. Zhang, M. Xiao, Y. Meng and L. Sun, *ACS Applied Materials & Interfaces*, 2014, **6**, 7417-7425.
9. D. Castellanos, A. Lewandowski, A. Diaz, A. F. Mejia, V. Carreto, C. Mashuga, A. S. Rangwala, Z. Cheng and M. S. Mannan, *Industrial & Engineering Chemistry Research*, 2014, **53**, 11527-11537.
10. J. Alongi and A. Frache, *Polym Degrad Stabil*, 2010, **95**, 1928-1933.
11. F. Bauer and M. Willert-Porada, *Fuel Cells*, 2006, **6**, 261-269.

12. C. B. Amphlett, L. A. Mcdonald and M. J. Redman, *Chem Ind-London*, 1956, **44**,1314-1315.

13. P. Armento, M. Casciola, M. Pica, F. Marmottini, R. Palombari and F. Ziarelli, *Solid State Ionics*, 2004, **166**, 19-25.

14. A. Diaz, V. Saxena, J. Gonzalez, A. David, B. Casanas, C. Carpenter, J. D. Batteas, J. L. Colon, A. Clearfield and M. D. Hussain, *Chem Commun*, 2012, **48**, 1754-1756.

15. M. Pica, A. Donnadio, V. Bianchi, S. Fop and M. Casciola, *Carbohyd Polym*, 2013, **97**, 210-216.

16. M. Pica, A. Donnadio and M. Casciola, *Starch-Starke*, 2012, **64**, 237-245.

17. U. Costantino, F. Fringuelli, M. Orru, M. Nocchetti, O. Piermatti and F. Pizzo, *Eur J Org Chem*, 2009, **8**, 1214-1220.

18. X. He, H. Xiao, H. Choi, A. Díaz, B. Mosby, A. Clearfield and H. Liang, *Colloids and Surfaces A: Physicochemical and Engineering Aspects*, 2014, **452**, 32-38.

19. G. G. Aloisi, U. Costantino, F. Elisei, M. Nocchetti and C. Sulli, *Mol Cryst Liq Crys A*, 1998, **311**, 245-250.

20. F. Xia, H. Yong, X. Han and D. Sun, *Nanoscale Research Letters*, 2016, **11**, 348.

21. W. J. Boo, L. Sun, J. Liu, A. Clearfield and H.-J. Sue, *The Journal of Physical Chemistry C*, 2007, **111**, 10377-10381.

22. M. Wong, R. Ishige, T. Hoshino, S. Hawkins, P. Li, A. Takahara and H.-J. Sue, *Chemistry of Materials*, 2014, **26**, 1528-1537.

23. P. He, A. F. Mejia, Z. Cheng, D. Sun, H.-J. Sue, D. S. Dinair and M. Marquez, *Physical Review E*, 2010, **81**, 026310.

24. X. Wang, D. Zhao, A. Diaz, I. B. Nava Medina, H. Wang and Z. Cheng, *Soft Matter*, 2014, **10**, 7692-7695.

25. A. F. Mejia, R. Ng, P. Nguyen, M. Shuai, H. Y. Acosta, M. S. Mannan and Z. D. Cheng, *Soft Matter*, 2013, **9**, 10257-10264.

26. A. F. Mejia, A. Diaz, S. Pullela, Y.-W. Chang, M. Simonetty, C. Carpenter, J. D. Batteas, M. S. Mannan, A. Clearfield and Z. Cheng, *Soft Matter*, 2012, **8**, 10245-10253.

27. X. Wang, L. Zhang, Y.-H. Yu, L. Jia, M. Sam Mannan, Y. Chen and Z. Cheng, *Scientific Reports*, 2015, **5**, 13357.

28. J. S. Guevara, A. F. Mejia, M. Shuai, Y. W. Chang, M. S. Mannan and Z. D. Cheng, *Soft Matter*, 2013, **9**, 1327-1336.

29. R. L. Jones, N. C. Pearsall and J. D. Batteas, *The Journal of Physical Chemistry C*, 2009, **113**, 4507-4514.

30. B. M. Mosby, A. Diaz and A. Clearfield, *Dalton Transactions*, 2014, **43**, 10328-10339.

31. B. M. Mosby, A. Díaz, V. Bakhmutov and A. Clearfield, *ACS Applied Materials & Interfaces*, 2014, **6**, 585-592.

32. F. Bellezza, A. Cipiciani, U. Costantino and M. E. Negozio, *Langmuir*, 2002, **18**, 8737-8742.

33. C. Y. Ortiz-avila and A. Clearfield, *Inorganic Chemistry*, 1985, **24**, 1773-1778.

34. A. Díaz, B. M. Mosby, V. I. Bakhmutov, A. A. Martí, J. D. Batteas and A. Clearfield, *Chemistry of Materials*, 2013, **25**, 723-728.

35. B. M. Mosby, M. Goloby, A. Díaz, V. Bakhmutov and A. Clearfield, *Langmuir*, 2014, **30**, 2513-2521.

36. M. Casciola, D. Capitani, A. Donnadio, G. Munari and M. Pica, *Inorganic Chemistry*, 2010, **49**, 3329-3336.

37. Abrahan Clearfield and C. Y. Ortiz-Avila, *polyether and polyamine derivatives of layered zirconium phosphates a supramolecules*, 1992.

38. X.-Q. Liu, D.-Y. Wang, X.-L. Wang, L. Chen and Y.-Z. Wang, *Polym Degrad Stabil*, 2013, **98**, 1731-1737.

39. Q. Zhang, H. Liu, X. Li, R. Xu, J. Zhong, R. Y. Chen and X. H. Gu, *Polym. Eng. Sci.*, 2016, **56**, 622-628.

40. D.-Y. Wang, X.-Q. Liu, J.-S. Wang, Y.-Z. Wang, A. A. Stec and T. R. Hull, *Polym Degrad Stabil*, 2009, **94**, 544-549.

41. H. J. Sue, K. T. Gam, N. Bestaoui, N. Spurr and A. Clearfield, *Chemistry of Materials*, 2004, **16**, 242-249.

42. R. Zhang, Y. Hu, B. Li, Z. Chen and W. Fan, *Journal of Materials Science*, 2007, **42**, 5641-5646.

43. K. L. Liu, H. C. Lee, B. Y. Wang, S. J. Lue, C. Y. Lu, L. D. Tsai, J. Fang and C. Y. Chao, *J. Membr. Sci.*, 2015, **495**, 110-120.

44. F. Carn, A. Derre, W. Neri, O. Babot, H. Deleuze and R. Backov, *New Journal of Chemistry*, 2005, **29**, 1346-1350.

45. M. Wong, R. Ishige, K. L. White, P. Li, D. Kim, R. Krishnamoorti, R. Gunther, T. Higuchi, H. Jinnai, A. Takahara, R. Nishimura and H.-J. Sue, *Nat Commun*, 2014, **5**.

46. Y. Zhou, J. Liu, M. Xiao, Y. Meng and L. Sun, *ACS Applied Materials & Interfaces*, 2016, **8**, 5547-5555.

47. A. Walther and A. H. E. Muller, *Soft Matter*, 2008, **4**, 663-668.

48. F. M. Menger and C. A. Littau, *Journal of the American Chemical Society*, 1993, **115**, 10083-10090.

49. P. G. Degennes, *Angew Chem Int Edit*, 1992, **31**, 842-845.

50. F. M. Menger and J. S. Keiper, *Angewandte Chemie-International Edition*, 2000, **39**, 1907-1920.

51. E. Vignati, R. Piazza and T. P. Lockhart, *Langmuir*, 2003, **19**, 6650-6656.

52. S. Levine, B. D. Bowen and S. J. Partridge, *Colloids and Surfaces*, 1989, **38**, 325-343.

53. S. Tsuji and H. Kawaguchi, *Langmuir*, 2008, **24**, 3300-3305.

54. F. Bellezza, A. Cipiciani, U. Costantino and S. Nicolis, *Langmuir*, 2004, **20**, 5019-5025.

55. F. Bellezza, A. Cipiciani and U. Costantino, *Journal of Molecular Catalysis B: Enzymatic*, 2003, **26**, 47-56.

56. S. Xu, J. C. Whitin, T. T.-S. Yu, H. Zhou, D. Sun, H.-J. Sue, H. Zou, H. J. Cohen and R. N. Zare, *Analytical Chemistry*, 2008, **80**, 5542-5549.

57. K. Avgoustakis, A. Beletsi, Z. Panagi, P. Klepetsanis, A. G. Karydas and D. S. Ithakissios, *Journal of Controlled Release*, 2002, **79**, 123-135.

58. J. Fang, H. Nakamura and H. Maeda, *Advanced Drug Delivery Reviews*, 2011, **63**, 136-151.

59. A. zur Mühlen, C. Schwarz and W. Mehnert, *European Journal of Pharmaceutics and Biopharmaceutics*, 1998, **45**, 149-155.

60. S. Hariharan, V. Bhardwaj, I. Bala, J. Sitterberg, U. Bakowsky and M. N. V. Ravi Kumar, *Pharmaceutical Research*, 2006, **23**, 184-195.

61. T. Musumeci, C. A. Ventura, I. Giannone, B. Ruozi, L. Montenegro, R. Pignatello and G. Puglisi, *International Journal of Pharmaceutics*, 2006, **325**, 172-179.

62. D. Cunha, M. Ben Yahia, S. Hall, S. R. Miller, H. Chevreau, E. Elkaim, G. Maurin, P. Horcajada and C. Serre, *Chemistry of Materials*, 2013, **25**, 2767-2776.

63. H. Maeda, J. Wu, T. Sawa, Y. Matsumura and K. Hori, *Journal of Controlled Release*, 2000, **65**, 271-284.

64. D. K. Sahana, G. Mittal, V. Bhardwaj and M. Kumar, *J. Pharm. Sci.*, 2008, **97**, 1530-1542.

65. M. Seiler, M. Haneke, H. Marckmann, S. Pilz, M. Irfan, S. Klee-Laquai, G. Hills, M. Farwick, P. Lersch and A. Kobus, Google Patents, 2010.

66. A. Lamprecht, U. Schafer and C. M. Lehr, *Pharmaceutical Research*, 2001, **18**, 788-793.

67. J. Frelichowska, M.-A. Bolzinger, J.-P. Valour, H. Mouaziz, J. Pelletier and Y. Chevalier, *International Journal of Pharmaceutics*, 2009, **368**, 7-15.

68. J. Marto, L. Gouveia, I. M. Jorge, A. Duarte, L. M. Gonçalves, S. M. C. Silva, F. Antunes, A. A. C. C. Pais, E. Oliveira, A. J. Almeida and H. M. Ribeiro, *Colloids and Surfaces B: Biointerfaces*, 2015, **135**, 183-192.

69. S. Tcholakova, N. D. Denkov and A. Lips, *Physical Chemistry Chemical Physics*, 2008, **10**, 1608-1627.

70. B. P. Binks, *Current Opinion in Colloid & Interface Science*, 2002, **7**, 21-41.

71. M. A. Creighton, Y. Ohata, J. Miyawaki, A. Bose and R. H. Hurt, *Langmuir*, 2014, **30**, 3687-3696.

72. C. Kaewsaneha, P. Tangboriboonrat, D. Polpanich, M. Eissa and A. Elaissari, *ACS Applied Materials & Interfaces*, 2013, **5**, 1857-1869.

73. P. G. de Gennes, *Reviews of Modern Physics*, 1992, **64**, 645-648.

74. A. Kirillova, G. Stoychev, L. Ionov, K.-J. Eichhorn, M. Malanin and A. Synytska, *ACS Applied Materials & Interfaces*, 2014, **6**, 13106-13114.

75. V. Saxena, A. Diaz, A. Clearfield, J. D. Batteas and M. D. Hussain, *Nanoscale*, 2013, **5**, 2328-2336.

76. A. Donnadio, V. Ambrogi, D. Pietrella, M. Pica, G. Sorrentino and M. Casciola, *RSC Advances*, 2016, **6**, 46249-46257.

77. J. Shaikh, D. D. Ankola, V. Beniwal, D. Singh and M. Kumar, *European Journal of Pharmaceutical Sciences*, 2009, **37**, 223-230.

78. V. Nedovic, A. Kalusevic, V. Manojlovic, S. Levic and B. Bugarski, *Procedia Food Science*, 2011, **1**, 1806-1815.

79. T. Kousksou, T. El Rhafiki, A. Jamil, P. Bruel and Y. Zeraouli, *Energy*, 2013, **56**, 175-183.

80. K. Peippo, P. Kauranen and P. D. Lund, *Energ Buildings*, 1991, **17**, 259-270.

81. M. N. A. Hawlader, M. S. Uddin and M. M. Khin, *Appl Energ*, 2003, **74**, 195-202.

82. D. P. Colvin, D. B. Moody and J. C. Driscoll, *Thermal management of electronic systems using diamond heat spreaders and microencapsulated PCM coolants*, American Institute of Aeronautics and Astronautics, 1997.

83. Y. Shin, D. I. Yoo and K. Son, *Journal of Applied Polymer Science*, 2005, **97**, 910-915.

84. R. Hannemann, presented in part at the Rohsenow Symposium on Future Trends in Heat Transfer, Cambridge, USA, May 16, 2003.

85. L. Zhang, Stanford University, 2002.

86. M. Asadi, G. Xie and B. Sunden, *International Journal Of Heat And Mass Transfer*, 2014, **79**, 34-53.

87. A. M. Adham, N. Mohd-Ghazali and R. Ahmad, *Renewable & Sustainable Energy Reviews*, 2013, **21**, 614-622.

88. J. Lee and I. Mudawar, *International Journal Of Heat And Mass Transfer*, 2007, **50**, 452-463.

89. H. A. Mohammed, P. Gunnasegaran and N. H. Shuaib, *International Communications In Heat And Mass Transfer*, 2010, **37**, 1496-1503.

90. B. Rimbault, N. Cong Tam and N. Galanis, *International Journal Of Thermal Sciences*, 2014, **84**, 275-292.

91. Y. Rao, F. Dammel, P. Stephan and G. P. Lin, *Heat Mass Transf.*, 2007, **44**, 175-186.

92. M. S. Mohammed Farid, Rami Sabbah, Said Al Hallaj, presented in part at the Fifth International Conference on Nanochannels, Microchannels and Minichannels, Puebla, Mexico, June 18-20, 2007.

93. R. Sabbah, M. M. Farid and S. Al-Hallaj, *Applied Thermal Engineering*, 2009, **29**, 445-454.

94. A. Jamekhorshid, S. M. Sadrameli and M. Farid, *Renewable & Sustainable Energy Reviews*, 2014, **31**, 531-542.

95. C. Y. Zhao and G. H. Zhang, *Renewable & Sustainable Energy Reviews*, 2011, **15**, 3813-3832.

96. L. Chen, L. L. Xu, H. B. Shang and Z. B. Zhang, *Energ Convers Manage*, 2009, **50**, 723-729.

97. E. Vignati, R. Piazza and T. P. Lockhart, *Langmuir*, 2003, **19**, 6650-6656.

98. A. Schrade, Z. Cao, K. Landfester and U. Ziener, *Langmuir*, 2011, **27**, 6689-6700.

99. K. Zhang, W. Wu, H. Meng, K. Guo and J. F. Chen, *Powder Technology*, 2009, **190**, 393-400.

100. S. Arditty, C. P. Whitby, B. P. Binks, V. Schmitt and F. Leal-Calderon, *Eur. Phys. J. E*, 2003, **12**, 355-355.

101. B. Xie, H. Shi, S. Jiang, Y. Zhao, C. C. Han, D. Xu and D. Wang, *The Journal of Physical Chemistry B*, 2006, **110**, 14279-14282.

102. A. Jamekhorshid, S. M. Sadrameli and M. Farid, *Renewable and Sustainable Energy Reviews*, 2014, **31**, 531-542.

103. F. Kuznik, D. David, K. Johannes and J.-J. Roux, *Renewable and Sustainable Energy Reviews*, 2011, **15**, 379-391.

104. Y. Fang, H. Yu, W. Wan, X. Gao and Z. Zhang, *Energ Convers Manage*, 2013, **76**, 430-436.

105. Y. Guan and Y. J. Zhang, *Soft Matter*, 2011, **7**, 6375-6384.

106. J. Dong, J. Weng and L. Z. Dai, *Carbon*, 2013, **52**, 326-336.

107. A. GhavamiNejad, S. Hashmi, H. I. Joh, S. Lee, Y. S. Lee, M. Vatankhah-Varnoosfaderani and F. J. Stadler, *Physical Chemistry Chemical Physics*, 2014, **16**, 8675-8685.

108. Y. Z. Pan, H. Q. Bao, N. G. Sahoo, T. F. Wu and L. Li, *Adv Funct Mater*, 2011, **21**, 2754-2763.

109. T. Zhou, B. B. Wang, B. Dong and C. Y. Li, *Macromolecules*, 2012, **45**, 8780-8789.

110. A. Diaz, M. L. Gonzalez, R. J. Perez, A. David, A. Mukherjee, A. Baez, A. Clearfield and J. L. Colon, *Nanoscale*, 2013, **5**, 11456-11463.

111. X. Wang, H. Wang and H. R. Brown, *Soft Matter*, 2011, **7**, 211-219.

112. J. Liu, C. Chen, C. He, J. Zhao, X. Yang and H. Wang, *ACS Nano*, 2012, **6**, 8194-8202.

113. T. Huang, H. Xu, K. Jiao, L. Zhu, H. R. Brown and H. Wang, *Advanced Materials*, 2007, **19**, 1622-1626.

114. H. Lee, J. Ryu, D. Kim, Y. Joo, S. U. Lee and D. Sohn, *Journal of Colloid and Interface Science*, 2013, **406**, 165-171.

115. A. Walther and A. H. E. Müller, *Chemical Reviews*, 2013, **113**, 5194-5261.

116. Y.-Z. You, K. K. Kalebaila, S. L. Brock and D. Oupický, *Chemistry of Materials*, 2008, **20**, 3354-3359.

117. S. Schmidt, T. Liu, S. Rütten, K.-H. Phan, M. Möller and W. Richtering, *Langmuir*, 2011, **27**, 9801-9806.

118. Y. Chen, Y. Bai, S. Chen, J. Ju, Y. Li, T. Wang and Q. Wang, *ACS Applied Materials & Interfaces*, 2014, **6**, 13334-13338.

119. J. Tang, P. J. Quinlan and K. C. Tam, *Soft Matter*, 2015, **11**, 3512-3529.

120. T. Suzuki, C. Morishita and M. Kawaguchi, *J. Dispersion Sci. Technol.*, 2010, **31**, 1479-1488.

121. H. Yang, F. Liang, X. Wang, Y. Chen, C. Zhang, Q. Wang, X. Qu, J. Li, D. Wu and Z. Yang, *Macromolecules*, 2013, **46**, 2754-2759.

122. Y. Wang and H. Wang, *Radiation Physics and Chemistry*, 2009, **78**, 234-237.

123. C.-D. Yuan, W.-F. Pu, X.-C. Wang, L. Sun, Y.-C. Zhang and S. Cheng, *Energy & Fuels*, 2015, **29**, 6165-6176.

124. T. Sharma, G. S. Kumar and J. S. Sangwai, *Journal of Petroleum Science and Engineering*, 2015, **129**, 221-232.

125. N. Rashidnia, R. Balasubramaniam and D. Del Signore, *AIChE Journal*, 1992, **38**, 615-618.

126. H. Kahl, T. Wadewitz and J. Winkelmann, *Journal of Chemical & Engineering Data*, 2003, **48**, 1500-1507.

127. I. Langmuir, *The Journal of Chemical Physics*, 1938, **6**, 873-896.

128. H. N. W. Lekkerkerker and G. J. Vroege, *Philosophical transactions - Royal Society. Mathematical, Physical and engineering sciences*, 2013, **371**, 20120263.

129. L. Onsager, *Annals of the New York Academy of Sciences*, 1949, **51**, 627- 659.

130. J. A. C. Veerman and D. Frenkel, *Physical Review A*, 1992, **45**, 5632-5648.

131. F. M. van der Kooij, K. Kassapidou and H. N. W. Lekkerkerker, *Nature*, 2000, **406**, 868-871.

132. J. E. Kim, T. H. Han, S. H. Lee, J. Y. Kim, C. W. Ahn, J. M. Yun and S. O. Kim, *Angewandte Chemie-International Edition*, 2011, **50**, 3043-3047.

133. A. M. Alsayed, M. F. Islam, J. Zhang, P. J. Collings and A. G. Yodh, *Science*, 2005, **309**, 1207-1210.

134. S. Tang, Z. Hu, Z. Cheng and J. Wu, *Langmuir*, 2004, **20**, 8858-8864.

135. A. F. Mejia, Y. W. Chang, R. Ng, M. Shuai, M. S. Mannan and Z. D. Cheng, in *Physical Review E*, 2012, vol. 85, ch. 061708-1, pp. 061708(061701-061712).

136. M. Marechal, A. Cuetos, B. Martínez-Haya and M. Dijkstra, *The Journal of Chemical Physics*, 2011, **134**, 094501.

137. H. H. Wensink and H. N. W. Lekkerkerker, *Molecular Physics*, 2009, **107**, 2111-2118.

138. X. Wang, D. Zhao, I. B. N. Medina, A. Diaz, H. Wang, A. Clearfield, M. S. Mannan and Z. Cheng, *Chem Commun*, 2016, **52**, 4832-4835.